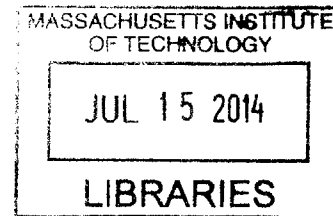# Hybrid Laser with CMOS Photonics

by

Johanna S. Chong

Submitted to the Department of Electrical Engineering and Computer
Science
in partial fulfillment of the requirements for the degree of

Master of Engineering in Electrical Engineering

at the

MASSACHUSETTS INSTITUTE OF TECHNOLOGY

February 2014

Signature redacted

Author . . . .
Department of Electrical Engineering and Computer Science
February 1, 2014

Signature redacted

Certified by . . . .
Rajeev J. Ram
Professor of Electrical Engineering
Thesis Supervisor

Signature redacted

Accepted by . . . .
Albert R. Meyer
Chairman, Masters of Engineering Thesis Committee

Hybrid Laser with CMOS Photonics

by

Johanna S. Chong

Submitted to the Department of Electrical Engineering and Computer Science
on February 1, 2014, in partial fulfillment of the
requirements for the degree of
Master of Engineering in Electrical Engineering

Abstract

In this thesis, an interesting approach for a photonic laser source is presented. By using integrated photonic resonators with an external gain medium, we are able to build a laser that offers a number of advantages including reducing the electrical and thermal load on the integrated chip socket, eliminating the challenges of integrating gain mediums into CMOS processes, allowing for lasing at virtually arbitrary wavelengths, the possibility of multiwavelength operation with a shared gain medium, elimination of closed-loop control of wavelength tuning, ability to control laser output and wavelength on-chip, and the potential for wavelength modulation using novel resonator tuning designs. Several iterations of the laser were built and characterized culminating in a final integrated laser that showed a wall-plug efficiency of 1.10% at a maximum output power of 6 mW. We demonstrate even higher wall-plug efficiencies using commercial filters. We also demonstrate wavelength modulation and open eye diagrams for data rates up to 5 Gb/s using the laser in a communications link. Simulations of birefringent filters are performed to model wavelength dependence on polarization which when manipulated can give rise to single or multiwavelength lasing. Finally, the power spectral density is simulated by assuming uncorrelated phase between lasing modes.

Thesis Supervisor: Rajeev J. Ram
Title: Professor of Electrical Engineering

Acknowledgments

I would like to first thank Prof. Rajeev Ram for helping me build my first foundations in research and guiding me to the enjoyment of my own work . I have also internalized much of his wisdom about life extracted from many consecutive and intense conversations. I can't begin to convey the depth of what I learned from him in my time here. For that, I am leaving changed and truly grateful.

I would also like to thank Prof. Tianxin Yang with whom I had the pleasure of working on the initial half of the project and from whom I had gained the momentum to continue on my own. This thesis stands on the shoulders of her earlier research efforts.

I would also thank Jason Orcutt and Karan Mehta from whom I frequently sought help and equipment. Much of what I've learned about lab work was learned from them. I find their habits and dedication quite admirable, and I have since become inspired to mimic some of their traits.

I would also thank Michael Georgas, Ben Moss, and Chen Sun from what I always called "the downstairs lab". Many of the key experiments in this thesis would not have happened without their help. In particular, I would like to thank Mike for his ever-constant willingness to help me out and find me in lab whenever he had the time.

I thank my fellow labmates in POE including those that have left while I have been here. It has been great to be in your company for the past two years. In particular, I mention Ashwyn, my bubble tea buddy and deskmate, and Parthi, who has been a great friend to me.

I also thank MIT Sport TKD and the women of BPF. Training with both of these groups has been the daily asylum I needed to remain sane and to remind myself that life offers a diversity of fulfilling activities.

Finally, I thank Mom, Dad, Lydia, Justin, and Victor for their unconditional love and support regardless of what I'm doing. I did this program for me, but I'm always thinking of you guys.

Contents

Chapter 1

Introduction

1.1 Sources for Interconnects

The required performance specifications of an optical source for electronic-photonic integrated circuits (EPICs) will be outlined through the description of a target application. Specifically, the system of interest will be a CMOS fabricated multicore CPU optically-linked to its main memory chips.

The core-to-memory bandwidth in modern CPUs is limited by electrical links in terms of the number of physical connections and energy dissipation. Photonic core-to-memory links address the issues of limited bandwidth and energy with the inherent advantages of wavelength-division multiplexing and high carrier frequency. In addition, increased bandwidth would lead to increased efficiency of processing cores while increasing the number of cores that would fit on a single chip.

1.1.1 Power Budget and Photonic Link Description

The total power consumed on a microprocessor has stabilized at 100 W as an average power dissipation limit over the last decade [1]. Of the total power, we approximate 60% is used for computation performed by processing cores, 20% is used for on-chip communication such as clock and core-to-core links, and 20% is for off-chip communication including socket-to-socket and core-to-memory links. We consider

only the core-to-memory links as our target application, which are assumed to require half of the off-chip power budget. Therefore, a maximum power dissipation of 10 W is outlined for this interconnect system.

To define a target bandwidth, we consider first the computational limits of the processing cores based on system targets and budgeted power. The desired performance of a general system architecture is one byte of data fetched per floating point operation (FLOP). We set the energy cost per FLOP using a High Performance Computing target of 10pJ/FLOP [2], and given a 60 W computational budget, this allows for 6 TFLOPs in the target processor. To achieve such performance, the read and write data paths of the system each require 48 Tbit/s defining the total bandwidth to be 96 Tbit/s.

In the simplest architecture, the notable optical and optoelectronic devices of a single photonic link are filters, modulators, and detectors. Tracing a link path beginning from the source, the light from the source must be coupled and then split into multiple waveguides. The launched light is modulated, dropped through a filter, and delivered to a detector. Assuming a link rate of 10 Gbit/s and 32 wavelengths, we require 150 waveguides to reach the target bandwidth of 48 Tbit/s.

Losses in the system links as a result of the thermal tuning of microring resonators for filtering signals, modulation, and detection will consume the off-chip power budget. For a recently proposed photonic link, the total link energy budget is found to be 188 fJ/bit with 100 fJ/bit for thermal tuning of microring filters, 38 fJ/bit for modulation drive, and 50 fJ/bit for detection [1]. Based on the link budget and a single direction bandwidth of 48 Tbit/s, the power dissipation in the links is calculated to about 9 W which falls within the 10 W. limit. This leaves 1 W for powering the optical source.

1.1.2 Target Performance of Off-Chip Laser Sources

The required optical power of the laser source is found by considering the target receiver sensitivity and the sources of optical loss. Upstream and downstream links losses are respectively found to be 7.9 dB and 8.9 dB with photodiode efficiencies of 0.8 and 0.5. The receiver sensitivities are given as 10 uA and 5 uA respectively [1].

Thus, the link optical power is calculated to be 77.07 uW upstream and 97.72 uA downstream at 1240 nm wavelength giving an average link optical power of 87.4 uW.

Using this result, we estimate the required output power of a single channel to be 15 mW. The total laser output power for all wavelengths is 480 mW, and thus, the required wall-plug efficiency to meet the 1 W dissipation limit is 48%. If we assume instead that the source has a wall-plug efficiency of 30%, the power dissipated by the source increases to 1.6 W of power. We will express dissipation of up to 2 W as a reasonable target and thus a wall-plug efficiency of at least 25% as desirable.

1.1.3 CMOS Processing and Packaging Requirements

The fabrication of the target application as mentioned above is a CMOS compatible process demonstrated by Jason Orcutt and others in the POEM program. As a result, the possible integration of an optical source must be considered with CMOS foundry processing and packaging requirements in mind.

Work in the POEM program has already demonstrated successfully integrated passive and active photonics with continuously improving performance [3]. However, the work of testing and characterizing these devices and links has mostly depended on external laser sources that are fiber-to-chip coupled, and more specifically, the efforts have met many challenges with regards to WDM experiments which require multiwavelength sources. The major challenges surrounding a dedicated photonic source examine not only the laser's impact on the power budget but also the measure of integration possible. As a result, one can see the spectrum of solutions that vary in trade-offs between processing and packaging.

At the highest level, the CMOS process can be separated into front-end and back-end processes. The front-end processes are everything up to but not including the metal interconnect layers. This includes layout of the field-effect transistors (FETs), diodes, and other semiconductor devices. It operates at high tempteratures up to 1050°C and is material restrictive. The back-end lays out the metal interconnects. The temperature is lower at 450°C, and there is more flexibility with material selection [1]. Based on these general rules, the resulting limits of laser integration come from

13

temperature and gain material compatibility at either ends of the CMOS process.

Furthermore, laser solutions that choose not to integrate the laser gain and cavity will lead to post-foundry processes whose advantages and disadvantages must be closely examined including packaging costs and CMOS foundry scale manufacturing. In Section 1.3, we will discuss different approaches to the photonic source and keep the processing and packaging compatibilities in mind.

1.2   Semiconductor Diode Laser Theory

Having illustrated the needs of the target application with regards to a laser source, we now review semiconductor diode laser theory in a phenomenological approach closely following the presentation by Coldren and Corzine in *Semiconductor Diode Laser Theory* to give a framework for some of the physics that will come into consideration in the design and optimization of sources [4]. We begin with single-mode rate equations to illustrate the movement of carriers and photons and how their density effects the gain. From single-mode, we extend the analysis to multi-mode rate equations. From these equations, we are able to discuss the gain and loss of a system and how it affects important lasing parameters which will affect the overall wall-plug efficiency.

1.2.1   Single Mode Rate Equations

We begin by describing the total carrier density rate in terms of current continuity. In an electrically pumped device, the injected carrier density rate is the gradient of the electron current density J divided by the charge q

$$\left(\frac{dN}{dt}\right)_{inj} = \frac{1}{q}\nabla_r J \tag{1.1}$$

We evaluate the gradient by considering the carrier buildup in the active region of a device with active length L_a and area A. For some input bias current I_{bias}, a 100% efficient laser is one in which the output electron current I_{out} is equal to zero allowing us to express the gradient as I_{bias}/V_a where the *active volume* $V_a = L_a A$. As the

14

laser does not have perfect efficiency, we scale the result by a quantum efficiency η_i.
Equation 1.1 is rewritten as

$$\left(\frac{dN}{dt}\right)_{inj} = \frac{\eta_i I_{bias}}{qV_a} \tag{1.2}$$

Inside the active region, carriers are being lost in radiative and nonradiative recombination events. Photons are emitted through stimulated emission, expressed as a rate R_{st}, or spontaneous emission, R_{sp}. The nonradiative recombination rate R_{nr} describes the loss of carriers through a phonon transition. We can express the total carrier density rate equation as

$$\frac{dN}{dt} = \frac{\eta_i I}{qV} - R_{st} - R_{sp} - R_{nr} \tag{1.3}$$

The photon density rate equation is partially extracted from the radiative recombination terms. Photon generation is thus a function of the stimulated and spontaneous emission rates. To write an expression for photon generation, we define the *confinement factor* Γ which is a proportional factor describing the finite overlap between the optical mode and the gain. As a result, both spontaneous and emission rates are multiplied by the confinement factor. Furthermore, as we are developing *single-mode* rate equations, we multiply the spontaneous emission rate by β_{sp}, the *spontaneous emission factor*, which is defined as the reciprocal of the number of optical modes in the bandwidth of spontaneous emission. The photon density generation rate is expressed as follows

$$\left(\frac{dN_p}{dt}\right)_{gen} = \Gamma R_{st} + \Gamma \beta_{sp} R_{sp} \tag{1.4}$$

Photon annihilation can be summarized using the *photon lifetime*, τ_p. This parameter describes the average time the photon survives in the laser cavity before it is lost. It will be related to the losses of the system in section 1.2.3, but for now, it suffices to say that the photon density rate equation takes the form

$$\frac{dN_p}{dt} = \Gamma R_{st} + \Gamma \beta_{sp} R_{sp} - \frac{N_p}{\tau_p} \tag{1.5}$$

Equations 1.3 and 1.5 are coupled rate equations that describe the steady-state

and dynamic responses of the diode laser. The next section will define the rates more explicitly in order to guide us to steady-state solutions.

1.2.2 Recombination Rates

The nonradiative recombination rate is the sum of two processes: trap-assisted recombination and Auger recombination. These processes are dependent on the carrier density and can be written as a polynomial

$$R_{trap} + R_{auger} \sim AN + CN^3 \tag{1.6}$$

Trap-assisted recombination depends on the presence of traps in the middle of the bandgap which occur as a result of defect states in the semiconductor. THis rate is proportional to the number of traps present and as such is a linear function carrier density.

Auger recombination is a three-body collision, involving a high energy electron-hole pair and an electron which absorbs the released energy increasing its kinetic energy. As a result, this rate must be proportional to the hole density and the square of the electron density. In the lightly doped assumption, the density of electron hole pairs is equivalent to the electron density, giving rise to Auger dependence of $\sim N^3$.

The spontaneous emission rate can also be determined with a similar treatment. For a spontaneous recombination event to occur, we require one electron and one hole, which means the rate changes as $\sim NP$ where P is the hole density. A fit coefficient B is called the bimolecular recombination coefficient. We, therefore, can approximate the spontaneous emission rate as

$$R_{sp} \sim BN^2 \tag{1.7}$$

To find the stimulated emission rate, we assume that across a small segment of gain medium with length z, an input photon density N_{po} will yield an output photon density $N_p = N_{po}e^{+g(N)z}$, increasing the photon density by some $\Delta N_p =$

16

$N_{po}(e^{+g(N)z} - 1)$. Evaluating the spatial derivative we find that $\frac{dN_p}{dz} = g(N)N_p$. Multiplying by the group velocity, the time derivative and an expression for the stimulated emission rate is the following

$$R_{st} = v_g g(N)N_p \tag{1.8}$$

This rewrites rate equations 1.3 and 1.5 into the form

$$\frac{dN}{dt} = \frac{\eta_i I}{qV} - v_g g(N)N_p - (AN + BN^2 + CN^3) \tag{1.9}$$

$$\frac{dN_p}{dt} = \Gamma v_g g(N)N_p + \Gamma \beta_{sp} BN^2 - \frac{N_p}{\tau_p} \tag{1.10}$$

1.2.3 Gain and Loss

We begin the discussion of gain and loss by stating the round-trip condition of a laser. The condition states that the product of the transmittances of all the discrete elements of the laser must equal 1. If less than one, the mode will decay to zero. If greater than 1, the mode will grow without bound. We express this in terms of a gain medium transmittance G, a coupler transmittance T_m, and cavity transmittance T_i. The round-trip condition is written as

$$T_i T_m G = 1 \tag{1.11}$$

where the gain medium transmittance is found from the threshold gain by

$$G = e^{\Gamma g_{th} L} \tag{1.12}$$

and the cavity transmittance is found from the internal loss parameter as follows

$$T_i = e^{-\alpha_i L} \tag{1.13}$$

By taking the natural log of the expression and rearranging, we can express the

17

equation in terms of threshold gain g_{th} and internal loss α_i, as well as the cavity length, L.

$$\Gamma g_{th} = \alpha_i + \frac{1}{L} \ln\left(\frac{1}{T_m}\right) \tag{1.14}$$

The above is the required condition to achieve threshold in a laser. We can express the coupler loss contribution as a mirror loss α_m defined

$$\alpha_m = \frac{1}{L} \ln\left(\frac{1}{T_m}\right) \tag{1.15}$$

From the above results, we are able to define the photon lifetime τ_p. From inspection, we realize that the total losses, which has units of inverse length, is equivalent to the product of the group velocity v_g and photon lifetime inverse. This defines the photon lifetime as

$$\tau_p = \frac{1}{v_g(\alpha_i + \alpha_m)} \tag{1.16}$$

An explicit expression of the gain is needed to calculate laser performance parameters. The gain can be well-approximated by a simple logarithmic function of the carrier density

$$g(N) = g_0 \ln\left(\frac{N}{N_{tr}}\right), \qquad (g \geq 0) \tag{1.17}$$

where g_0 is a gain coefficient obtained from fitting and N_{tr} is the transparency carrier density. The latter corresponds to the carrier density at which the gain is equal to zero. We refer to the gain in a more useful fashion in terms of the bias current and by defining our gain in dB as $G_{dB} = 10\log_{10}(e^{g(N)L})$. Our gain as a function of current becomes

$$G_{dB}(I) = G_{dB,0} \ln\left(\frac{I}{I_0}\right), \qquad (G \geq 0) \tag{1.18}$$

where I_0 represents that bias current at which the gain is equal to zero.

1.2.4 Threshold and Efficiency

We restate the threshold condition substituting the mirror loss from Equation 1.15

$$\Gamma g_{th} = \alpha_i + \alpha_m \tag{1.19}$$

Equation 1.19 shows how one could express the loss parameters in terms of threshold current using Equation 1.18. Specifically, the threshold gain can be related to the threshold current by the following

$$G_{th} = G_0 \ln \left(\frac{I_{th}}{I_0} \right) \tag{1.20}$$

The gain clamps at the threshold value. This expression is only valid for currents less than I_{th}.

We also evaluate the differential efficiency η_d which describes the percentage of photons in the cavity that will be able to leave the cavity to become useful photons. It is evident that the mirror loss will dominate changes in our differential efficiency while the internal losses will have a weak influence. The differential efficiency is as follows

$$\eta_d = \frac{\eta_i \alpha_m}{\alpha_i + \alpha_m} \tag{1.21}$$

We are now able to calculate the output optical power which is a function of the threshold current and the differential efficiency beyond threshold. We write the expression as

$$P_{opt} = \eta_d \frac{h\nu}{q}(I - I_{th}), \qquad (I \geq I_{th}) \tag{1.22}$$

To approximate the input or electrical power, we multiply the input bias current by the voltage of the quasi-Fermi level separation at transparency.

$$P_{elec} \approx \frac{h\nu}{q} I \tag{1.23}$$

From this, it is simple to calculate the wall-plug efficiency, a figure of merit which

measures the laser power consumption efficiency, written as follows

$$\eta_{wp} = \frac{P_{opt}}{P_{elec}} \qquad (1.24)$$

1.2.5 Multimode Rate Equations

When multiple modes are present, it is straightforward to express the rate equation for each mode indexed i

$$\frac{dN}{dt} = \frac{\eta_i I}{qV} - (R_{sp} + R_{nr}) - \sum_i v_{g,i} g_i N_{p,i} \qquad (1.25)$$

$$\frac{dN_{p,i}}{dt} = \Gamma_i v_{g,i} g_i N_{p,i} - \frac{N_{p,i}}{\tau_{p,i}} + \Gamma_i R'_{sp,i} \qquad (1.26)$$

Note that the photon density, group velocity, gain, photon lifetime, and confinement factor depend on the mode. The electron density changes as the summation of the stimulated recombination events for each mode i. Furthermore, the photon density is expressed as a single mode. $R'_{sp,i}$ is the spontaneous recombination rate for a single mode; thus, note that β_{sp} is no longer in the rate equation.

We set the photon density rates to zero and present the steady-state solution of each mode

$$N_{p,i} = \frac{\Gamma_i R'_{sp,i}}{\frac{1}{\tau_{p,i}} - R_{st,i}} \qquad (1.27)$$

The spontaneous emission is defined in terms of the *inversion factor*, n_{sp}.

$$R'_{sp,i} = n_{sp} R_{st,i} \qquad (1.28)$$

The inversion factor is always greater than 1 and decreases with increasing carrier injection. It approaches unity at complete inversion; that is, when there are no carriers left in the valence band.

We can also express the photon lifetime for a single mode in the same method as Equation 1.16

$$\tau_{p,i} = \frac{1}{v_{g,i}(\alpha_s + \alpha_{m,i})} \qquad (1.29)$$

20

The photon density can be rewritten as follows

$$N_{p,i} = \frac{\Gamma_i n_{sp}}{\frac{1}{G_i} - 1} \tag{1.30}$$

where we have introduced G_i as the normalized gain

$$G_i = g_i v_{g,i} \tau_{p,i} \tag{1.31}$$

Combining Equations 1.31 and 1.29 gives a different expression for the normalized gain

$$G_i = \frac{g_i}{\alpha_s + \alpha_{m,i}} \tag{1.32}$$

We wish to evaluate at lasing modes. As such, we take the normalized gain to approach unity, $G_i \rightarrow 1$. We now simplify the steady-state photon density as the following

$$N_{p,i} \approx \frac{\Gamma_i \beta_{sp} n_{sp}}{1 - G_i} \tag{1.33}$$

Finally, the Mode Suppression Ratio (MSR) is defined the main mode power divided by the side mode power.

$$\text{MSR} = \frac{P(\lambda_0)}{P(\lambda_1)} \tag{1.34}$$

In a single mode laser, suppression of side modes is desired while in a multiwavelength laser, the goal will be to minimize this value around the center wavelength.

1.3 Possible Solutions to Photonic Sources

This section will discuss possible methods of developing multiwavelength sources for optical interconnects. We consider the merit of each solution in the context of our target application of a CMOS process compatible photonic circuit.

1.3.1 External Lasers

The most straightforward method of creating an optical interconnect source is to dedicate a single off-chip laser for each required wavelength. We first examine the kind of performance such a solution would achieve. We evaluate a 1177 nm distributed feedback (DFB) quantum dot laser from QD Laser/Cybel.

An obvious advantage of an off-chip laser is that wavelength can be chosen almost arbitrarily. As it will be shown, wavelength selection becomes a potential issue in the development of other solutions. The target center wavelength is 1180 nm for the core-to-memory system, which is a specification the laser meets. Another advantage is the side mode suppression ratio (SMSR) is huge and far exceeds the required spec of 20 dB [1]. Efficiency aside, the laser can also provide any amount of output power. We also expect excellent performance in the signal-to-noise ratio (SNR).

The differential efficiency in this wavelength range is approximately 35% with a threshold current of 22.5 mA [5]. At 15 mW required output, this gives a wall-plug efficiency (WPE) 23% nearing target requirements.

The most significant comment, however, of operating an off-chip bank of lasers is the need for temperature control. We first consider the effects on packaging. The optical outputs of the individual modules can be multiplexed into a single output fiber coupled to the source. However, electrical feedback from the chip I/O pins is required for each laser for wavelength alignment to the on-chip optical channels. The 1177 nm DFB QD laser package requires 4 connects, 2 for each thermistor terminal and 2 for each cooler terminal. For 32 lasers, this leads to a requirement of 128 I/O pins that will be used for temperature control. This is a huge amount of real estate that is occupied for simply wavelength aligning the lasers. The second issue with temperature control is the additional power dissipation leading to losses in efficiency. Furthermore, this power dissipation will load the socket as the cooler must be controlled by the chip. Finally, the chip will require additional electronics on-chip to work with the laser module cooler feedback system.

An ideal solution for interconnect sources would eliminate the need for tempera-

ture control or eliminate the use of I/O pins by being on-chip. The following sections explore solutions undergoing research that attempt to accomplish this goal.

1.3.2 Hybrid III-V Silicon Evanescent Lasers

III-V materials are well-established in the creation of optoelectronic devices, but they cannot be grown on silicon substrate. As a result, hybrid III-V/Silicon lasers always require a post CMOS process step thus complicating the packaging.

In the case of evanescent lasers, III-V layers are created and then bonded to an SOI chip. Precise alignment is not required due to the lateral symmetry of the III-V layer. The laser is electrically pumped through contacts patterned on the semiconductor, and the evanescent wave propagates through a silicon waveguide on the SOI chip.

In a room temperature and electrically pumped device created by *Fang et al.*, an output power of 1.8 mW, threshold current of 65 mA, and a differential quantum efficiency of 12.7% is demonstrated. This corresponds to a wall-plug efficiency of 2.3%. The maximum operating temperature is 40 °C. This work reports that the device could be further optimized to improve lasing threshold and slope efficiency as well as increasing operating temperature [6].

This solution has the advantage of minimal alignment and lasing wavelength flexibility, but is greatly limited in its scalability alongside CMOS electronics. The first issue is the yield in III-V processes would likely set the limiting yield even for a billion-transistor scale. The second issue is that it is not possible to grow large enough III-V wafers for bonding to Silicon wafers. Production of these lasers would be limited to the die or partial wafer level. Furthermore, determination of a properly working laser can only occur after the semiconductor has already been bonded to the silicon.

Though this solution is particularly flexible, it requires a significant amount of processing work outside of the CMOS foundry without the ability to keep up with foundry throughput.

1.3.3 Germanium on Silicon Lasers

Germanium lasers have been investigated because germanium can be grown directly on silicon. Theoretical models have also shown that with enough tensile strain, Germanium can be made into a direct bandgap material with good optoelectronic properties [7]. However, at the time of this writing, creating the necessary strain has not been achieved and still an area of research. Current germanium on silicon lasers use a combination of tensile strain and n-type doping of the germanium.

An electrically-pumped Ge-on-Si laser has been demonstrated by *Camacho-Aguilera et al.*. The device outputs 1 mW of power at a threshold current density of 280 kA/cm^2. To find the area, we use the waveguide width and length. The width is given as $w = 1\mu m$, and a length of $L = 1mm$ is assumed based on previous work with 4.8 mm length waveguides [8]. Based on this, the threshold current calculated to be 2.8 A. Lasing wavelengths are reported between 1510 and 1700 nm with a gain spectrum bandwidth of 200nm [9]. With a maximu output power of 1 mW and threshold current on the order of 1 A, the WPE is found to be very low; less than 0.1%.

Germanium on silicon as aforementioned has the advantage of CMOS compatibility, but the issue of high diffusion into the silicon at high temperatures. As germanium is a front-end process, this does not allow the lasers to be created in the same mask as the transistors adding additional steps to the process. Furthermore, while the hope for creating enough tensile strain exists, the present need for doping still adds another processing step. The results so far for Germanium on silicon are not sufficient for photonic interconnect sources but that the trajectory of ongoing research is somewhat promising.

1.3.4 Erbium-doped glass lasers

Erbium-doped glass as a gain medium is another possibility as an on-chip laser source. One approach by *Purnawirman et al.* uses silicon nitride (SiN_x) strip embedded in SiO_2 to create a ridge waveguide. An erbium-doped glass layer is then deposited

onto the wafer. If the mode propagates in the z direction, the ridge and the index differences between the glass, wafer, and air interfaces confine the modes in the x and y directions. The mode is guided in the erbium-doped glass.

The waveguide has a length $L_{gain} = 20mm$ and a width $w = 4.0\mu m$, and the device is optically pumped with a 980 nm laser. The laser achieves a maximum on-chip output power of 5.1 mW with threshold power of 44 mW and a slope efficiency of 2.6%. It also showed lasing wavelengths in the C and L-bands [10]. To calculate the wall-plug efficiency, we first determine the efficiency of the pump laser. We take the specifications for a high-efficiency 980 nm laser from JDSU and state that the pump laser wall-plug efficiency is 64% [11]. From this result, we find the erbium-doped glass laser has a wall-plug efficiency of 1.7%.

For our target application, the erbium-doped fiber laser has a number of drawbacks. First, though SiN is a CMOS compatible material, it is not inherently in the CMOS process, and the device cannot be fabricated within the foundry steps. Second, erbium-glass will always be optically pumped which adds the additional step of coupling a laser from off-chip. However, this has the advantage of relieving the power consumption on the socket. Third, for a purely erbium-doped glass laser, the device sizes will have to be rather large to achieve enough gain (one source reports 4.1 dB/cm of gain [12]) which makes it questionable that such a device could work on the μm scale.

1.3.5 Quantum Dot Comb Laser

The quantum dot comb laser from Innolume uses a quantum dot active region with a Fabry-Perot cavity to create a comb spectrum. A wide bandwidth distributed bragg reflector (DBR) rather than the gain spectrum selects the modes of interest, and the mode spacing is decided by the cavity length. For example, a cavity length of 1 mm corresponds to a free spectral range of $\sim$ 40 GHz while a length of 500 μm gives an $\sim$ 80 GHz FSR [13].

The Innolume comb laser is a completely external source but has a multiwavelength output. One package offers 16 wavelengths per comb. The target application

would then require two comb laser packages. In addition, temperature control allows one to tune the comb and not individual wavelength. In the event that integrated filters are not designed to consistent spacings, this will pose a problem.

The comb laser data sheet gives the slope efficiency as 0.19 W/A. Maximum optical output power is 12 mW which translates to 750 μW per wavelength at the operating current 77 mA. Given that the forward voltage is 1.95 V, we find that the WPE is 7.8% [14]. Furthermore, Innolume demonstrates that each individual Fabry-Perot modes can be modulated up to 10 GB/s. The comb output has also been modulated at data rates up to 3.2 Gb/s [13].

The individual FP modes also show low relative noise intensity (RIN) [15]. According to [16], the cavity contains a "noise-reducing" component in addition to its active gain in the cavity. This "noise-reducing" section is thought to be a saturable absorber. Used in passive mode-locking of lasers, a saturable absorber has the property where at high optical intensities the absorption decreases due to the carrier depletion. As a result, noise intensity is suppressed by the absorber region. The effects of mode-locking will be addressed in a later chapter.

1.3.6   Off-chip gain and on-chip cavity

The method proposed in this thesis employs a hybrid design of off-chip gain and on-chip resonators for tuning and selection of lasing modes. More specifically, the gain and resonator are connected in a fiber ring. The advantages of this type of laser is that it offloads the required power to pump the laser by keeping the gain medium off-chip while eliminating the need for temperature control of wavelength by keeping the resonators on-chip and thus matched to the chip temperature. It has no effect on the CMOS processing steps given that the resonator bank fabrication is established as foundry compatible. Of further interest is the possiblity for multiwavelength operation using a single source gain.

The presence of the gain outside of the chip complicates the packaging step. Yet because of the interesting multiwavelength behavior, only a single optical fiber needs to be coupled between the chip and SOA package unlike the case with an array of

single wavelength lasers. However, the behavior of multimode lasers with shared gain mediums is not completely understood. This poses interesting questions about the stability and performance of such a system and stands as the most significant challenge to this method. This is an issue that is explored throughout the thesis, but much of the research is performed treating the laser a single mode source.

At the time of this writing, there has been one other laser found in research that uses the hybrid approach. Designed by *Jeong et al.*, the laser is cavity is completely fabricated into a silicon chip. The SOA is butt-coupled to the cavity chip which consists of a coupler, micro-ring resonator, and Bragg reflector at the output. A mirror at the SOA input completes the Fabry-Perot cavity. The micro-ring resonator is assumed to have a large enough FSR that the Bragg reflector acts a wavelength selective component. As a result, the laser is designed for single-mode lasing.

The most recent results reported threshold current at 48 mA and output power of 3 mW at a current of 210 mA. This corresponds to a slope efficiency of 1.85% and a WPE near 1.4% for 3 mW output power. Reaping the benefits of on-chip resonator and wide bandwidth of Bragg reflector, they have also demonstrated a laser tuning of +0.079 nm/°C [17].

Furthermore, the laser competence as a data carrier is presented. The hybrid laser was originally designed with a fabricated modulator structure in mind. In fact, the purpose was to explicitly solve the cost of temperature tuning to the modulator resonance. The hybrid laser demonstrated a 10 Gb/s open eye diagram at two different temperatures [18]. It remains that to accomodate 32 wavelengths, this approach requires 32 SOAs; though useful for their application, we are still interested in reducing the packaging costs further. Nevertheless, the results demonstrated in this hybrid laser will be a figure of comparison for the results of this thesis.

1.4 Multiwavelength Operation of Fiber Ring Laser

Previous work on these lasers as multiwavelength sources have experimented with different gain mediums and with discrete filters placed into the fiber loops or using

27

the resonance of the fiber loop to create the filter peaks. Consistently, polarization dependent gain is reported. Work in this type of laser generally uses either an Erbium Doped Fiber Amplifier (EDFA)[19] or a Semiconductor Optical Amplifier (SOA) [20] as the gain medium. However, the design challenge lies in the issue that in both gain mediums, the wavelengths are not independent and are subject to some homogeneous broadening.

In homogeneous broadening, the gain spectrum does not change. We can consider the system as a single oscillating spring system, and thus in the context of the ring laser, we would not expect the rise of independent multimode behavior. In a purely inhomogeneous broadening case, the system can be considered as a many independent oscillating springs; a more ideal case for multimode operation. In the case of both EDFA and SOA gain mediums, the system is neither purely homogeneous or inhomogeneous and rather somewhere in between behaving more as coupled oscillating systems.

A consequence of this issue in the design aspect of the ring laser is the exploitation of nonlinearity within the gain medium and/or in the cavity. Nonlinear effects examined in gain mediums for generation of multimode or inhomogeneous behavior include spatial-hole burning effects and four-wave mixing [21, 22]. Intensity-dependent loss mechanisms built within the cavity are a more controllable aspect of design. A common approach is the use of the Kerr effect in combination with polarization effects to induce loss at higher intensities [23].

Many iterations of a mostly consistent ring laser design has been shown in the previous work in this topic. Figures of merit that are typically discussed are the laser stability as well as total output power. However, there also seems to be a limit to knowing how applicable some designs are to a photonic interconnect system. At the time of this writing, no work showing modulation or data transmission using a multiwavelength ring laser system has been demonstrated. Furthermore, stability is often described in pictures of cascaded spectra. It will be a goal of this thesis to more deeply understand that multimode stability behavior of this laser design.

1.5 Conclusion and Thesis Overview

Laser Solution	Threshold Current	Output Power	WPE	Processing	Packaging	Wavelength Alignment
External Lasers	22.5 mA	15 mW	23%	N/A	Off-chip	Required
Hybrid III-V	65 mA	1.8 mW	2.3%	Post-CMOS	On-chip	Required
Ge-on-Si	2.8 A	1 mW	< 0.1%	CMOS	On-chip	Required
Erbium-doped Glass	44 mA	5.1 mW	1.7%	Post-CMOS	On-chip	Required
Quantum Dot Comb Laser	mA	0.8 mW	7.8%	N/A	Off-chip	Required
External Gain with Integrated Filter	48 mA	3 mW	1.4%	CMOS (filter)	On-chip filter, off-chip gain	Not Required

Figure 1-1: Table summarizing photonic laser solutions and key features of laser performance and cost effectiveness.

In this section, we have provided the description of the target photonic application for which a laser source is required and the resulting laser specifications. The aim is for the laser to be low-cost in terms of processing and packaging with a wall-plug efficiency of at least 25% . A phenomenological description of the semiconductor laser was given to provide background on the important aspects of laser performance, and we have also discussed current approaches in research that aim to solve the source problem including the approach of this thesis to use an external gain source with integrated components to build a laser.

Figure 1-1 summarizes the this information. Of the approaches covered, only the simplest approach, an array of external high-efficiency lasers, reaches the desired WPE. Second in WPE is the commercial multiwavelength comb laser. Integrated solutions are clearly still in the realms of research with WPE of less than 5%. Furthermore, the production of these integrated solutions involves material science questions and undoubtedly many iterations with fabricated test chips.

29

The solution presented in this thesis is approachable from the perspective of first using commercial products before moving to the integrated approach. As a result, the benefits of such a laser can be reaped well before it becomes a final integrated component of the system. Comparatively as a solution, much of the integrated solutions are projected to have longer timelines of research. It could be considered that the method presented in this thesis as a "hybrid" approach acts as an intermediate step to future integrated sources.

As such, the remainder of the thesis will discuss the experiments and theory developed in efforts to optimize and understand the laser's performance. Chapter 2 will begin with experiments with a fiber ring laser that use commercial filters rather than integrated components. The performance of the fiber ring laser are evaluated and optimized, and the results of these efforts act as an intentional stepping stone to using integrated components. Chapter 3 will replace the commercial filter with integrated micro-ring resonators fabricated on EOS18 device chips as part of the POEM project. Though the experimental setup is quite different, much of what was learned in Chapter 2 is applied in evaluation of the laser performance. Chapter 4 will attempt to provide some framework of basic theory that describes some of the physics of the laser at work to explain some of the more unexpected and interesting results. Finally, Chapter 5 will discuss what remains to be done in future work that involve experiments and modeling of the laser.

Chapter 2

Building the Multiwavelength Ring Laser

In this section, we discuss the construction and results of several iterations of the multiwavelength ring laser using discrete fiber optical components.

The first iteration of the laser uses a 1310 nm centered SOA. The structure of the laser is described, and the components are individually characterized. Component performance is measured, and key laser parameters of threshold current, lasing wavelength, and efficiency are predicted based on the measured results. The laser is then built and observed. We then compare the predicted results to the experimental results.

We also evaluate the laser in communications performance through optical heterodyne experiments. These experiments require the use of a tunable filter. Available filters required a longer operating wavelength, and as a result, a 1550 nm SOA is used.

Finally, we make arguments to improve the laser performance. A final iteration of the laser is built near the 1310 nm wavelength with attempts to optimize the design and laser output, and the same analysis from the first iteration is applied to the improved laser.

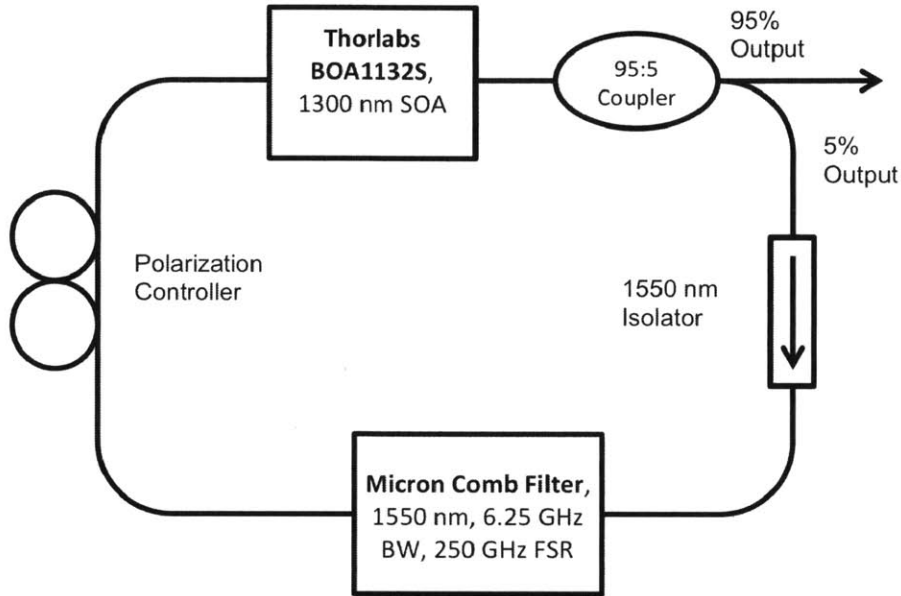## 2.1 Laser Component Characterization

2.1.1 Laser Structure

Figure 2-1: Illustration of basic fiber ring laser structure. The laser cavity is made with an semiconductor optical amplifier (SOA) gain medium, filter, isolator, output coupler, and polarization controller.

The multiwavelength ring laser is first characterized by measuring and analyzing its discrete parts. The structure of the laser is shown in Figure 2-1. This section will discuss a first iteration of the laser design which uses a semiconductor optical amplifer gain component with a combination 1550 nm passive devices. All components of the cavity have single-mode fiber pigtails with FC/APC connectors, and the total length of the cavity is approximately 11.82 m. The following subsections will discuss the individual devices in detail.

2.1.2 Semiconductor Optical Amplifier (Thorlabs BOA1132S)

The SOA used in the first iteration of the multiwavelength ring laser is an O-Band Booster Optical Amplifier from Thorlabs (BOA1132S); a quantum well, ridge waveguide structure made of InP/InGaAsP gain medium. It has a typical center wavelength

of 1300 nm and, for a seed wavelength of 1312 nm, has a saturation output power at -3 dB of 18.9 dBm. The maximum current is 600 mA with a typical noise figure of 7 dB [24].
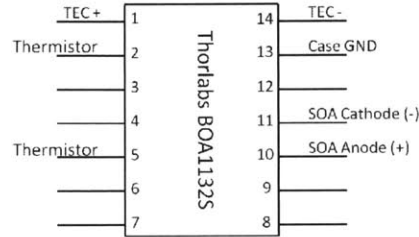

Figure 2-2: Pinout diagram of BOA1132S 14-pin butterfly package. The SOA package was used with a Newport 7400 diode mount and Newport 8000 Laser Diode and Temperature Controller.

The gain at low currents was measured for predicting threshold current later. For this measurement, a TSL-21OF full-band tunable laser from Santec was used as the input source. The Santec laser has a wavelength range of 1260-1630 nm and a step resolution of 0.01 nm. The Santec laser is input to an Agilent 11896A Polarization Controller and then to a 90:10 coupler. The output power of the 10% port of the coupler is measured with a Hewlett Packard 81532A Power Sensor. The 90% port is then passed to the input of SOA. The SOA output is connected to another Power Sensor.
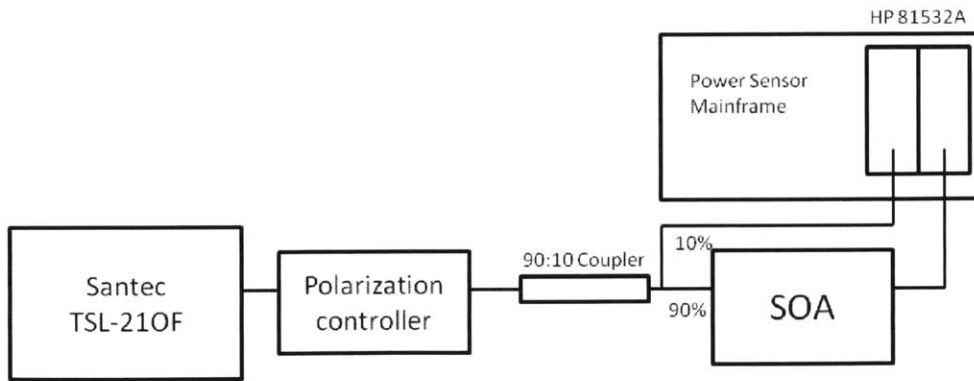
Figure 2-3: Measurement equipment and setup for measuring loss and gain in devices. The figure shows the SOA in the measuring path, but this arrangement was used for transmission measurements of all laser components.

The power sensors are designed to be housed in a source meter mainframe which

displays the measured power. Using a Hewlett Packard 8153A Lightwave Multimeter, the measurement is calibrated by first connecting the 90% output power directly to the second power sensor and applying a dB power offset to the first power sensor until the power difference between the first and second sensors is equal to 0±0.2 dB. Thus, if we reinsert any device into the 90% path, the difference will show the device loss or gain.

To plot the gain as a function of wavelength, the input seed laser was set at an output power of -10 dBm. The laser was swept from 1330 nm to 1350 nm in steps of 0.01 nm. The gain at each step is recorded, and the results are saved as a .mat file for analysis in MATLAB. This is initially performed for currents in the range of 30-40 mA. The results are shown in the figure below.
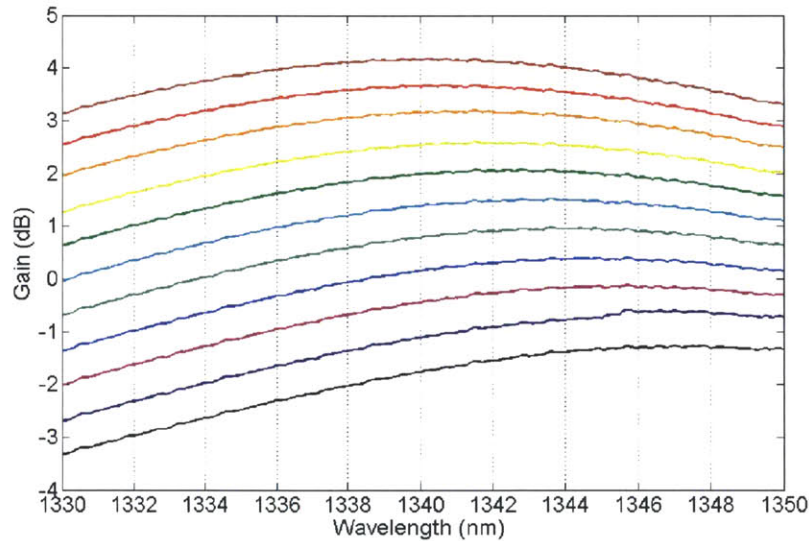
Figure 2-4: SOA gain curves as a function of wavelength for bias currents of 30-40 mA with seed lasing power of -10 dBm.

2.1.3 Fabry-Perot Filter

Selection of the filter in our system decides the minimum free spectral range of the multiwavelength laser. We used a 1550 nm Fabry-Perot Interferometer from Micron Optics with a free spectral range of 250 GHz and a filter bandwidth of 6.25 GHz.

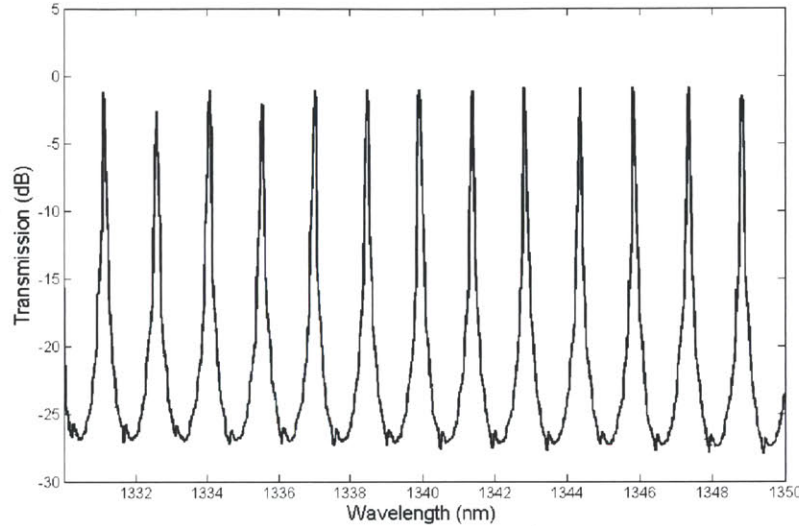Since the SOA is operating in the O-band, the filter losses are measured using the

Figure 2-5: The 1550 nm center wavelength filter transmission output with FSR = 250 GHz and bandwidth = 6.25 GHz. The measurement is limited somewhat by the tunable laser resolution, and thus the peaks appear to be uneven.

setup in Figure 2-3 but replacing the SOA with the filter. Figure 2-5 shows the loss of the fiter around 1340 nm wavelength. The filter performance suffer very little in this range with an average loss of about 0.5 dB. We note that the Santec TLS-21OF tunable laser has a limited resolution of 0.01 nm and that the peaks are expected to have nearly identical heights in this range.

2.1.4   Coupler, Polarization Controller, and Isolator

In a ring laser, the output coupler plays the role of etalon mirrors. In this first iteration setup, we used a 95:5 coupler with the 5% port as the system output allowing for 95% of the SOA output to recirculate. However, the device is designed for 1550 nm wavelength; thus we cannot assume the split ratio is perfectly 95:5 since we are operating in the 1310 nm range. We would expect the loss through the 5% port in the ideal case to be about -13.01 dB, but when measured under the worst polarization conditions at 1340 nm wavelength, it is as high as -14.51 dB. This corresponds to a

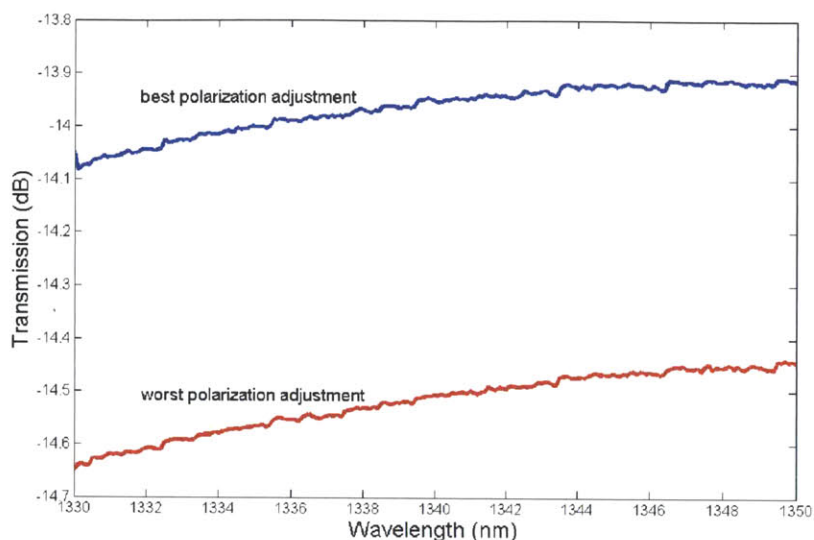coupling ratio of 96.5 to 3.5.

Figure 2-6: The coupler loss through the 5% port was measured twice: once for polarization setting that minimized loss and once for a setting that maximized loss. At a wavelength of 1340 nm, the coupler losses range from -13.95 dB to -14.51 dB compared to an expected loss of -13.01 dB for an ideal 95:5 coupler.

Since the SOA has polarization dependent loss and thus has an optimal input polarization orientation, a polarization controller is placed behind the SOA. The controller is a simple paddle controller with long SM fiber wrapped in loops. The paddles twist the fiber to rotate the polarization. As will be addressed later, the polarization plays a significant role in the output behavior of the laser.

Because of the the unidirectional output, an isolater is used to extinguish backwards propagating waves that contribute to saturating the gain but cannot be coupled out. The isolater used in the system is designed for 1550 nm. The forwards and backwards losses are shown in Figure 2-7 for both 1340 nm and 1550 nm bands. The loss in the forward direction increases by about 1.3 dB. However, the greatest change is in the extinction, where the isolator performance at 1340 nm degrades by about 40 dB. This is far from ideal for an isolator, but we assume that a directional loss difference of 17.5 dB will be large enough so as to not load the gain in the backwards direction.

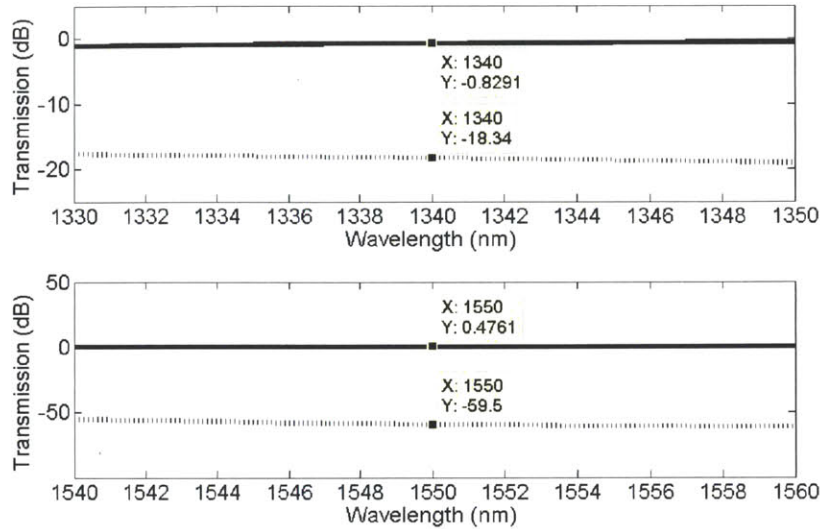Finally, the total losses are shown in Figure 2-8. We show the losses contributed

Figure 2-7: Isolator forwards and backwards transmission for center wavelengths of 1340 nm and 1550 nm. Though the losses in the forward direction suffer by less than 2 dB, the extinction drops by at least 40 dB.

by the isolator, the coupler, and the filter. The summed losses of the three elements are then compared to the loss measured through the entire cavity in Figure 2-1 unwrapped sans SOA. We will use the latter measurement for predicting threshold and differential efficiency. Near the wavelength 1340 nm, we find that the total internal loss is approximately 2.61 dB, which expressed as a transmittance is equal to 0.548.

2.2 Predicting Laser Characteristics

From the losses and gain curves, we can try to predict the lasing characteristics that were experimentally determined. For the following sections, we treat the system as if it were lasing single mode. Experimentally, it is possible in the actual multiwavelength ring laser to encourage single mode lasing through adjustments in the polarization. A polarization condition must be met to achieve minimal losses in the cavity; that is, the polarization needs to be tweaked in a trial-and-error fashion until wavelength-dependent losses with mode competition make the system selective for a single mode. It is at this operating point that the LI curve is measured and compared to the

37

predicted laser parameters.

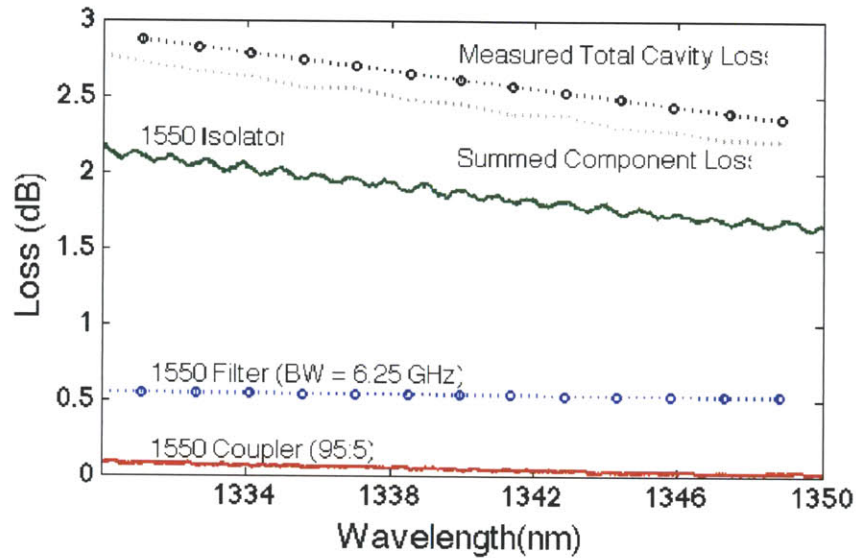## 2.2.1   Threshold Current and Lasing Wavelength

Figure 2-8: Loss measurements for the isolator, coupler, and filter. The summed losses of the three components are shown together with the loss through the complete connected cavity.

The threshold current and lasing wavelength were predicted by examining the point at which the SOA gain curves intersects with the total cavity losses. From the gain and loss measurements, the lasing wavelength is predicted to be between 1342 and 1344 nm with a threshold current of about 37 mA. However, it should be noted that polarization easily could change lasing wavelength and threshold current on a wide range. Figure 2-10 shows the effects of polarization on the SOA gain for two bias currents: 34 mA and 38 mA. We see not only a significant difference in the gain for the same bias current but also a change in shape which would effect the lasing wavelength as well.
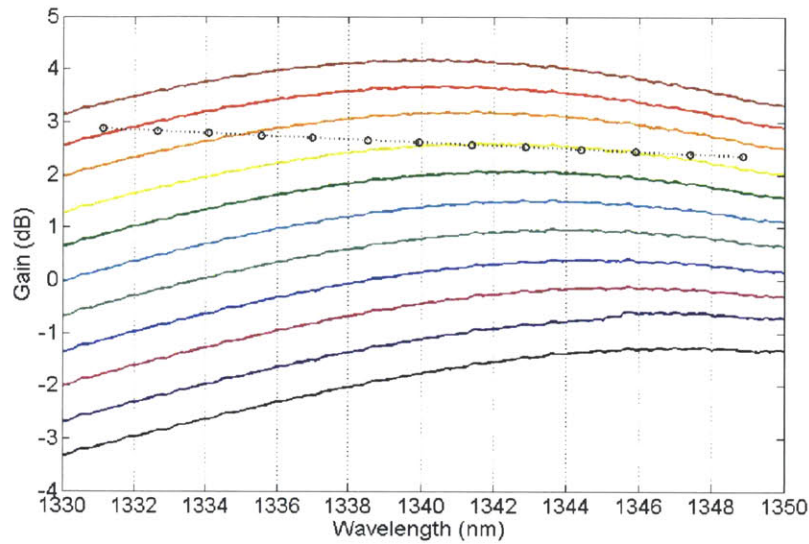
Figure 2-9: The loss measurement from Figure 2-8 is plotted on top of Figure 2-4 to find the lasing wavelength and threshold current. The plot shows that the lasing wavelength is between 1342 nm and 1344 nm and that the threshold current is about 37 mA.
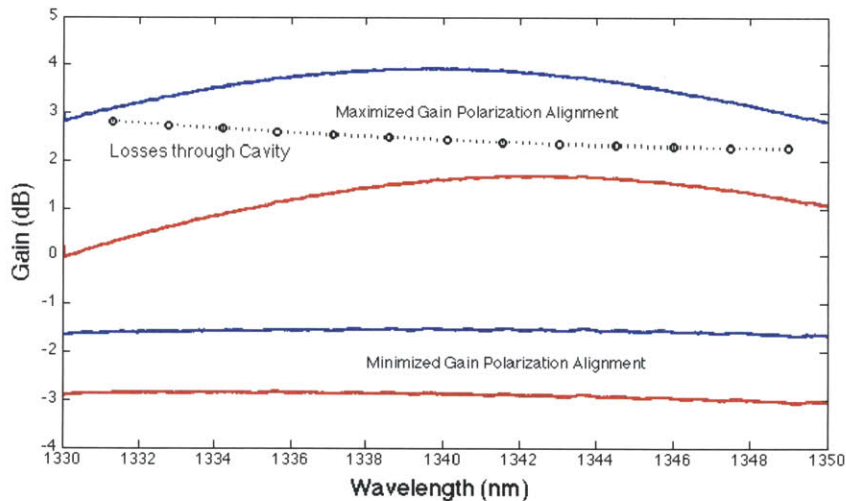

Figure 2-10: The effect of polarization on gain can be large. The blue curves are both the SOA gain at a bias current of 38 mA while the red curves are set at a bias current of 34 mA. The range of gain is for the 38 mA case is -1.5 dB to 3.9 dB.

2.2.2 Differential Efficiency

The differential efficiency is determined using Equation 1.21. In the multiwavelength ring laser, the measure of photons that stay in the cavity versus those that leave

39

the cavity is expressed in the coupling ratio. As discussed in Section 2.1.4, the transmittance is calculated from the measured loss as 0.965. Using Equation 1.15, $\alpha_m L$ is calculated . In addition to the coupler loss, the total cavity transmittance T_i is also necessary to calculate η_d as well as the internal quantum efficiency η_i which for now is assumed to be 0.8. From these values, we predict a differential efficiency of 4.55%.

2.3 Observation of Laser Output

This section discusses some of the initial observations of the multiwavelength ring laser performance. With the laser assembled, an optical spectrum analyzer is used to observe the comb shape of the output as well as the effects of polarization. A microwave spectrum analyzer is viewed to determine the effects of the cavity resonances due to the long cavity length. Finally, using the optical spectrum analyzer, we take our first steps in characterizing the laser by plotting the LI curve.

2.3.1 Optical Spectrum

The laser output was observed on an HP 7095B Optical Spectrum Analyzer. Adjustments to the polarization can change the output spectrum significantly from the center wavelength to to the total number of modes lasing. More interestingly, the polarization can be adjusted so that the spectrum can be swtiched between multimode and single mode lasing.

The power measurements used with the OSA also needed to be calibrated. Using again the TSL-210F laser, the input power was set, then measured first with the OSA then with a power sensor. It was also noted that the power measured by the OSA at even a larger resolution bandwidth of 1 nm differed from a power tap measurement by 1.02 dB was measured. As a result, all power measurements have a 1.02 dB calibration offset added to the results.

40

(a) I = 38 mA   (b) I = 82 mA

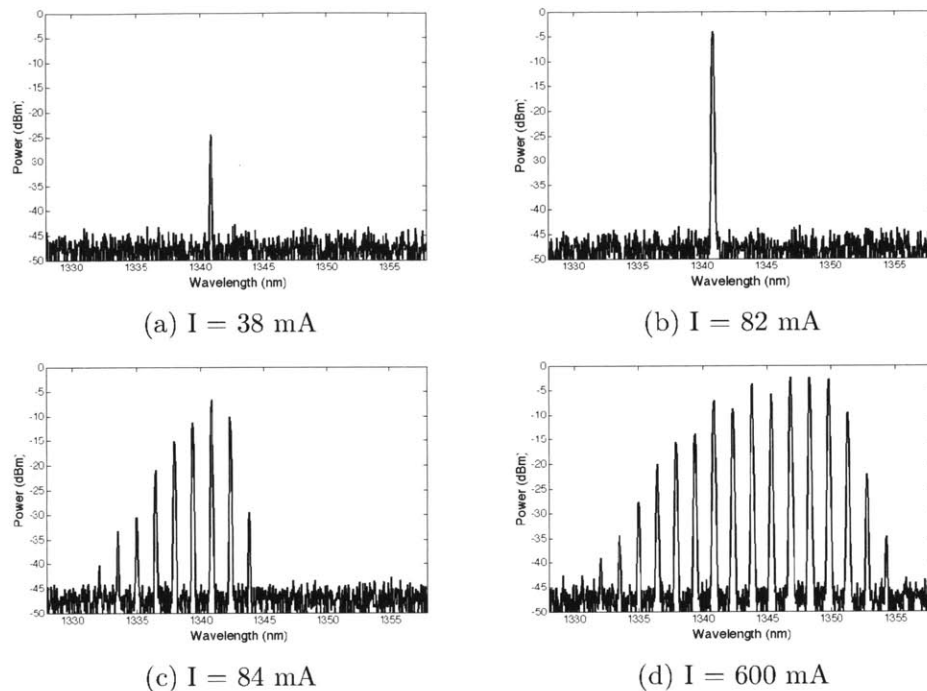(c) I = 84 mA   (d) I = 600 mA

Figure 2-11: Optical spectra taken at different current values. The laser experiences a dependable transition from single wavelength in Figure 2-11b to multiwavelength Figure 5-9b given that the polarization is unchanged.

2.3.2 LI Curve

The threshold current, lasing wavelength, and differential efficiency were determined experimentally through analysis of optical spectra. The ring laser was constructed and the output was viewed on an Optical Spectrum Analyzer. By adjusting the polarization, the laser could be made to lase single filter resonance for a large range of bias currents starting from threshold. It is in single mode operation that the LI curve was obtained.

Using a Newport 8000 Model Laser Diode and Temperature Controller, the bias current was stepped in 0.5 mA divisions from 35-60 mA while the temperature of the package was held at 20 C°. At each step, the optical spectrum is recorded. The spectra are then compiled into a matrix array, and analyzed in MATLAB. By using a peak detection function, the resulting peak powers are plotted as points. It can be seen by the gray points in Figure 2-12 that the laser was likely to lase in multimode at
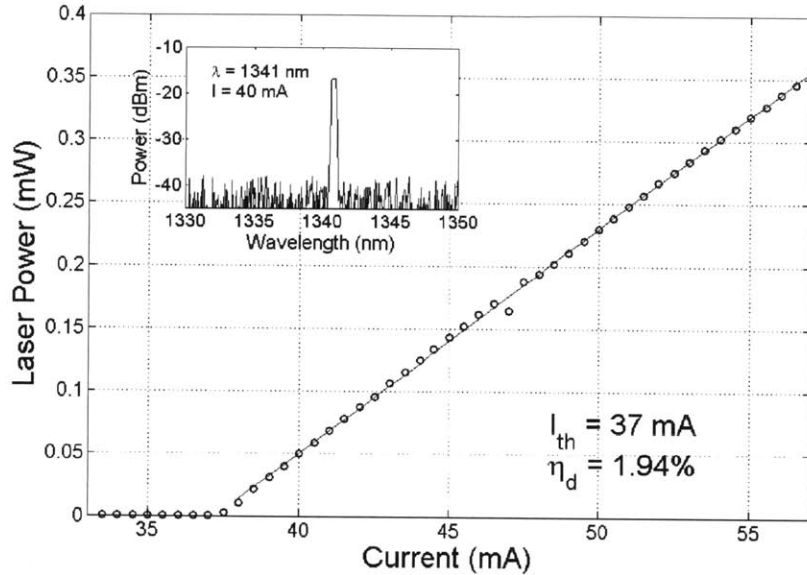
Figure 2-12: The LI curve was collected using the optical spectrum analyzer. After plot the peak powers and plotting a best fit line (shown in gray), the calibration offset is applied to give the final curve (shown in blue). The lasing wavelength shown in the smaller graph is approximately 1341 nm.

higher currents. The points that showed linear behavior were used to draw a best fit line. The resultant line is then adjusted according to the OSA calibration offset. All of this information can be seen in Figure 2-12. Viewing the plot, the threshold current is 37 mA, and the differential efficiency after calibration is 1.94% and corresponding wall-plug efficiency for 0.35 mW of output power of 0.67%.

Compared to the measured results, the threshold prediction of 37 mA matches the experiment, but the measured differential efficiency is off by an error of 57%. However, we had neglected the noise figure of the SOA in our calculations. The noise figure can be expressed in dB as follows

$$NF_{dB} = SNR_{in} - SNR_{out} \qquad (2.1)$$

In a shot-noise limited detector, the ideal ampifier has an SNR (signal-to-noise ratio) of 3 dB. However, a typical SOA has coupling and waveguide losses captured in the noise figure. Thus for a noise figure of 7dB, we obtain that the SNR at the output is

-4dB. We can express this as a transmission or inherent SOA efficiency of $\eta_{SOA} = 40\%$.

Including this in our calculations, we predict a differential efficiency of 1.82% with an error of 6.5%. We note this uses the absolute worst case polarization losses through the coupler of -14.5 dB. Our experimental results imply the coupler loss at the drop port is -14.2 dB which is within the measured range. Using this value of loss instead, we can reduce our error to 0.3%.

2.4 Optimizing Laser Wall-Plug Efficiency

To find the wall-plug efficiency for a target optical power, we rewrite Equation 1.22 to find an expression for the bias current I since the optical power P_{opt}, the differential efficiency η_d, and the threshold current I_{th} is either given or can be calculated.

$$P_{elec} = \frac{P_{opt}}{\eta_d} + \left(\frac{h\nu}{q}\right) I_{th} \tag{2.2}$$

The threshold current is found by first finding the threshold gain G_{th} using Equations 1.12 and 1.19. The threshold current is then found from the threshold gain using the logarithmic fit from Equation 1.18

$$I_{th} = I_0 \exp\left(\frac{G_{th}}{G_0}\right) \tag{2.3}$$

Relating the gain and bias current from measured data points shown in Figure 2-13, I_0 and G_0 are found through the fitting to be 30 mA and 16.284 dB respectively. The experiments show a maximum output power of 0.35 mW before the laser becomes multiwavelength. At this output optical power, we obtain a wall-plug efficiency of 0.67 %. For an optical output power of 1 mW, the wall-plug efficiency of the multiwavelength ring laser is 1.18%. For an optical power of 10 mW, the efficiency improves to 1.82%.

To improve the wall-plug efficiency, the coupler transmittance ratio can be modified to couple more photons to the output. We also see from Equation 2.2 that both the threshold current and the differential efficiency are functions of the mirror loss.
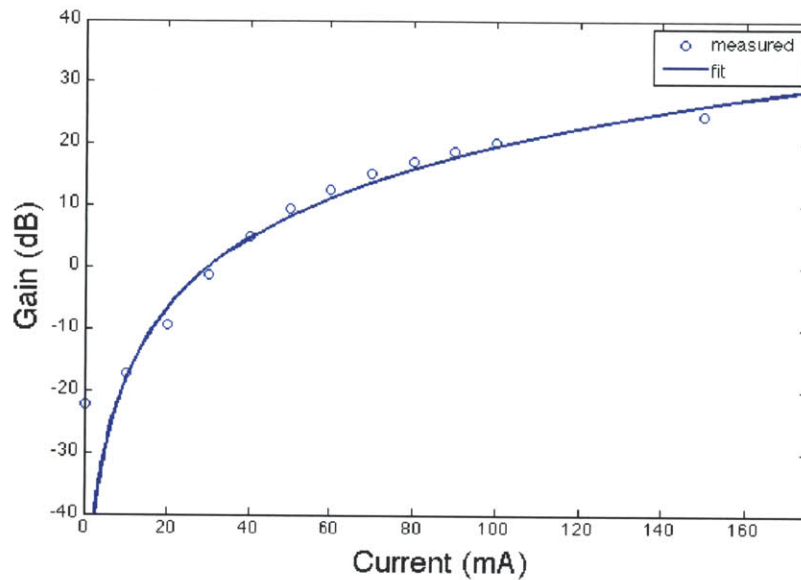
Figure 2-13: The gain as a function of current was found using a logarithmic fit with $I_0 = 30$ mA and $G_0 = 16.284$ dB.

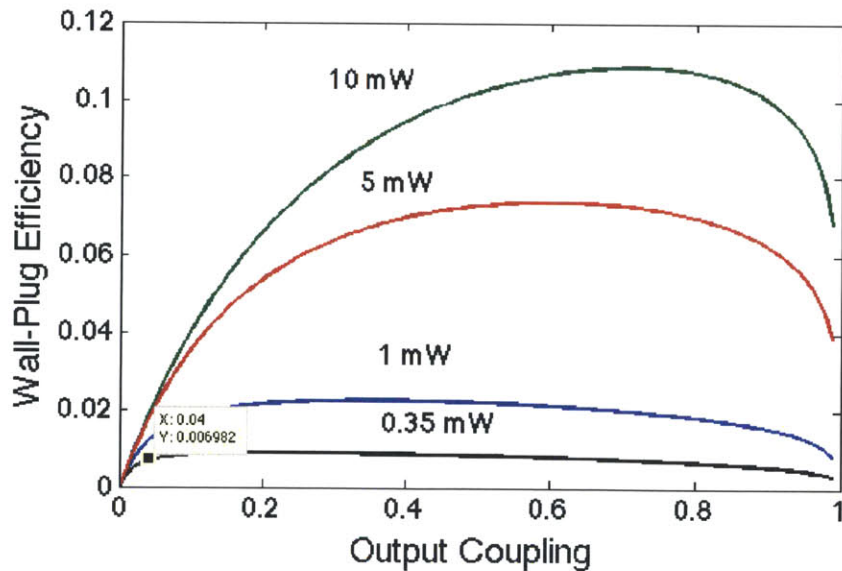Figure 2-24 shows the wall-plug efficiency as a function of the coupling ratio for our

Figure 2-14: Wall-plug efficiency for optical output powers of 0.35 mW, 1 mW, 5 mW, and 10 mW as a function of coupling ratio. The efficiency improves as the coupling ratio moves towards 50:50 for higher output powers.

experimentally confirmed output power of 0.35 mW as well as for 1 mW, 5 mW,

and 10 mW. The model shows that the wall-plug efficiency improves not only with increasing optical power but also with a more evenly split coupling ratio. Clearly, a low output coupling ratio is keeping the WPE to lower than 2% even at a high output power of 10 mW.

2.5 Microwave Spectrum

In addition to observing the optical spectra, it is important to analyze the laser microwave spectra in order to determine its usability as a communications laser. An Agilent 74100 Microwave Spectrum Analyzer was used to view the spectra. In addition, to simulate the laser operation on a photonic integrated circuit, it was also required to filter one of the wavelengths of the laser comb and assess its performance individually. In order for the ring laser to be usable for link communication, each mode would ideally behave like a single mode laser when filtered. As a result, a tunable optical filter was required. As only a 1550 nm MEMs voltage-controlled tunable filter was available, for the following measurements, a 1550 nm JDSU SOA was used. Due to the center wavelength shifting to longer wavelengths, optical spectra were collected using a Yokogawa AQ6370 OSA.

To analyze the laser performance in optical heterodyne, the output of the laser was observed in the MSA under three conditions: multimode, filtered multimode, and single mode.

Filtered Laser Comb We begin by showing the optical spectra for the laser before and after filtering. The filter was tuned to select the 1604 nm wavelength. Figure 2-16b shows that the filter suppresses the strongest side mode by 25 dB. The filtered output is then modulated using an Avanex 10 Gb/s LiNbO3 modulator.

Observation of the filtered mode output as shown in Figure 2-17 indicates the significant presence of noise. Because the modulation frequency peak is not visible, the laser would not be suitable in a communications application. Changing the modulation frequency from 100 MHz to 110 MHz changes the microwave spectrum quite
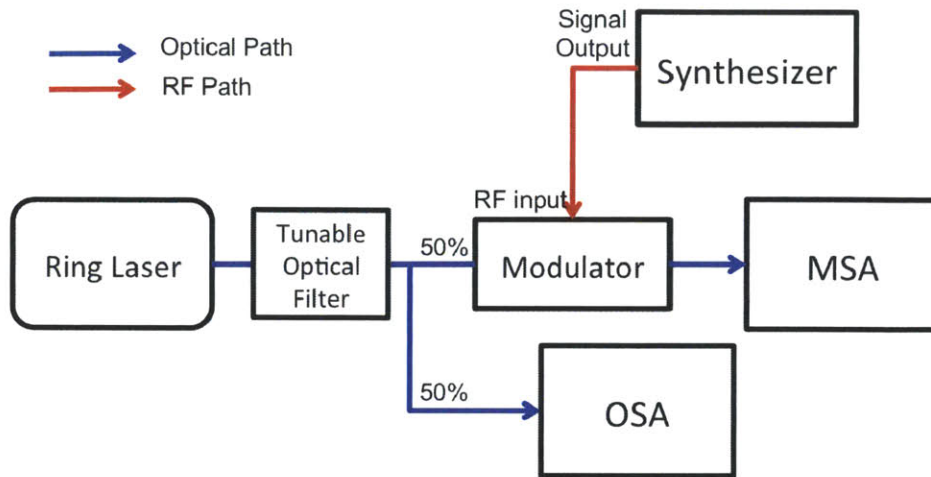
Figure 2-15: Diagram of microwave spectrum measurement. The laser output is filtered to select a single wavelength output. This is confirmed with 50% sent to an OSA. The other 50% is modulated with a modulator driven by a sine wave from a synthesizer, and the modulator output is observed on the MSA.

drastically. This leads us to conclude that the beat notes seen on the microwave spectra are spaced approximately 15 MHz apart, and the 100 MHz modulation experiment showed the beat spectrum convolved around 100 MHz and its harmonics. Based on the measured cavity length of 11.82 meters, the predicted mode spacing is 17.3 MHz assuming fiber effective index of 1.47, thus consistent with the observed beat note spacing.

For comparison, the polarization controller in the laser was adjusted to induce single mode operation. The output of this laser was modulated and observed on the MSA. As shown in Figure 2-18, the laser appears to be operating as truly single mode based on the lack of noise.

For completion, the multimode output was also modulated at 110 MHz viewed on the MSA. The results are shown in Figure 2-19. The noise is present, but reduced to the point where the modulation frequency is discernible.

The conclusions from the multimode and filtered multimode measurements show the presence of approximately 15 MHz spaced beat notes whereas for a stable single mode case, there were no beat frequencies. We conclude that the beat frequency spacing is a result of the cavity resonances, and that in multimode operation, each
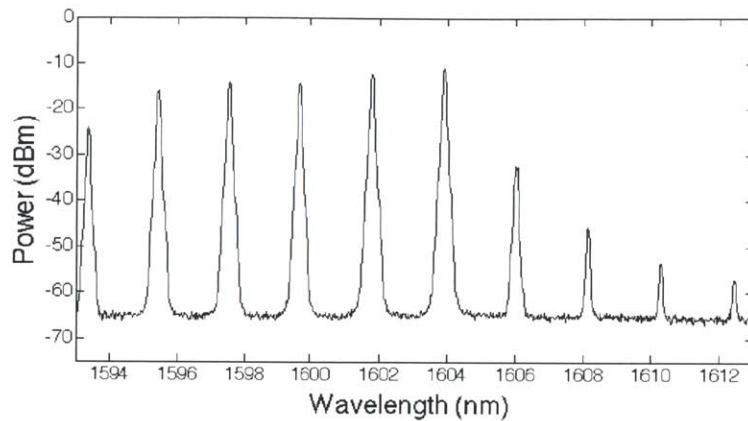
(a) without fiter
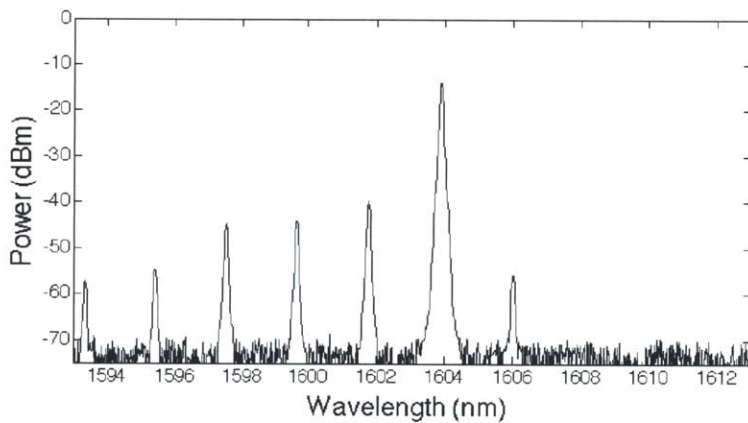
(b) with filter

Figure 2-16: Optical spectra of the 1550 nm ring laser multiwavelength output before and after optical filter.

filtered peak is a separate multimode laser.

When the laser is in single mode operation, we can conclude that the output is indeed purely single mode. As this is a result of polarization adjustment, the possibility for this behavior is that in certain polarization conditions, one mode completely is able to dominate and suppress side modes thus leading to a single mode output. In other conditions, the competition is more even, and as the modes are competing for the available power, what results is a beating electrical signal as a result of the cavity resonances.
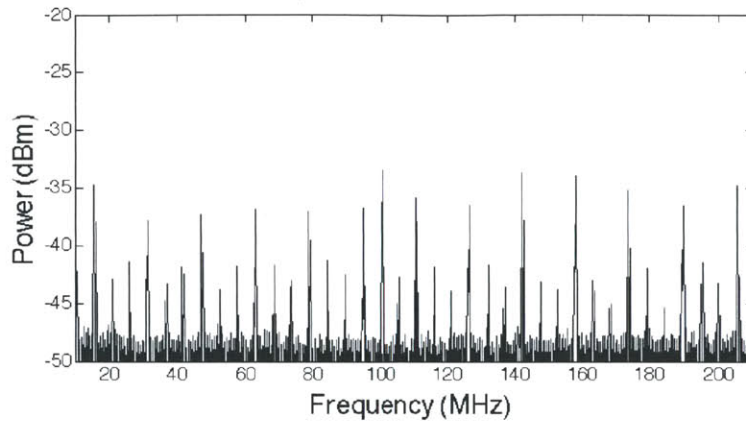
(a) $f_{mod} = 100$ MHz
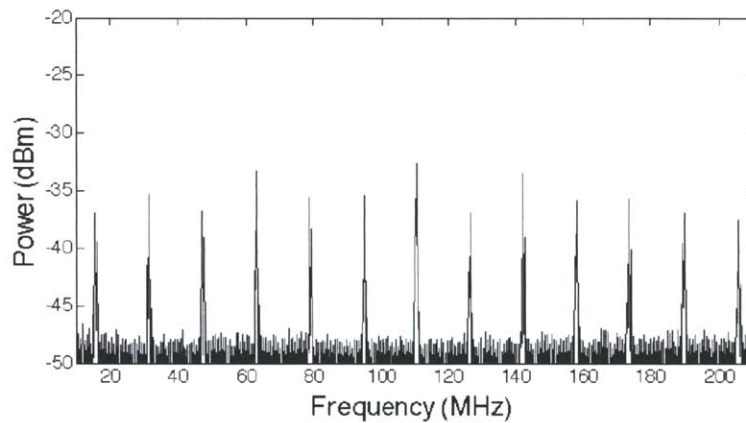
(b) $f_{mod} = 110$ MHz

Figure 2-17: Microwave spectra of 1550 nm filtered multiwavelength laser output modulated at 100 MHz and 110 MHz

2.6 Improving Laser Performance

Based on the results of Sections 2.4 and 2.5, iterations of the laser using components and conditions selected to improve laser efficiency and noise performance were built and characterized.

Particularly, a new Fabry-Perot filter from Micron Optics was obtained for the following experiments. The new filter was requested to be designed for the 1310 nm wavelength range as well as for a higher finesse of 1000 pertaining to a much narrower bandwidth of 150 MHz and smaller free spectral range of 150 GHz. The resultant filter bandwidth cannot be resolved with measurements using the Santec laser, and
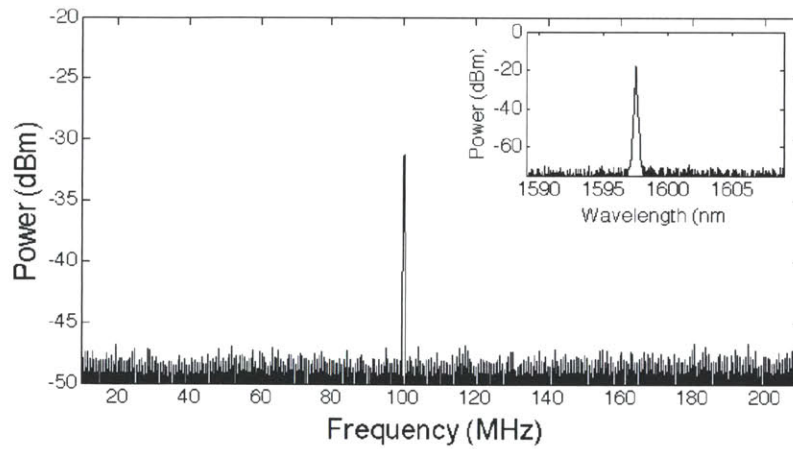
48

Figure 2-18: Microwave spectrum of multiwavelength laser with filtered wavelength modulated at 110 MHz.
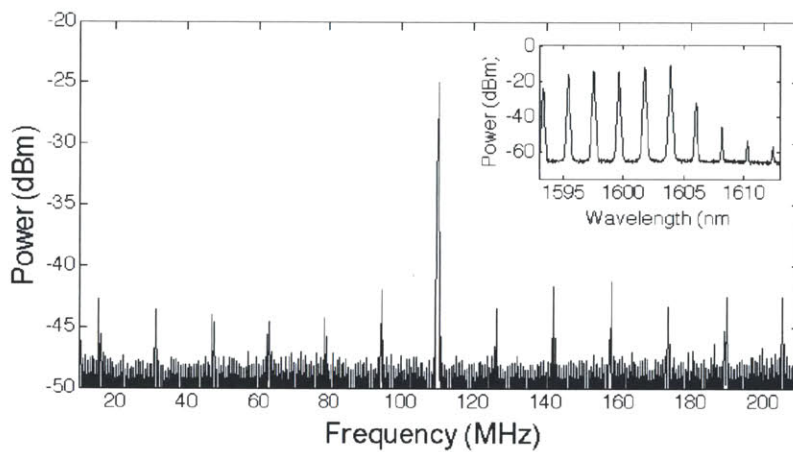

Figure 2-19: Microwave spectrum of multiwavelength laser with all wavelengths modulated at 110 MHz.

the setup shown in Figure 2-3 could not be used to determine the loss of the filter. Instead, a constant loss of 3.5 dB was assumed based on the measured loss of 3.5 dB at 1310 nm as indicated in the datasheet.

2.6.1 Improved Efficiency

First, a laser with better efficiency was built with the aim of lowering internal losses of the components. In addition, the coupling ratio was reduced to 50:50. Specfically,
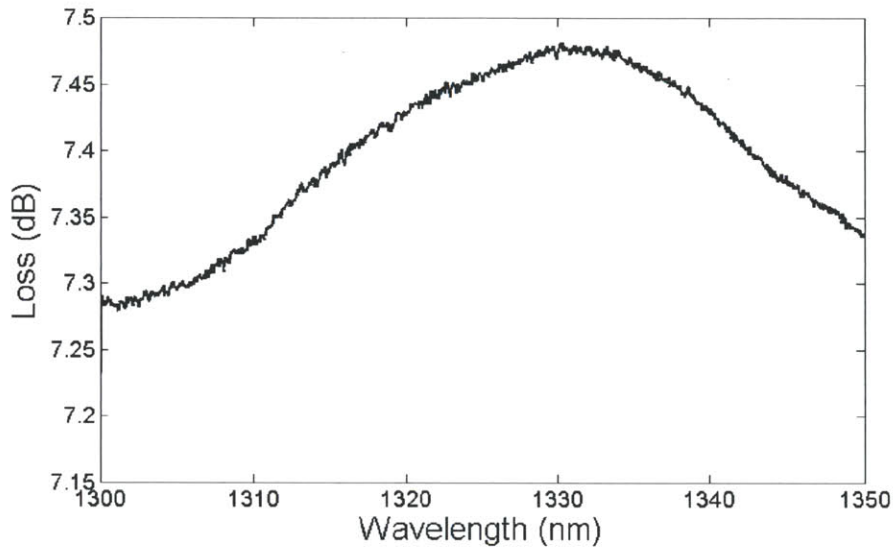
49

a 1310 nm isolator and 1310 nm 50:50 coupler from Thorlabs and a 1310 nm 150 MHz Fabry-Perot Filter from Micron Optics were selected for this design.
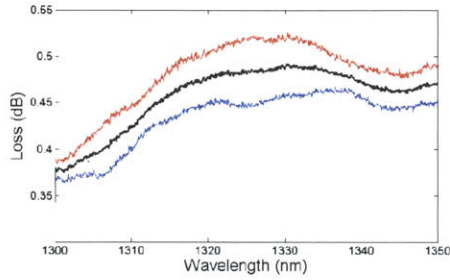
(a) Thorlabs 1310 nm Isolator
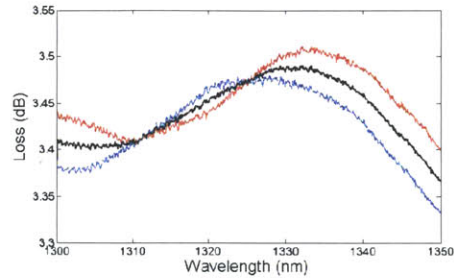
(b) Thorlabs 1310 nm 50:50 Coupler

(c) Summed losses of isolator, coupler, and 1310 nm Micron Filter.

Figure 2-20: Losses in the improved iteration of the ring laser. (a) The 1310 nm isolator loss is measured at high and low polarization dependent loss (PDL), shown in red and blue respectively. The black curve shows the average loss of the isolator. (b) The 1310 nm 50:50 coupler is similarly measured at high and low PDL and the result is averaged and shown in black. (c) The total summed losses of the cavity includes the average loss of the filter given by Micron Optics as 3.5 dB at 1310 nm.

Losses and Slope Efficiency Prediction The isolator loss shown in Figure 2-20a has a maximum loss of 0.49 dB near 1331. The loss was determined by measuring the isolator loss at high and low polarization dependent losses (PDL) (shown in Figure 2-20a as red and blue curves respectively). The two curves were averaged to

produce a wavelength dependent curve for the isolator loss.

The loss of the coupler was found through the same exact means used to find the isolator loss by first finding the curves at high and low PDL then averaged. The through port loss is 3.5 dB at its peak near 1335 nm resulting in a transmission percentage of 55.3%. The drop port is correspondingly 44.7% transmission or 2.57 dB of loss.

To find the total loss of the cavity, the sum of the isolator and coupler losses are offset by 3.5 dB representing the filter loss. The results show that the internal losses of this laser iteration are in fact higher than the first iteration due to the increased losses in throughport of the output coupler and the FPF. We anticipate that this will increase the threshold current, but the lowered coupling ratio should play a larger role than the internal losses in improving the slope efficiency.

Given these values, we make a prediction the slope efficiency. Based on the results from Section 2.2.2, we again make the assumption that the quantum efficiency of the optical amplifier is 0.8 and that the SOA has an inherent efficiency of 40%. The total internal loss at 1335 nm is approximately 7.5 dB and the loss through the drop port of the coupler is 2.57 dB. We calculate a differential efficiency of 10.3%.
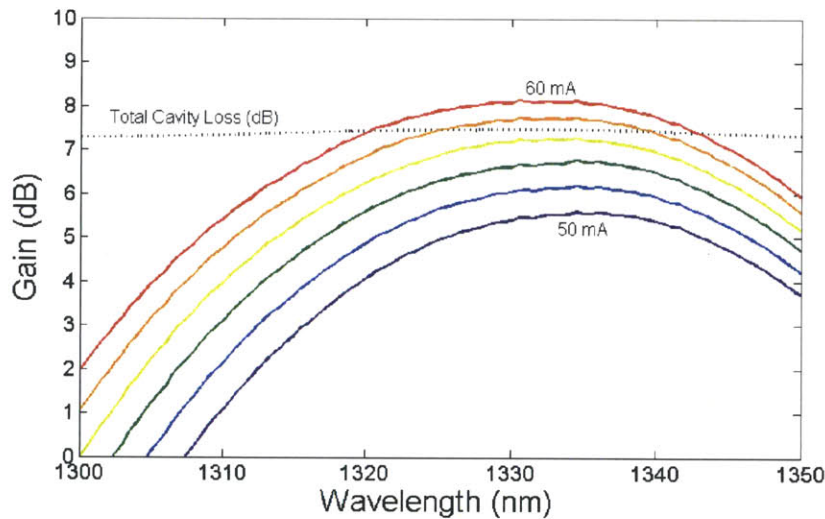

Figure 2-21: Gain curves of Thorlabs 1132 SOA showing gain for 1300-1350 nm wavelength span for bias current of 50-60 mA

Gain Curves The SOA used in this experiment is the Thorlabs BOA1132S from the first iteration. However, because of the higher losses in the cavity, the gain curves were measured at higher bias currents. The results are shown in 2-21 and predicts a threshold current of about 57 mA. The lasing wavelength can also be estimated near 1335 nm. Again, it is noted that the gain shape and magnitude is very polarization dependent.

(a) I = 60 mA
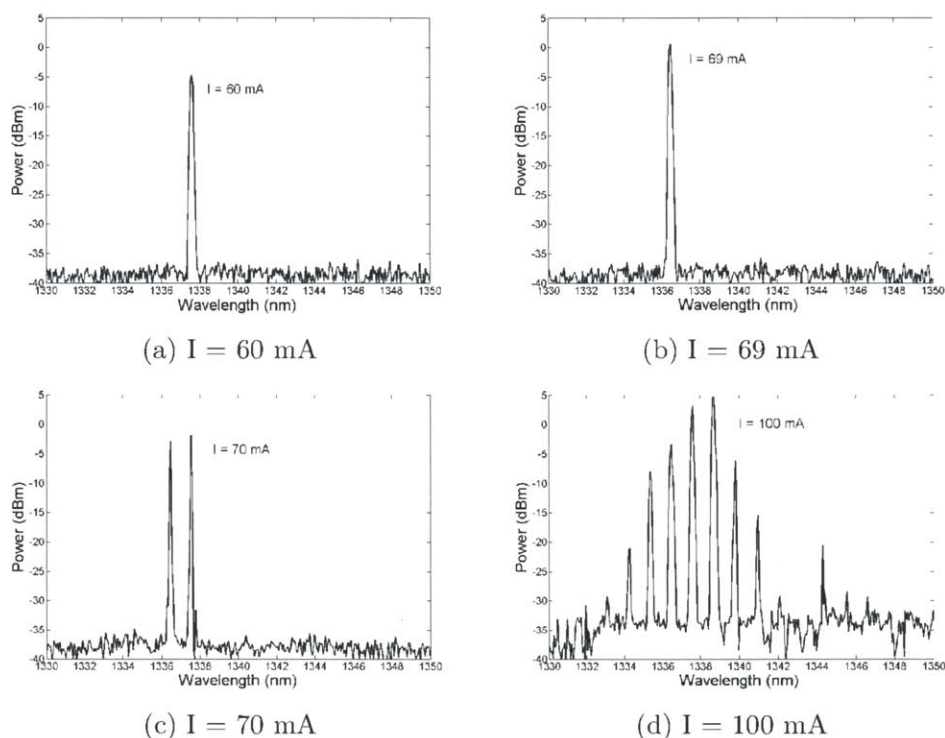
(b) I = 69 mA

(c) I = 70 mA

(d) I = 100 mA

Figure 2-22: Optical spectra of second iteration of laser taken at different current values. The laser again transitions from single wavelength to multiwavelength at increasing bias currents. However, the transition was less dependable and the laser output seemed generally less stable.

Optical Spectra and Laser Behavior Observation of the laser spectra on the OSA shows more unstable behavior than its previous iteration. Comparing Figures 2-22a and 2-22b show that though the laser is in single-mode operation in both bias currents, the wavelength is not the same in the two spectra indicating that the laser is mode-hopping. Furthermore, it was more difficult to maintain single-mode operation

at low bias currents as indicated in Figure 2-22c whose bias current differs from that of Figure 2-22b by 1 mA. The multiwavelength spectrum shown in Figure 2-22d also looks decidedly less clean than the multiwavelength spectrum from the previous laser iteration shown in Figure 2-11d.
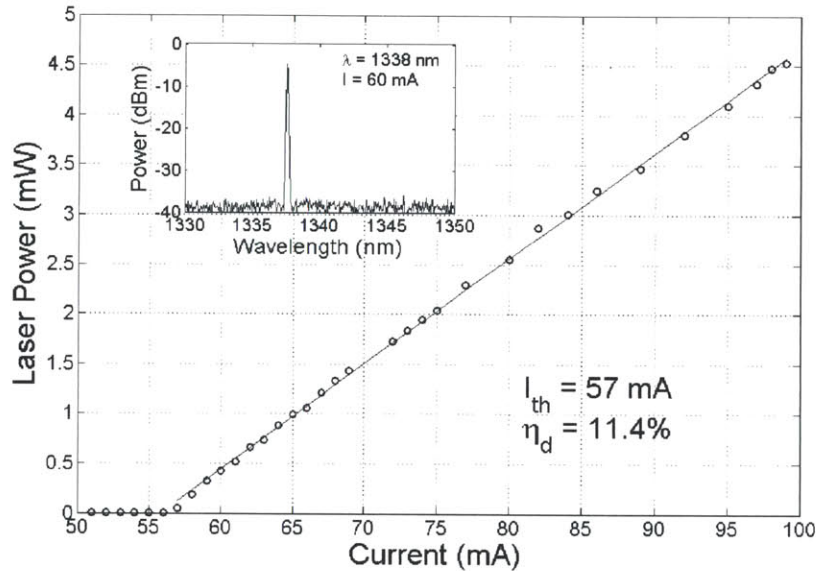

Figure 2-23: Plotted LI curve of 1310 nm laser. Threshold current occurs at 57 mA, matching prediction. The differential efficiency is 11.7% and smaller than predction.

LI Curve and Slope Efficiency   In order to plot the LI curve, the unstable behavior must be considered and the plot adjusted accordingly. The peak powers of all the spectra were plotted as points. Points that did not fit a linear slope were confirmed to be in multimode operation by matching to the spectra index and thrown out. The remaining points were confirmed to show single-mode spectra and used to plot the curve.

Figure 2-23 shows the curve and lasing wavelength. The threshold occurs at 57 mA which matches our prediction with a lasing wavelength that comes close. However, recall that the lasing wavelength was not stable. The slope efficiency is calculated for $\lambda = 1340$ nm as 11.4% showing a significant improvement from the first laser differential efficiency of 1.94%. Compared to our prediction, we are off by 10.9%,

but we note that our experimental efficiency is higher than what we have predicted. It is possible that we have introduced losses inadvertently through measurement, or we are observing polarization dependent losses. Reducing our losses by just 0.3 dB already brings us down to 7.9% error.
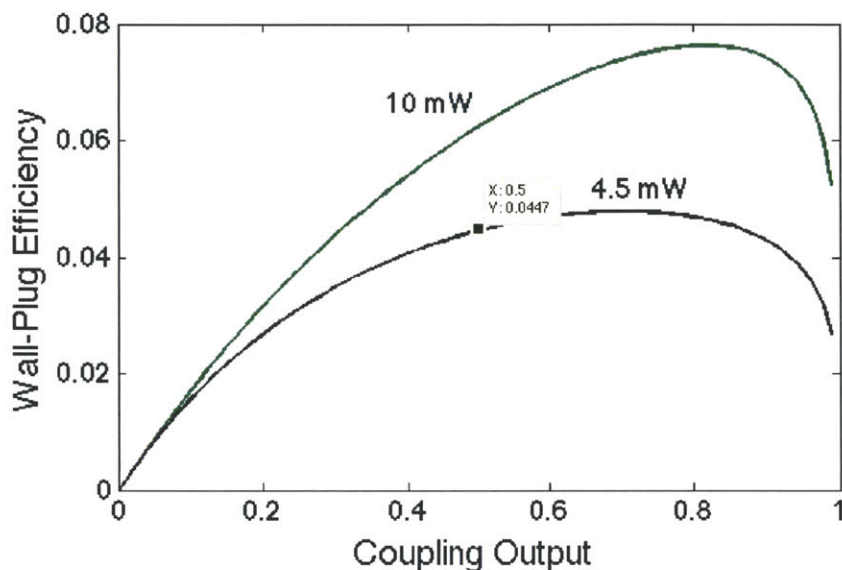

Figure 2-24: Wall-plug efficiency for optical output powers of 4.5 mW and 10 mW as a function of coupling ratio.

Based on these results and an output power of 4.5 mW, the wall-plug efficiency of the laser is calculated for an output power as 4.9%. Increasing the output power to 10 mW pushes the WPE up to 7.1%. We have already increased the WPE from the first to second iteration by 700%.

2.6.2 Improved Noise Performance

The second aspect of improvement deals with the noise on the microwave spectrum. From Section 2.5, it was stated that the 15 MHz spaced modes are likely the ring cavity resonances. We also found that modulation at different frequencies would appropriately lead to the unmodulated microwave spectrum convolved over the modulation frequency and its higher harmonics. Based on these results, it was concluded that finding a means of increasing gain homogeneity on the scale of the cavity res-

onance FSR and gain inhomogeneity on the scale of the filter FSR was important for reducing noise. We modified the laser without changing the gain in the following ways.

Decreasing Filter Bandwidth As mentioned above, the new Micron Filter has a much narrower bandwidth of 150 MHz. This limits the number of modes under a single filter peak which we hypothesize will be an advantage because of reduced competition.

Increasing Fiber Ring Free Spectral Range In Section 2.5, the cavity was measured to be of a significantly long length. By reducing this length, the cavity FSR is increased and artificially increases gain homogeneity on the cavity scale. It also reduces the number of modes contained under a single filter peak.

Ideally, reducing cavity length by 10× would give a cavity mode spacing of 150 MHz which perfectly fits the bandwidth of the new Micron Filter. Unfortunately, this requires the cavity to be a total length of 1.1 m. Each filter component has fiber pigtails approximately 2.2 meters in length. For the sake of preserving the components for future use, a laser cavity length was reduced to 3.8 meters but no more.

Results Two lasers of differing length, one 8.9 meters and one 3.8 meters, were built and their microwave spectra compared. The results were plotted on a linear power scale by first recording the DC power measured by the MSA and normalizing the measured points.

The results are somewhat unexpected. Distinguished by long or short cavity and wide or narrow bandwidth, we found that the best performing laser was one of short cavity and wide bandwidth as shown in Figure 2-25c. The opposite conditions shown in Figure 2-25b show the worst performance. At the least, the results confirm that the microwave noise is due to the cavity length which is shown by the changed spacing from short to long cavity, and it is possible to conclude that reducing the cavity length will in general show some improvement in the noise.
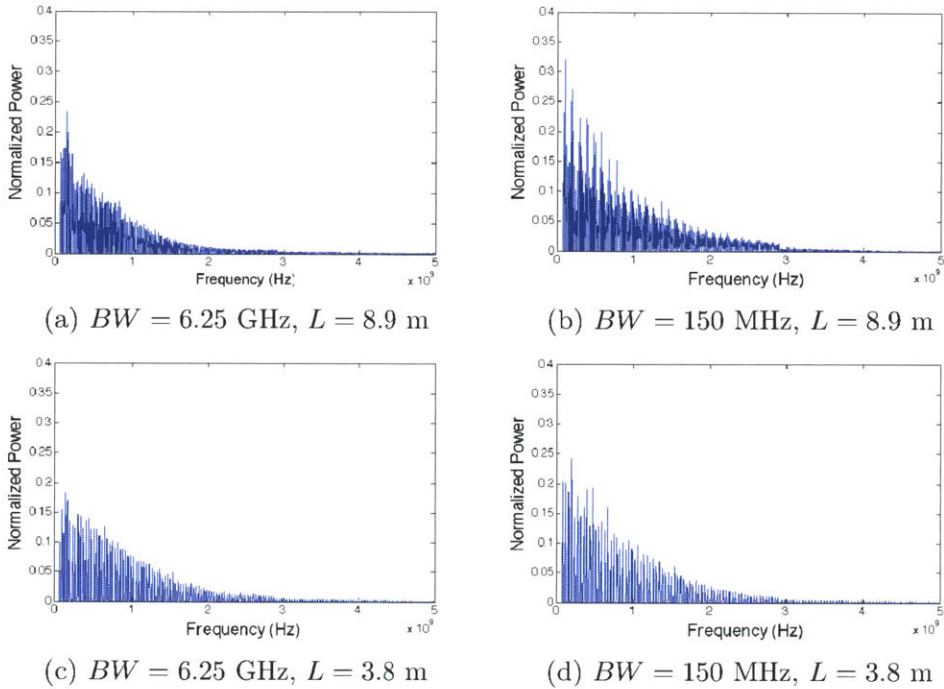
55

(a) $BW = 6.25$ GHz, $L = 8.9$ m   (b) $BW = 150$ MHz, $L = 8.9$ m

(c) $BW = 6.25$ GHz, $L = 3.8$ m   (d) $BW = 150$ MHz, $L = 3.8$ m

Figure 2-25: Normalied microwave spectra of the laser operating with different filter bandwidths and cavity lengths. We find that the laser with large bandwidth and shorter cavity exhibits the least amount of sideband noise.

However, the narrow bandwidth filter shows noticeably worse performance than the wide bandwidth filter negating our hypothesis that dramatically reducing the number of modes would reduce mode competition and encourage single mode lasing under a single filter peak. More unexpected, however, is the spectra shape. One would expect the narrow bandwidth spectrum to fall away sooner as a Lorentzian, but the bandwidth of the spectra regardless of filter bandwidth seem essentially the same.

2.7 Conclusion

In this chapter, we have developed a zero-order model predicting laser characteristics. By individually analyzing the transmission of the components of the ring laser, we were able make predictions about the threshold current and differential and wall-plug efficiencies.

In experiment, we have demonstrated not only multiwavelength but also a single wavelength laser, and it was in this operation where much of our measurements took place. It was found that the mode of operation between single and multiwavelength can be chosen through adjustment of the polarization via twisting the fibers. We find that polarization plays a larger role than anticipated. Comparison of the threshold current and efficiencies showed some discrepancy, but the major issue is the inability to predict the exact output due to the apparent wavelength dependent effects of polarization.

Furthermore, observation of the microwave spectra shows multiple modes underneath the comb filter resonances when the laser is in multiwavelength operation. We saw that the overall beat noise is greather when we filter out a single wavelength in the multiwavelength spectrum and observe it independently than if we observed the entire multiwavelength microwave spectrum. More interesting, however, is that the microwave spectrum when the laser is in single wavelength operation shows none of the multimodal beat noise implying that the laser is truly single frequency.

From the results of the experiments, optimization of the laser was performed by reducing the coupling ratio and internal losses, and we were able to improve the laser WPE 700% with final values of 4.9% WPE with a maximum output power of 4.5 mW. Experiments attempting to improve the microwave spectra noise lead to shortening of the cavity and reducing the filter bandwidth. Though the results were enlightening, they were not expected as we would have guessed the narrower filter reduces the noise and falls off more quickly than the wider bandwidth. What we instead saw was that the narrow filter increases noise and falls off at the same rate as the wider filter. However, we were able to confirm that reducing the cavity length directly reduces the density of modes under the filte peak thus leading to less noise.

Chapter 3

Ring Laser with Integrated Photonic Filters

Chapter 2 discussed the basic setup of a ring laser cavity and an optimization model for improving the performance of the laser. We now incorporate an integrated micro-ring resonator as the wavelength selective filter in our cavity. This requires coupling into a photonic chip using lensed or cleaved fibers. The light propagates a distance in free space and couples into the chip by means of grating couplers. The remaining components of the laser are external to the photonic chip. In this chapter, we detail the coupling method into the photonic device. Then, iterations of the ring laser using an integrated micro-ring resonator as the filter component are described, and the results are discussed. Finally, the performance of succesfully lasing setup based on tunability and communications capability is evaluated.

3.1 Fiber Coupling into Photonic Chips

As mentioned above, coupling into a device on a chip requires different techniques and experimental apparatus than those used in the previous set of experiments. This section will first briefly discuss how the light is coupled into a device on a chip. It will then describe the fiber probe station setup.
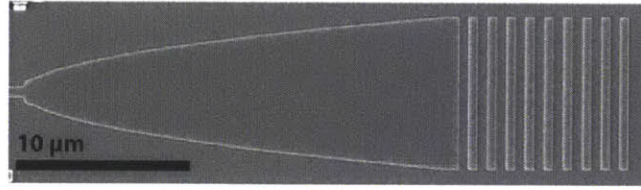
59

3.1.1 Grating Couplers

Figure 3-1: Micrograph of vertical grating coupler by Jason Orcutt [1].

Among the challenges in photonic integration is coupling light into the device. In all integrated devices used in this thesis, the light is coupled through vertical grating couplers from above the chip via fibers rather than being butt coupled. Shown in Figure 3-1 is a micrograph of a vertical grating coupler taken by Jason Orcutt. The coupler tapers to reduce the input or increase the output spot size. A periodic grating scatters the light vertically from the chip.
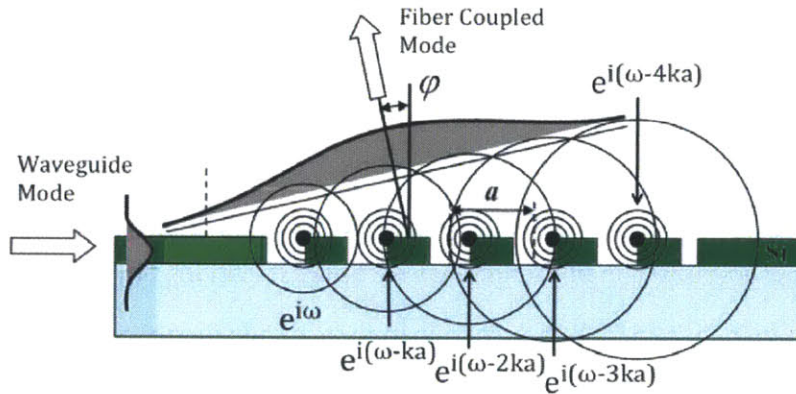

Figure 3-2: Illustration of Hugyens principle as a wave propagates from a waveguide to a grating [1].

Vertical grating couplers at their simplest can be understood using Huygens' Principle. Considering etched teeth placed periodically. This is the grating. As the light propagates toward the grating, each tooth marks a scattering point from which spherical wavelets emanate. At the appropriate grating spacing at a certain wavelength, the wavelets will constructively interfere, and the wavefront moves outward as illustrated in Figure 3-2.
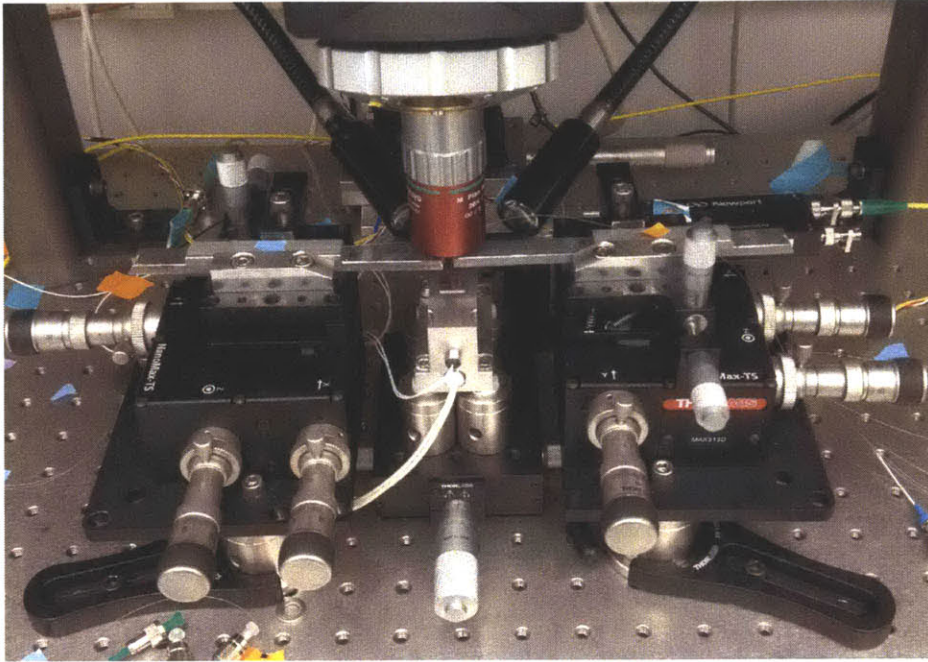
3.1.2 Fiber Probe Station

Figure 3-3: Photograph of fiber probe station.

The fiber probe station is a setup built for testing optical devices on the photonic chips. The chip is held on a heated aluminum vacuum chuck mounted to a 3-axis translation stage. The fibers are mounted on to machined aluminum fiber holders of fixed angles. There are 3-axis translation micrometer stages on either side of the vacuum chuck. 2-axis rotation micrometer stages are mounted to the translation stages to control the angle of the fiber. The fibers are mounted to these stages on either side to control fiber positioning and angle. A microscope with 20× objective lens and and infrared camera are used to observe light input and output as well as fiber position over the chip. The entire setup is held on a floating optical breadboard to minimize mechanical vibration.

3.2 Laser with Tunable 1280 nm Ring Filters

The next set of experiments use micro-ring resonators found in EOS18 device chips meant to operate in the 1280 nm wavelength range. Designed by Mark Wade, the

rings have been selected for having low loss and tuning capacity; thus, we aimed to demonstrate wavelength tuning of the laser as well.
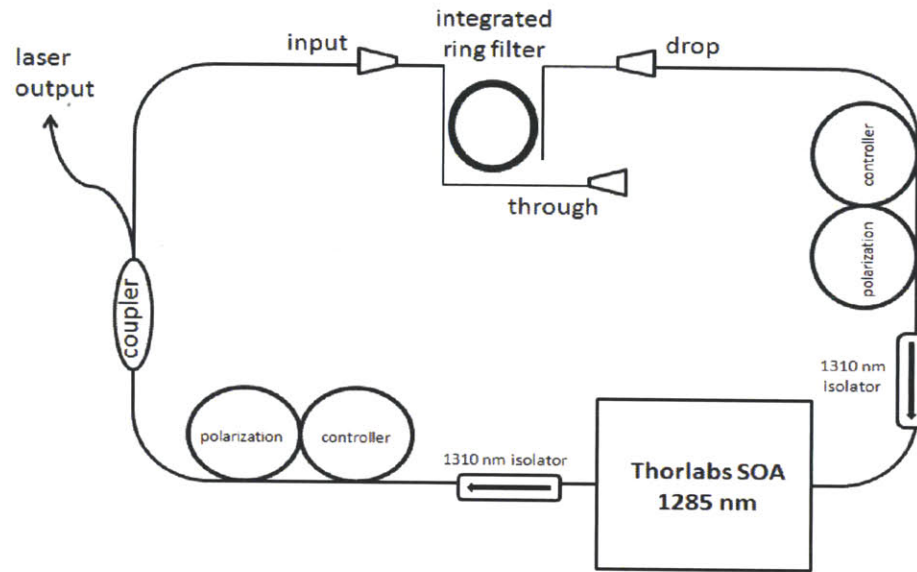
3.2.1 Modified Laser Setup

Figure 3-4: Diagram showing the laser setup for the integrated ring filter experiments. The total fiber length without coupling fibers is 8.8 meters. The coupling fibers add approximately 2 meters.

The laser is shown in Figure 3-4. Having learned from the earlier experiments, an isolator is placed at both the input and output of the SOA to eliminate backwards propagating waves. In addition, the both sets of isolator fibers are threaded through polarization controllers to increase the tuning flexibility and wavelength selection for optimizing the laser performance. The isolators and coupler are both Thorlabs devices designed for operation at 1310 nm wavelength.

3.2.2 Laser Component Characterization

Tunable Micro-Ring Resonator For this laser iteration, the micro-ring resonators chosen are from EOS18 generation device chip. Four-ring filter banks like those shown in Figure 3-5 were designed with 1280 nm grating couplers. The filter
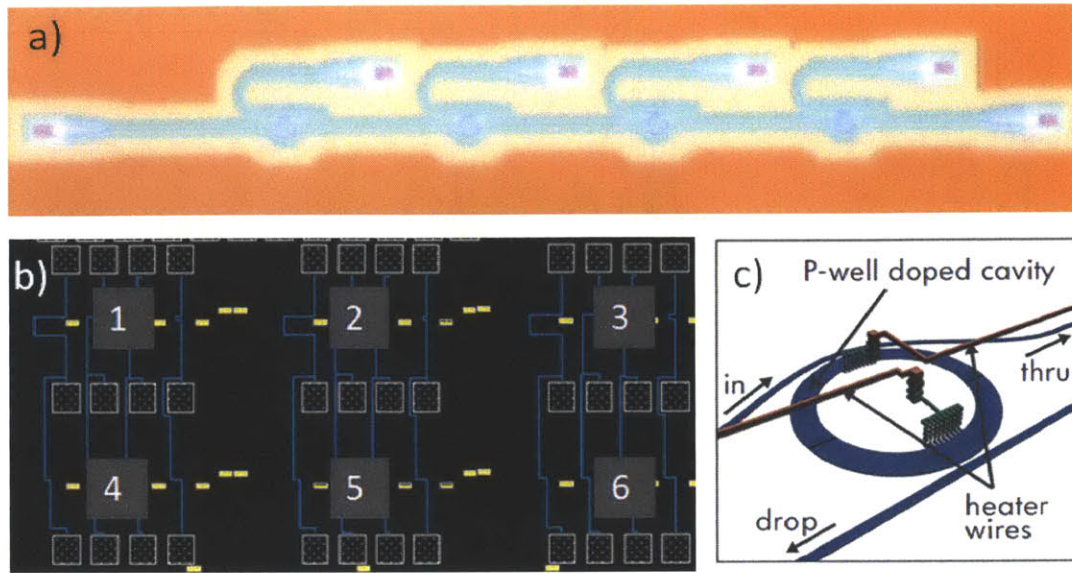
Figure 3-5: EOS18 device chip ring resonator details. a)Photograph through back of EOS18 device chip of a 4-channel filter bank. The vertical grating couplers are designed for 1280 nm wavelength range. Design dimensions: unknown. b) Design environment screenshot showing arrangement of heating pad contacts around six filter banks (numbered 1-6). Filter banks 1-3 are designed for a channel spacing of 400 GHz while 4-6 have a channel spacing of 200 GHz. c) Illustration of heating system of ring. The silicon ring is doped directly making it the origin of resistive heating [25].

banks are numbered 1-6. We selected filter bank 1 for use for its low reported losses. The first ring resonator in filter bank 1 was measured as having losses as low as 10 dB at a coupling angle of 11° [25].

Furthermore, the ring resonators are tunable using electrical heaters. The silicon of the ring resonators in filter bank 1 were p-doped increasing the ring conductivity but having little effect on optical performance. As shown in Figure 3-5, the rings are heated by applying a DC voltage to the contact pads. The measured resistance of ring 1 in filter bank 1 was approximately 50 kΩ.

The transmission function and tuning of the ring resonator is shown in Figure 3-6. The results show the filter has a 3dB bandwidth of 75 GHz or 0.423 nm. The lowest fiber-to-fiber coupling losses at resonance achieved with the aforementioned setup was measured as 15 dB with an FSR of about 18.9 nm. The tuning performance is also shown with up to 2 mW of electrical power applied to the contacts. The tuning curve
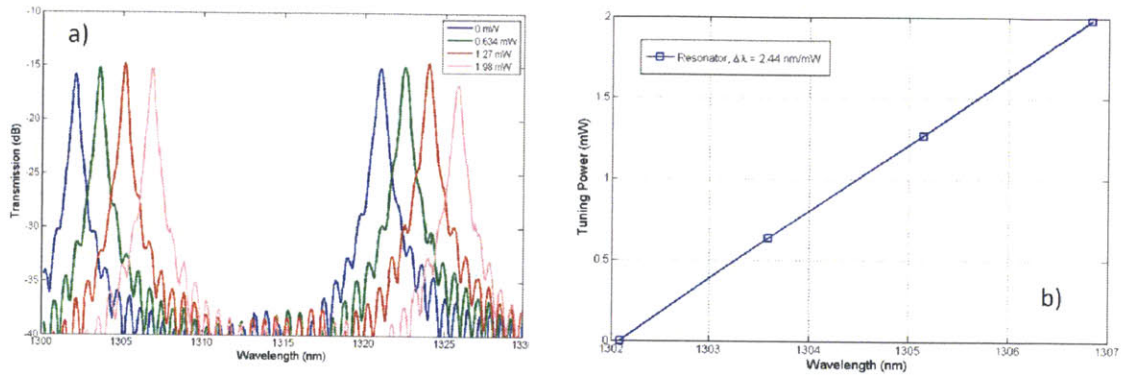
Figure 3-6: Performance of tunable micro-ring resonators. a) Transmission function of micro-ring resonator for tuning powers of 0 mW, 0.643 mW, 1.27 mW, 1.98 mW corresponding to tuning voltages of 0V, 6V, 9V, and 12V. b) Tuning is a linear function of applied power. The wavelength shift is measured as 2.44 nm/mW

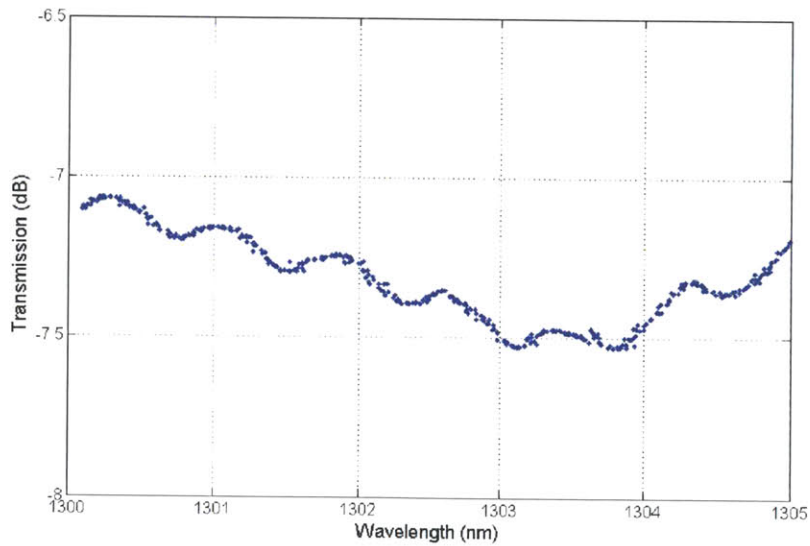is linear with a wavelength shift of 2.44 nm/mW.

Figure 3-7: Transmission through external loss components: two 1310 nm isolators and 1310 nm 50:50 coupler from 1300 nm to 1305 nm. The maximum loss measured in this wavelength range was 7.5 dB.

External Losses In addition to the fiber-to-fiber coupling losses of the ring resonator, the losses contributed by the two isolators and coupler were measured. Figure 3-7 shows the transmission through two Thorlabs 1310 isolators and 1 Thorlabs

64

50:50 coupler for the wavelengths from 1300 and 1305 nm. The components showed losses between 7-7.5 dB in this range. Refer to Section 2.1.4 for details on losses of the individual components.
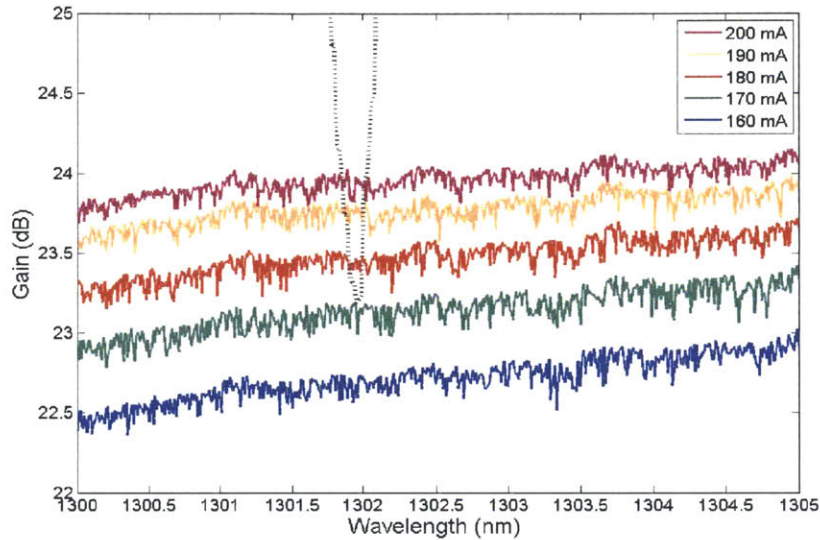

Figure 3-8: The laser setup for the integrated ring filter experiments included two isolators at the input and output of the SOA. The isolator fibers were threaded through a polarization controller to obtain more .

Thorlabs 1130S SOA A Thorlabs 1285 nm center wavelength SOA was used with a maximum small signal gain of 30 dB and saturated gain of 16 dB at a maximum operating current of 700 mA. Figure 3-8 shows the SOA gain over a 5 nm range for relevant bias currents. The threshold current is predicted here to be about 170 mA. However, as was the case in the Micron Filter experiments, the gain curve shows variability as a function of the input polarization. At a bias current of 180mA and wavelength 1300 nm, the gain was measured to have a range as high as 8dB.

Threshold Current and Wall-plug Efficiency The dotted line in Figure 3-8 shows the loss through the total cavity including ring filter, isolators, and coupler. The intersection of the minimum and a gain curve predicts the threshold current. Based on the range of the polarization dependence, we expect the prediction not to
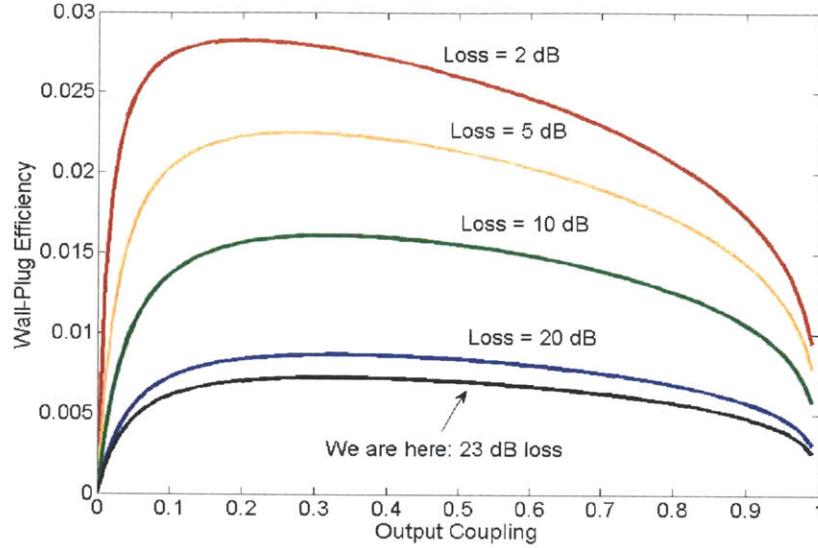
Figure 3-9: Plot showing calculated wall-plug efficiency for an output power of 1mW as a function of coupling output for different internal loss values. Minimizing internal loss in addition to utilizing greater output power will improve efficiency.

be exact but rather an estimate for an arbitrary polarization setting.

The wall-plug efficiency was also calculated using the fitted gain model from Section 2.4. Figure 3-9 shows the wall-plug efficiency plotted for a laser output of 1 mW for a range of internal losses. As seen in Section 2.4, higher output powers will lead to higher efficiencies. In general, 1 mW of output power using this particular SOA will lead to low wall-plug efficiency. In addition, our high internal losses lead us to expect to even lower values of less than 1%. As mentioned in previous arguments, improved laser performance is expected with lowered internal losses as well as utilization of higher output powers.

3.2.3 Laser Performance

LI Curves The LI curves and differential efficiency of the laser are shown in this figure for two different output couplings of 50:50 and 90:10. The data shows predictably that the high coupling ratio has a lower threshold current due to reduced losses in the cavity, but a lower differential efficiency due to lower output photon
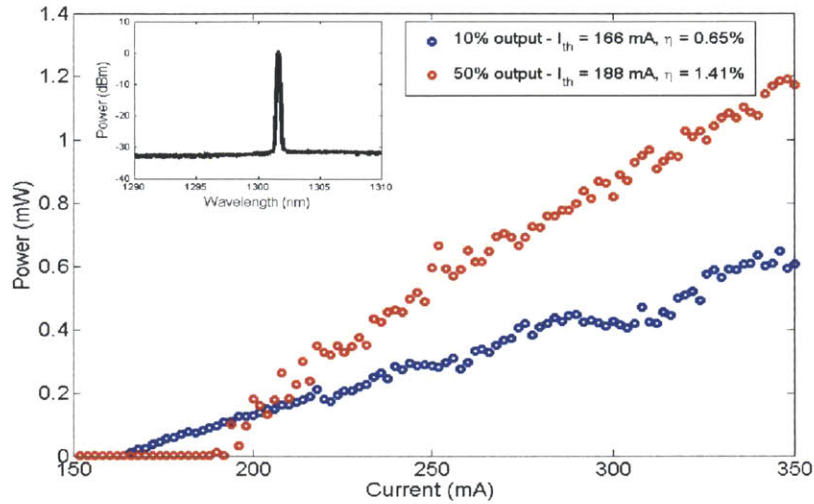
66

Figure 3-10: Plots of LI curves of the integrated 1280 nm laser under two coupling conditions. The high coupling ratio leads to a low threshold current due to lower internal losses but lower efficiency to do low output photon rate. The inset shows the laser spectrum at 350 mA bias current at a resolution bandwidth of 0.1 nm

coupling. At a bias current of 350 mA, an output power of 1.2 mW was achieved; however, the maximum output power is highly dependent on optimal polarization alignment. It is possible to do better by having full tuning control of the polarization. For an output power of 1 mW, the wall-plug efficiency is calculated as 0.42% for 50% output coupling and as 0.34% for 10% output coupling. The results are comparable to predicted values from Section 3.2.2.

The LI curve data shows some instability in the output power. The OSA spectra also showed instability in wavelength. To examine this instability, the wavelength as a function of the laser power was plotted, as shown in Figure 3-11. The curve indicates that the wavelength is not hopping for arbitrary powers as the current is stepped.

The experiment is repeated with the 50:50 coupler but pushed to the maximum SOA current of 600 mA. Based on Figure 3-12, the laser becomes less stable at higher currents but continues to increase in power in an approximately linear curve showing no signs of roll-off. The power at 600 mA projected by the fitted line is 6.34 mW, but the highest recorded power is 6.72 mW. The differential efficiency of 1.46% is close to
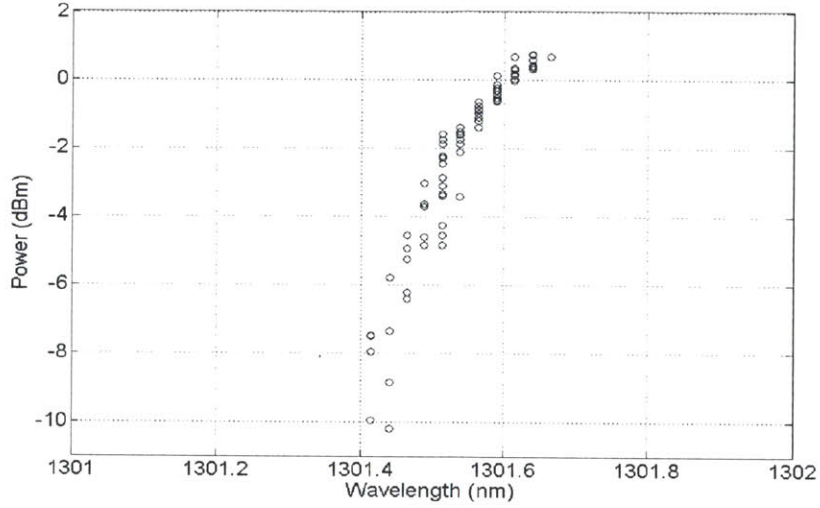
Figure 3-11: Plot showing relationship between output power and wavelength shift. The total wavelength shift from threshold to 1.2 mW output power is 0.2 nm. The results indicate that wavelength shifts on the order of 0.1 nm are correlated to laser output power and also therefore the heating of the ring.
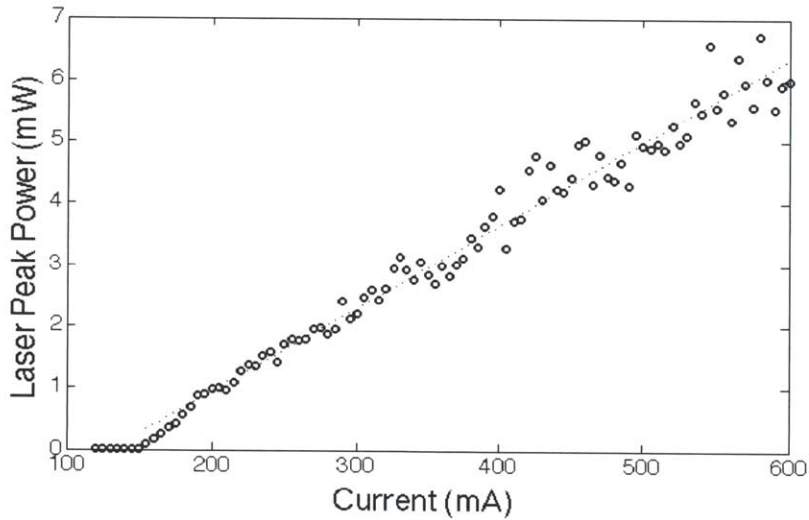

Figure 3-12: Plotted LI Curve of integrated 1280 nm laser taken to maximum SOA current of 600 mA. The laser performance becomes noticeably less stable at higher currents. The differential efficiency is measured as 1.46%.

the original experiment. The threshold current occurs at 155 mA. This corresponds to a wall-plug efficiency of 1.10% for our maximum output power. For an output power of 1 mW, the WPE is closer to 0.46% matching up to the predictions of Figure 3-9.
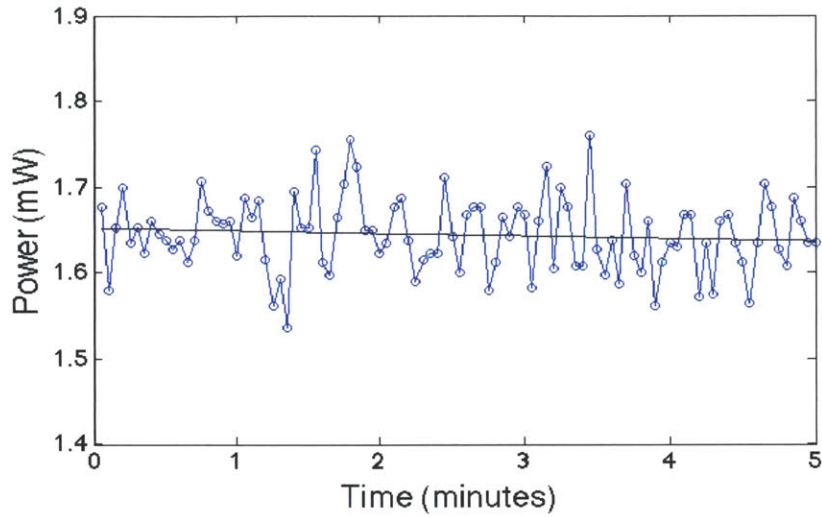
68

Figure 3-13: Plot of integrated 1280 nm laser stability showing the laser peak power as a function of time for up to 5 minutes at a bias current of 300 mA with range of fluctuation 0.223 mW.
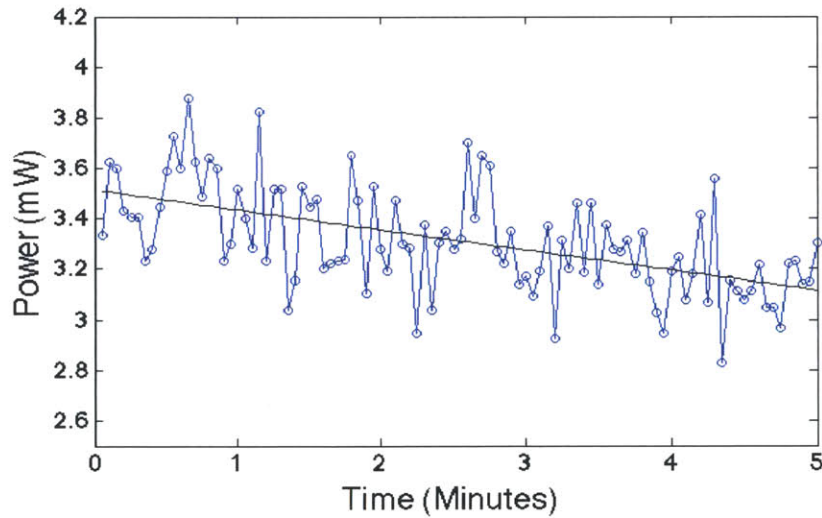

Figure 3-14: Plot of integrated 1280 nm laser stability showing the laser peak power as a function of time for up to 5 minutes at a bias current of 400 mA with largest power jump being 0.73 mW. In addition to power instability on shorter time scales of seconds, the plot shows an overall trend of decreasing laser power at the rate -0.078 mW/min.

The stability was evaluated by taking 100 spectra at a current bias of 300 mA over the course of 5 minutes. The time is approximate as it accounts for the waiting time

69

between scans but not the additional machine cycles for the instrument commands which are assumed negligible. Figure 3-13 shows the peak power of the laser as a function of time. The laser fluctuates over a range of 0.223 mW and shows slight decline.

The experiment is performed again at higher current bias of 400 mA, and the results are shown in Figure 3-14. Not only has the range of fluctuation greatly increased with the largest power change in consecutive scans being 0.73 mW, but the stability plot shows an obvious trend of decreasing average power at a rate of -0.078 mW/min.
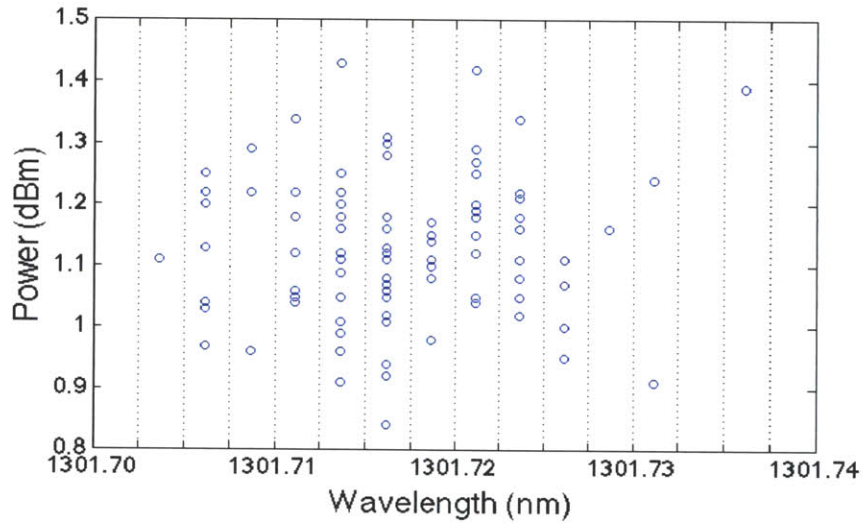

Figure 3-15: Plot of integrated 1280 nm laser wavelength as a function of power. The columns are each 0.0025 nm width which is the MATLAB data resolution.

Plotting the wavelength as a function of power for the bias current of 300 mA also shows that the laser peak wavelength is most unstable. Figure 3-15 shows that the lasing mode is not dependent on power and moves within a 0.04 nm or 7 GHz range. The points are determined to be spaced 0.0025 nm apart. However, this is the resolution of the MATLAB data. It is likely that more of a spread would appear at better resolutions. One can make the conclusion that the peak wavelength is constantly hopping. To support this, Figure 3-16 shows the measured peak wavelength as a function of time. The source of the constant peak shifting could be instabilities

70
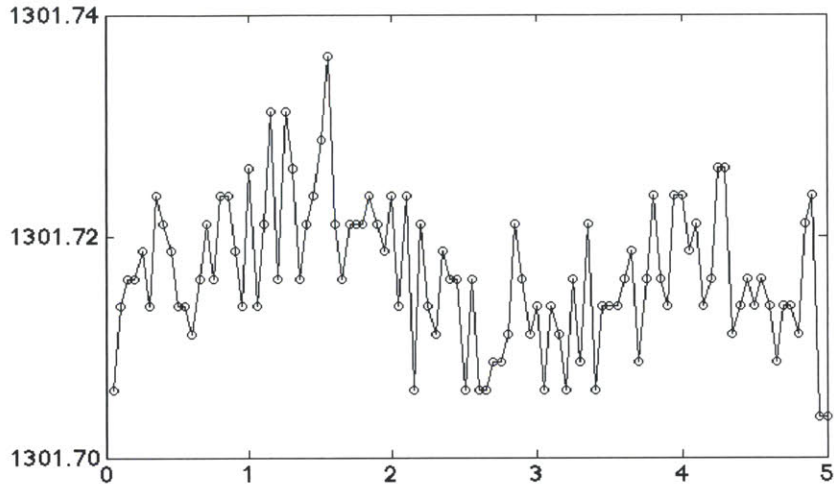
Figure 3-16: Plot of integrated 1280 nm laser wavelength as a function of time.

in the fiber coupling. The fiber is floating over the chip and mechanical vibrations may disrupt stable laser operation.

Figure 3-17: Optical heterodyne experiment with the laser modulated at 1 GHz to compare cavity mode strength to the modulation frequency beat. The MSA resolution bandwidth is 511 KHz.

Optical Heterodyning As a result of the power instability, the microwave spectrum of the laser was also measured to look for beating cavity modes. Optical

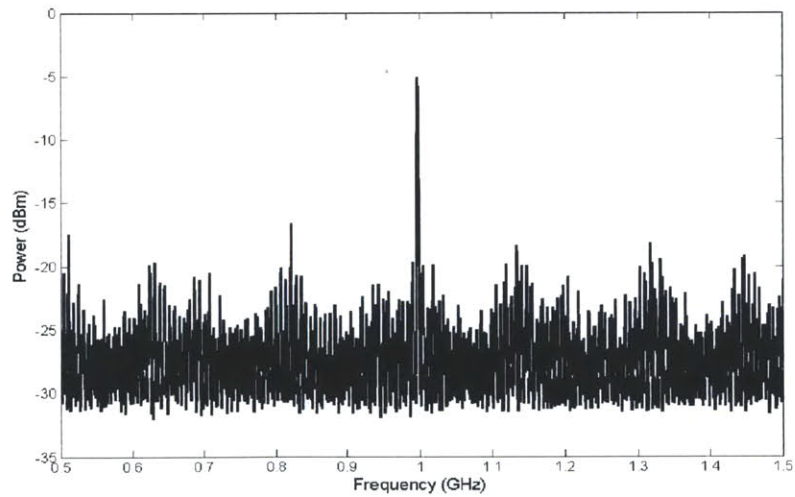heterodyne experiments using the Microwave Spectrum Analyzer show that the laser has decent suppression of beat noise. The Figure 3-18 shows the microwave spectrum of the laser output modulated at 1 GHz. The microwave spectrum of the direct laser
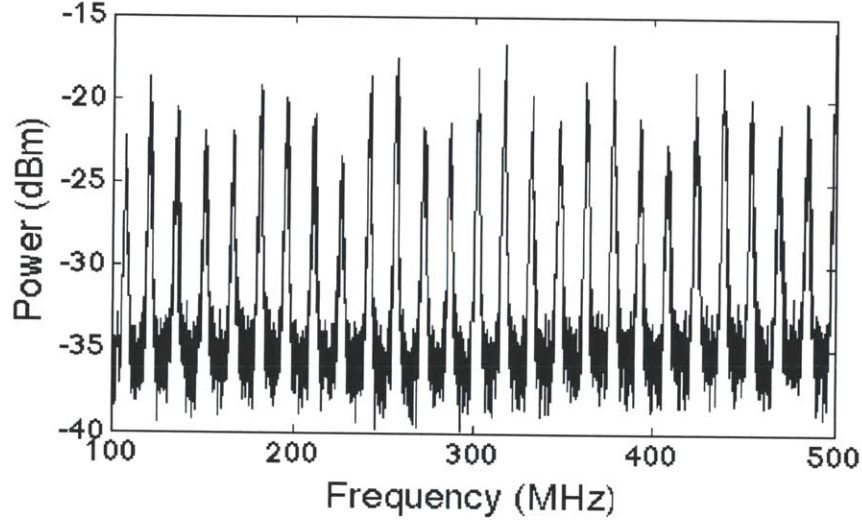

Figure 3-18: Optical heterodyne experiment with direct laser input at showing microwave spectrum from 100 to 500 MHz. The approximate mode spacing is 15 MHz.

output without modulation shows that the beat notes are spaced 15 MHz apart.

We can also estimate a value for the the Relative Intensity Noise (RIN) of the laser. The RIN is given as

$$\text{RIN} \equiv \frac{\langle \Delta P(t)^2 \rangle}{P_0^2} \tag{3.1}$$

where $\langle \Delta P(t)^2 \rangle$ is the mean-square optical intensity noise and P_0^2 is the average optical power squared. We show the microwave spectra for measuring the optical intensity of the frequency noise with and without the laser input. Near 2 GHz, we find that the averaged optical intensity noise looks to be about -20 dBm. We can rewrite Equation 3.1 in terms of dBm units.

$$2\Delta P(t)_{dBm/Hz} - 2P_{0,dBm} \tag{3.2}$$

To find a value for the RIN, we first convert optical intensity from dBm to mW, and divide by the resolution bandwidth which is 511 kHz. We convert this value back to
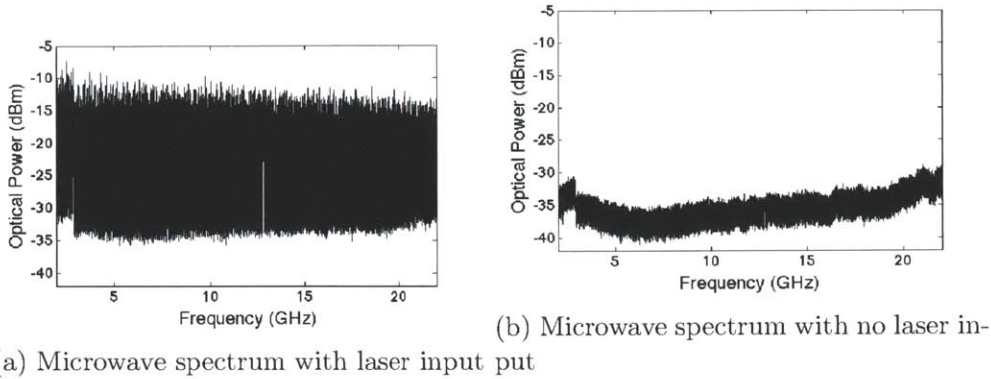
72

(a) Microwave spectrum with laser input put

(b) Microwave spectrum with no laser in-

Figure 3-19: Microwave spectra displayed by MSA with and without laser input over 2-22 GHz range. The laser input power was 9.4 μW for a resolution bandwidth of 511 kHz.

logarithmic scale abd then subtract two times the average optical power measured in dBm. From this, we find that the RIN estimate is about -113 dB/Hz keeping in mind that a DFB laser has a typical RIN around -150 dB/Hz. We find this consistent with our observations of the laser as a noisy source, but also comment that the laser is not far from the performance of a typical Fabry-Perot laser which has a RIN near -120 dB/Hz.

3.3 Laser Tuning and Wavelength Modulation

To tune the laser, DC probe needles were mounted and positioned around the chip at the top and bottom of the vacuum chuck to touch the heater contacts. The laser was tuned by applying a DC voltage across the contacts. The results of tuning the laser are shown in Figure 3-20 for four tuning powers. The resonator peak transmission at the same tuning is also shown in dotted lines in the figure. It is apparent that the tuning curves have slightly different slope and slight offset. This is a result of the laser power generating additional heating in the doped silicon ring and creating a larger wavelength shift than anticipated from the resonator tuning results.

The tuning curve shown in Figure 3-21 shows a slight increase in tuning efficiency by 3.7% for the laser over the resonator tuning. The linear behavior is disturbed

73
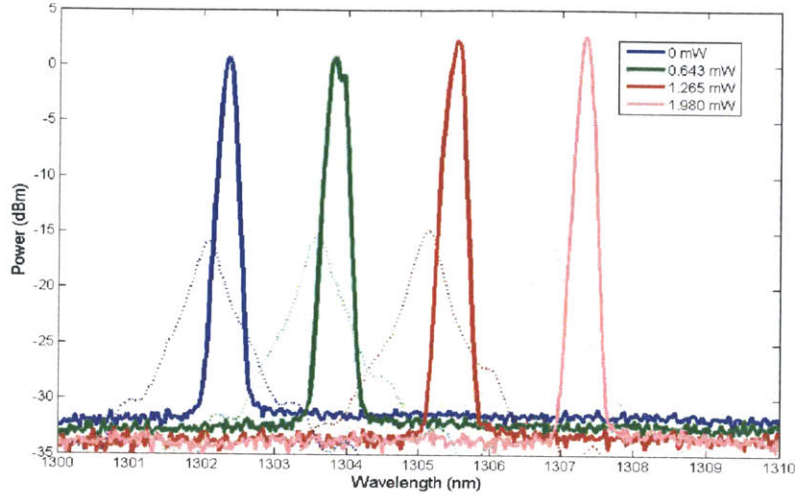
Figure 3-20: Optical spectra showing wavelength shift of laser as different tuning powers are applied. The resonator transmission at the respective tuning powers is also plotted. Misalignment of the laser spectra and resonator transmission are attributed to the laser power contributing to additional heating of the ring resonator.
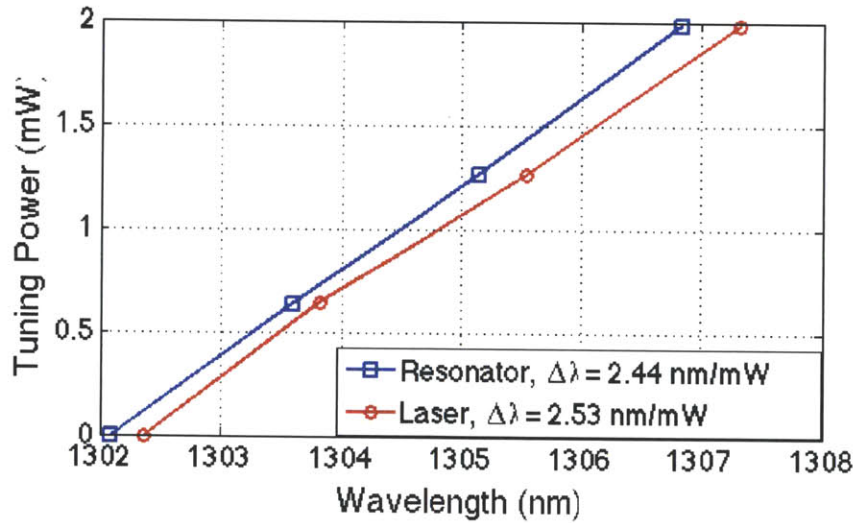
Figure 3-21: Tuning curves for the laser in red and ring resonator in blue. The laser shows an increase in tuning efficiency due to self-heating. The laser tunes 2.53 nm/mW. The ring resonator tuned 2.44 nm/mW.

slightly by the second data point in the laser tuning curve corresponding to a tuning power of 0.643 mW. The laser output at this point shown in Figure 3-20 is the green curve, and a cleft peak is noticeable in this output. The double-peaked behavior

74

suggested the possibility of at least a second simulataneously lasing mode that was not visible under the OSA resolution bandwidth.
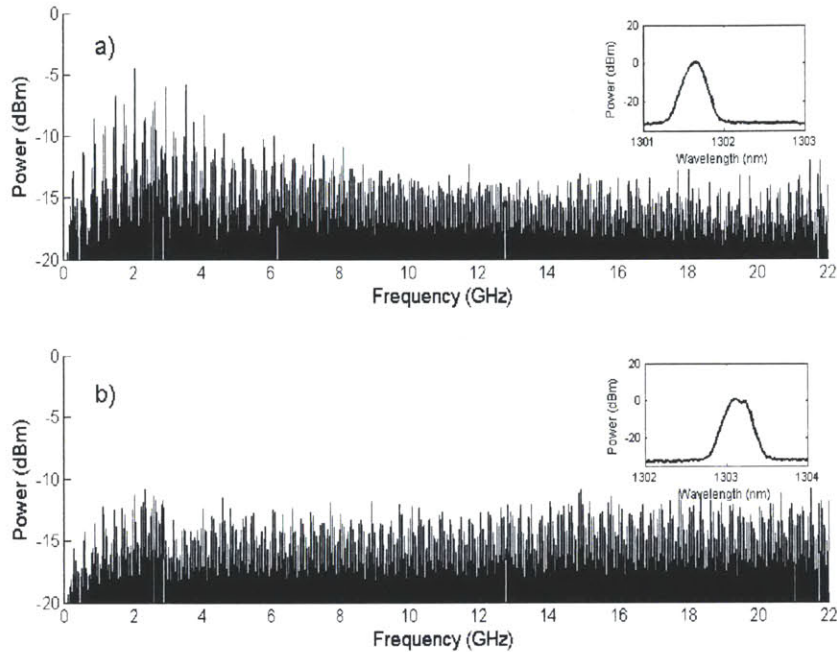

Figure 3-22: Microwave spectra comparing the laser RF noise at two tuning voltages. a) Spectrum showing the laser at 0V tuning. The inset is the optical spectrum show a single-peaked laser. b) Spectrum showing the laser at 6V tuning. The inset again is the optical spectrum, but showing the double-peaked curve. The results of these measurements does not show a second mode responsible for the cleft curve in the 22 GHz range.

The microwave spectra of the laser output at 0 mW tuning and the output at 0.634 mW tuning were measured and compared in order to determine the presence of a second mode within the filter bandwidth. Figure 3-22 shows the full 22 GHz range of the MSA spectra for the laser at the two tuning powers. The results show the usual cavity noise but no indication of a second lasing mode. It is possible that since the ring resonator bandwidth is 75 GHz, the MSA bandwidth is not large enough to see the second mode. Alternatively, the cleft shape of the laser may be due to mode hopping over larger spaces than shown in Figure 3-15, and the video averaging of the OSA which is on the order of a millisecond shows two peaks rather than a shifting

peak. The results show that in spite of the shape, the noise of the tuned laser output is no worse, but actually better, than the untuned laser output with a single peak.
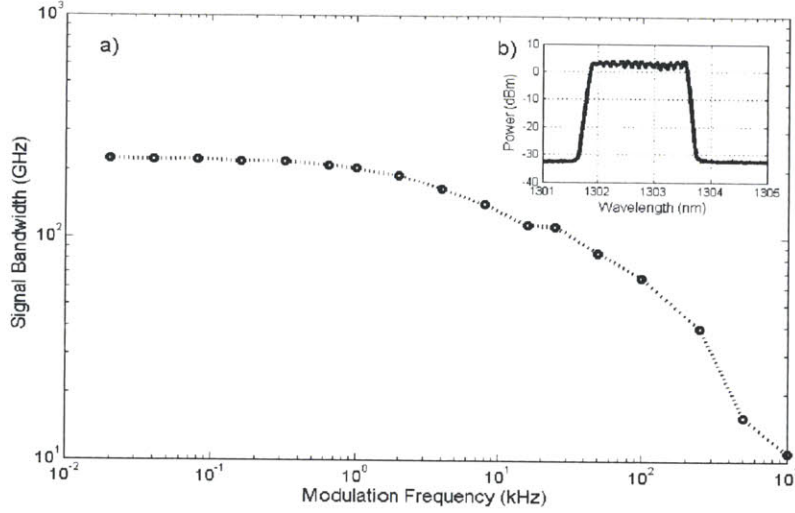

Figure 3-23: Logarithmic plot showing wavelength sweep range as a function of modulation frequency for a tuning voltage of $4V_{pp}$. Rolloff occurs near 1 KHz. The behavior is most likely the result of high frequency limits of the DC probe.

Because the laser tuning required applying power to the ring directly, it became interesting to investigate wavelength modulation of the laser. A sine wave voltage of $4V_{pp}$ with 2VDC offset was applied to the contacts through the DC probes. The spectra was measured using the OSA at a much slower scan time of 15 seconds as opposed to the default 1 ms. Figure 3-23 shows the wavelength sweep range of the laser versus the modulation frequency.

The plotted curve seems to show rolloff near 1 KHz. The likely cause of this rolloff is the use of DC probes for applying higher frequency AC voltage and about 1 meter of cable from the voltage source. The measurement should be performed again with microwave RF probes to apply high frequency voltages. However, the test structures and heater contacts on EOS18 are positioned in such a way that the fibers would interfere with probing the contacts, see Figure 3-5. As a result, future layouts with similar ring resonator structures should consider contact placement for AC probing.

The tuning voltage range was tested for signs of rolloff at high voltages. The maximum tuning voltage is set to 20V due to the appearance of sharp peaks on the

(a) Tuning Voltage $= 10V_{pp}$

(b) Tuning Voltage $= 15V_{pp}$
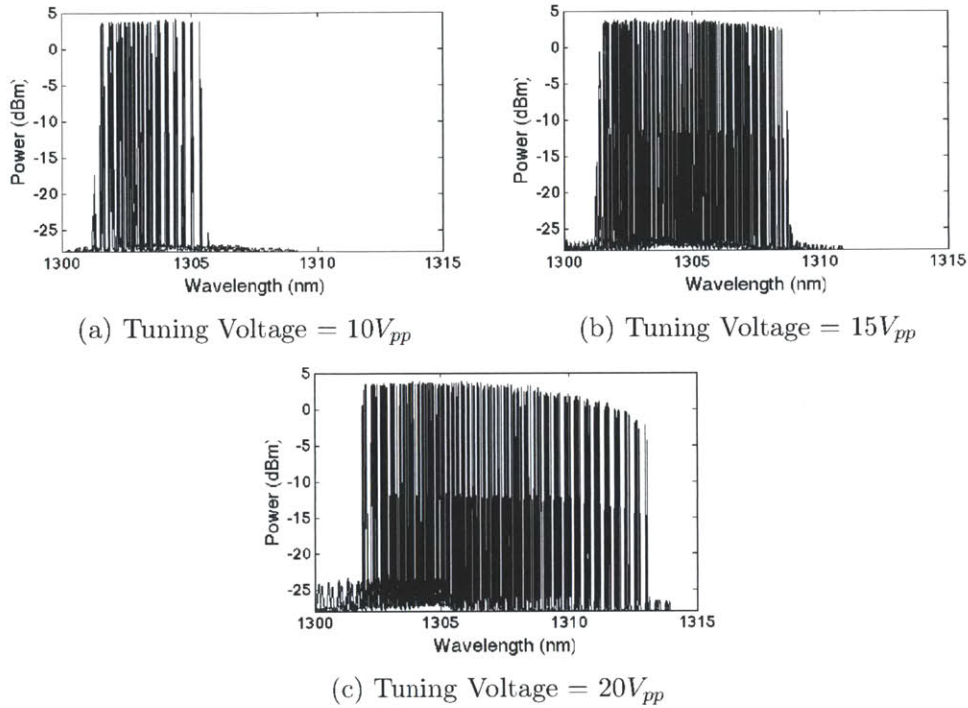

(c) Tuning Voltage $= 20V_{pp}$

Figure 3-24: Optical spectra of the integrated ring laser wavelength modulated at different tuning voltages at a frequency near 1 Hz. The spectra was measured with a slow scan time of 30 seconds.

noise floor in the optical spectrum and concern for the MRR integrity. Figure 3-24 show the optical spectra for tuning voltages of $10V_{pp}$, $15V_{pp}$, $20V_{pp}$. The high voltage waveform source is a Agilent 4156B Semiconductor Parameter Analyzer programmed to produce a triangular output wave. The frequency of the signal is near 2 Hz as to avoid rolloff. The observed spectra over the range of tuning appeared to maintain single frequency lasing.

The resultant tuning ranges gathered from the optical spectra were plotted with respect to the applied power. The applied power required knowledge of either the resistance of the doped resonator or the input current. Results from Figure 3-21 were used to calculate the resistances for the applied tuning voltages. We found the resistance was an linearly increasing function of voltage, and the curve shown in Figure 3-25 was used to extrapolate the ring resistance at the higher voltages, and the tuning voltage was converted to tuning power using $\frac{V^2}{R}$.
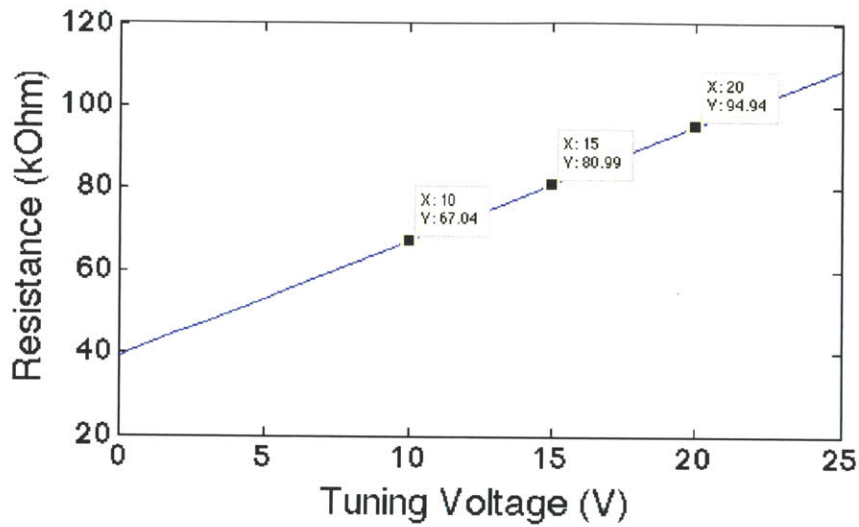
Figure 3-25: Fitted curve of ring applied voltage versus ring resistance. The curve was used to extrapolate values of resistance at the applied voltages of 10, 15, and 20 V_{pp}
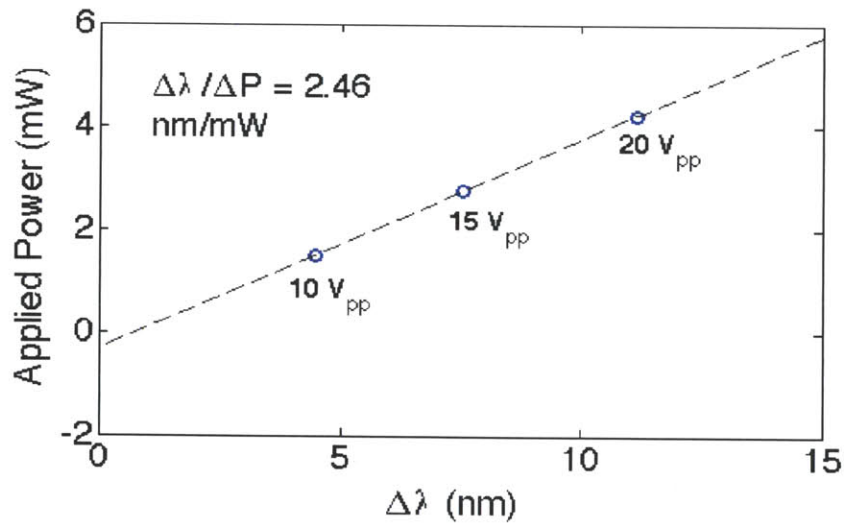
Figure 3-26: Curve showing signal voltage versus width of signal in the optical spectrum for 10, 15, and 20 V_{pp}. The three points were used to create a linear fit an inverse slope 2.46 nm/mW.

Figure 3-26 shows the results of plotting the applied power against the wavelength range. A line was fit to the three points, and a slope of 2.46 nm/mW was calculated. This matches with the tuning slope of the resonator without modulation which leads us to believe that modulation of the ring at a high voltage should not degrade its

tuning performance.

3.4 Laser Performance in Communications Link

Because of the results of the optical heterodyning showed suppression of beat noise and the clear appearance of the modulation signal, we set up a communications experiment evaluating the performance of the laser as a data carrier. The internal
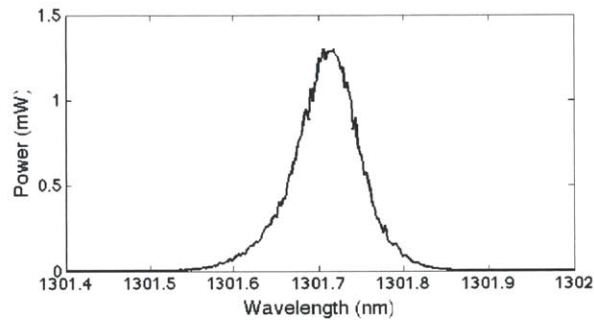
Figure 3-27: Laser spectrum from photonic ring experimental laser. The linewidth is limited by the OSA resolution bandwidth of 0.1 nm.

polarization of the laser cavity was adjusted until the laser appeared to be single mode. The resolution bandwidth of the OSA is 0.1 nm. We show the laser spectrum in Figure 3-27.

3.4.1 Data Line Setup

The output of the laser was modulated using an Avanex 15 GHz modulator. An Agilent 70843B Bit Error Rate Tester (BERT) generates the pseudo-random bit sequence (PRBS) that drives the modulator. The data rate of the PRBS can be adjusted by changing the clock frequency of BERT. The output is measured using a Hewlett-Packard 83480A Digital Communications Analyzer with an optical input module. The communications analyzer is set to color grade the waveform so that for a given period, the waveform is overlapped to generate an eye. Figure 3-28 shows the experimental setup and distinguishes the RF and optical paths. The laser was operated at a bias current of 300 mA which is a laser output power between 2.5-3.0 mW.

Figure 3-28: Illustration of eye diagram measurement setup. The BERT is simplified as a clock and PRBS generator providing the RF trigger and data outputs.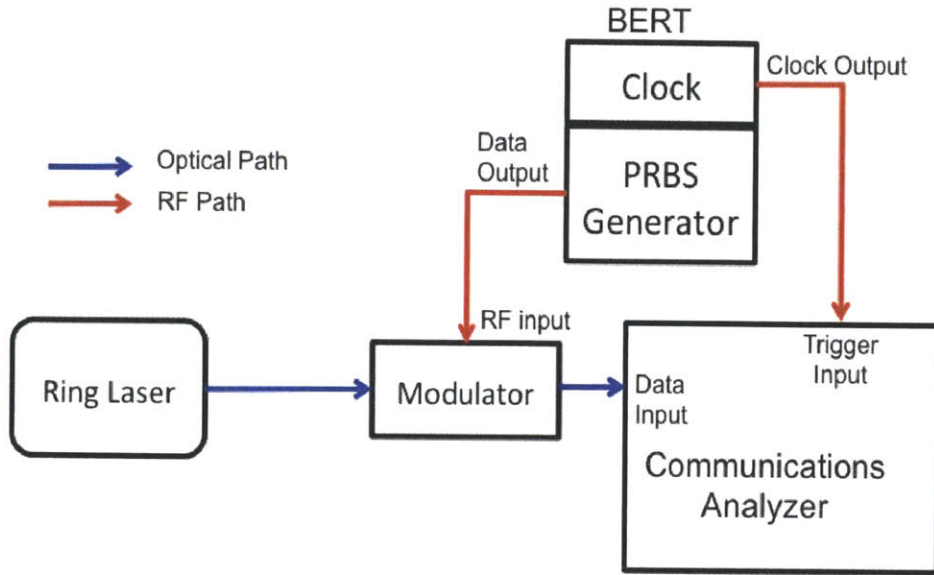 These RF signals go to the Comm. Analyzer and modulator RF input respectively. In the optical path, the laser output is passed through the modulator input and output and viewed on the Comm. Analyzer.

3.4.2 First Round Eye Data Results

The first results of the measurements showed open eye data at a bit rate up to ~5 Gb/s with signal peak-to-peak of 1.2 mW. However, at the lowest data rate of 1 Gb/s, the signal was too noisy to produce an open eye as shown in Figure 3-29a. However, increasing the data rate to 2.5 Gb/s eliminated the noise. Figures 3-29b and 3-29c show results considered successful eyes.

3.4.3 Modified Data Line

Because of the flatter shape of the pulses, the driving power of the BERT is amplified through a 40 Gb/s modulator driver from Picosecond Pulse Labs to see if the shape of the waveform can become sharper and lead to a cleaner eye as a result. Furthermore, a Thorlabs 1310 nm isolator was added before the modulator input in an attempt to reduce the noise at the lower data rate. The modified setup is shown in Figure 3-30. The laser bias current was also increased to 400 mA in order to increase laser output

(a) Data rate of 1 Gbps

(b) Data rate of 2 Gbps
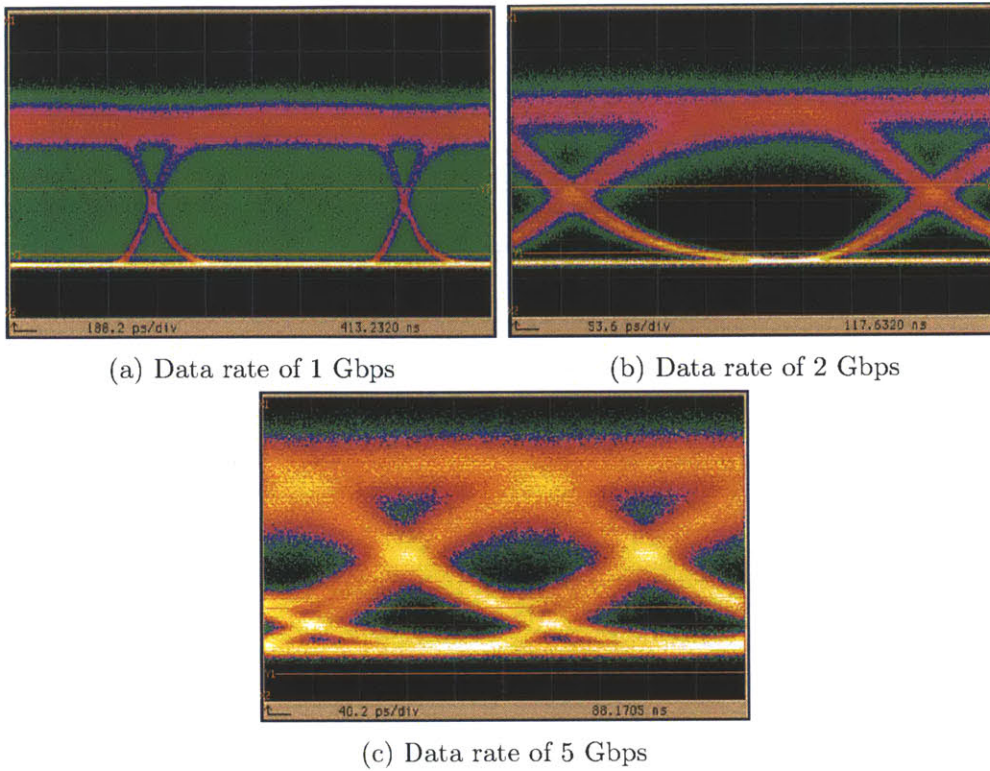

(c) Data rate of 5 Gbps

Figure 3-29: Screenshot of measured eye using Communications Analyzer at a data rate of 1.8 Gbps. The vertical axis measures power at 200uW/div.
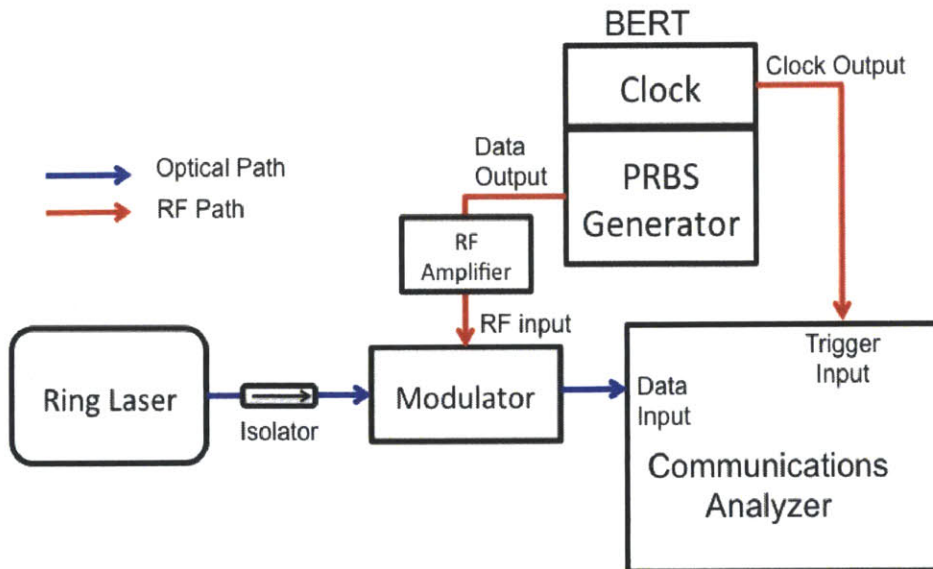

Figure 3-30: Communications experiment with modifications including an isolator before modulation in the optical path and an amplifier in the RF path.

power without observing too much instability on the optical spectrum. This is a laser output power near 3.5-4.0 mW.

3.4.4   Second Round Eye Data Results

(a) Data rate of 1 Gbps   (b) Data rate of 5 Gbps
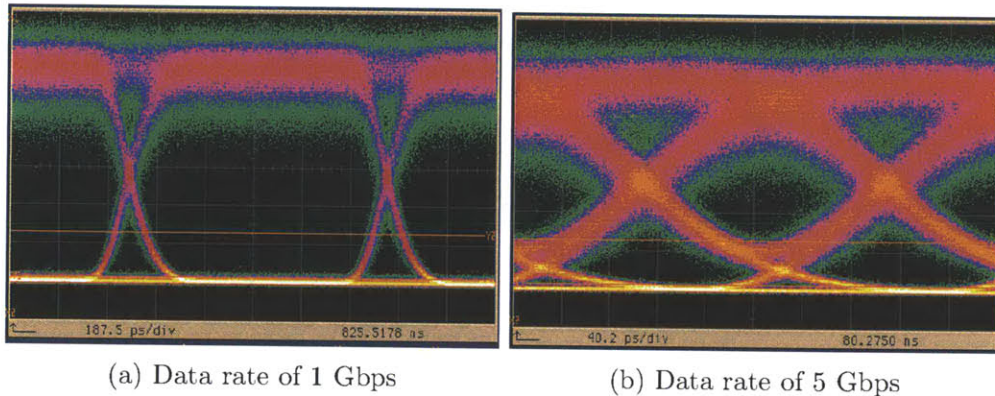
Figure 3-31: Screenshot of measured eye using Communications Analyzer at a data rates of 1 Gbps and 5 Gbps.

The results of the data at 1 Gb/s data rate showed significant noise improvement as the eye was completely clear. Also, due to increased optical power, the signal height improves from 1.2 mW to 1.8 mW peak-to-peak. The measurement is performed at 5 Gb/s. Though the signal peak is higher and the eye more visible, the rise and fall of the edges of the signal is still too slow. This may be ultimately rely on the limits of the PRBS generator. The features of thick band of signals for 'on' state and narrow band at 'off' state is resultant of the laser noise. Certainly, we can expect to improve these results if the laser noise and instablity is also reduced.

Because of the improvements from increased signal strength, eye diagrams were measured at data rates 6 Gb/s and 7 Gb/s. Unfortunately, the results shown in Figures 3-32a and 3-32b show eyes that are barely open in the case of 6 Gb/s or not open at all 7 Gb/s. This experiment still deserves more work, particularly with improving the signal rise and fall times of the PRBS source.

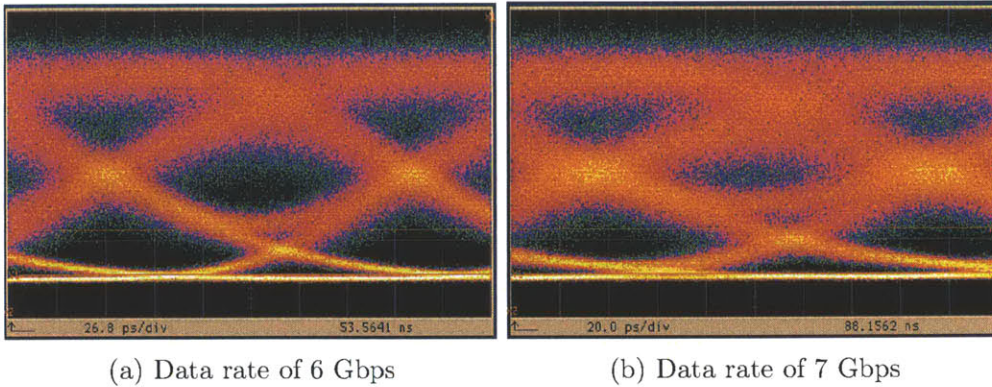|	
(a) Data rate of 6 Gbps	(b) Data rate of 7 Gbps

Figure 3-32: Screenshot of measured eye using Communications Analyzer at a data rates of 6 Gbps and 7 Gbps.

3.5   Conclusions

In this chapter, we have demonstrated a laser using external gain and integrated components with an output power upwards of 6 mW and corresponding wall-plug efficiency of 1.10%. We predict that improving the round trip losses, particularly the integrated resonator and fiber coupling losses, will lead to much better WPE.

Furthermore, we have demonstrated the advantages of using integrated components by successfully tuning the laser wavelength using integrated heating components. Because the resistive losses are built into the ring structures themselves, we were able to show the results of some wavelength modulation experiments but were ultimately limited to low frequency modulation due to inconvenient placement of the probe pads. Though the frequency rolloff remains inconclusive, we were able to modulate the wavelength up to a range of 11.2 nm.

Finally, lower noise from the microwave spectra results indicated the possibility of reading distinguishable bits using the laser. As a result, eye diagrams modulating the laser at increasing data rates were taken. We find that the laser is still much too noisy to achieve a clean eye at 10 Gbps, but an open eye at 5 Gbps has been demonstrated.

Chapter 4

Multiwavelength Ring Laser Theory

From the results of Chapters 2 and 3, it is apparent that the phenomenogical laser theory from Section 1.2 is not sufficient to describe the observed behavior of the fiber ring laser. The system exhibits complicated behavior that is not easily predictable or, at the time of observation, explainable.

In particular, in Chapter 2, we were able to show that the polarization controller could be adjusted so that the laser is either multiwavelength or single wavelength. On that note, we also found that the unknowns about the system polarization made it difficult to make an accurate prediction about the laser characteristics.

Furthermore, results from microwave spectra measurements ran counter to our intuitions. Specifically, though we anticipated the presence of multiple modes, we found two surprising results that seem related: 1) The relative noise decreased when the input into the photodetector was multiwavelength than when it was filtered single wavelength. 2) A narrower filter bandwidth demonstrated higher intensity noise than the wider bandwidth.

This chapter attempts to provide some possible explanations and theory behind the aforementioned observations of the ring laser performance. The first section of this chapter will analyze the effects of polarization and begin with a coverage of Jones Calculus. This foundation will then be applied in simulation to explore

the polarization dependence of the cavity and how it may have significant effects on laser performance. The second section examines the microwave spectra more closely by considering the effect of random phase and calculating predicted spectra for comparison to experimental results.

4.1 Effects of Polarization

The experiments show that the ring laser performance is highly polarization dependent. The fiber used in all of these experiments is not polarization maintaining and components such as the SOA and integrated filter of the ring cavity show very high polarization dependence. In fact, the filter works in conjunction with polarization controllers act together as the wavelength selective elements of the cavity, and each iteration of the laser required significant tweaking of the polarization paddles to maximize output power. As a result, we seek a means of explaining the components together via Jones matrices in an effort to illustrate the wavelength dependence of the cavity polarization.

4.1.1 Jones Matrix Formulation

Modeling Birefringence We start with a simple model for birefringence as developed by Yariv and Yeh in Chapter 5 of *Optical Waves in Crystals* by deriving the Jones matrix for a uniaxial material [26]. Stated simply, a uniaxial material has different indices of refraction along different crystal axes. We assume orthogonal axes which we will call "fast" and "slow" axes with the light propagating in the z-direction. Figure 4-2 illustrates the orientation of the material and laboratory axes. Given our labeling, we express the index of refraction of the fast and slow axes as n_f and n_s respectively. Because of the inevitable phase lag that occurs between the fast and slow axes, this material is called a retardation plate.

We express the Jones vector of an incident propagating wave defined along labo-
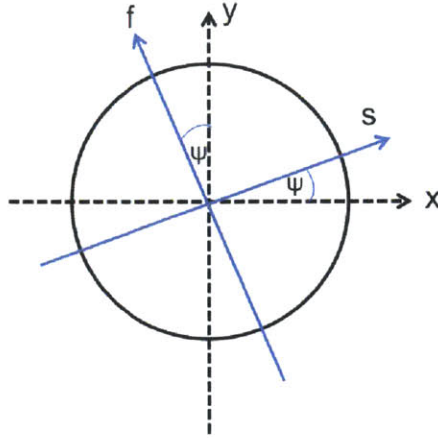
Figure 4-1: Illustration of uniaxial material with orthogonal "fast" and "slow" axes offset at an angle ψ from the laboratory x and y axes.

ratory axes as follows

$$\mathbf{E}_{in} = \begin{pmatrix} E_x \\ E_y \end{pmatrix} \tag{4.1}$$

Using a coordinate transform, the incident wave is redefined along the plate axes which is offset an angle ψ from 0. The orientation is shown in Figure 4-2, and the transformation is expressed as

$$\begin{pmatrix} E_s \\ E_f \end{pmatrix} = R(\psi) \begin{pmatrix} E_x \\ E_y \end{pmatrix} \tag{4.2}$$

where the transformation matrix $R(\psi)$ is

$$R(\psi) = \begin{pmatrix} \cos(\psi) & \sin(\psi) \\ -\cos(\psi) & \cos(\psi) \end{pmatrix} \tag{4.3}$$

Since the incident field has been written in terms of the plate axis, we see that the phases along the fast and slow axis operate independently on the respective vector components. Therfore, the on-axis Jones matrix of a phase retarder, which we will

87

call W_0, is diagonal and written

$$\begin{pmatrix} E'_s \\ E'_f \end{pmatrix} = \begin{pmatrix} e^{-ik_s d} & 0 \\ 0 & e^{-ik_f d} \end{pmatrix} \begin{pmatrix} E_s \\ E_f \end{pmatrix} \tag{4.4}$$

where a wave vector component is expressed as $k = \frac{2\pi n}{\lambda}$.

We wish to rewrite the Equation 4.4 with respect to the total phase difference Γ defined as

$$\Gamma = \frac{2\pi d}{\lambda}(n_s - n_f) \tag{4.5}$$

Furthermore, the mean absolute phase change ϕ is defined as

$$\phi = \frac{\pi d}{\lambda}(n_s + n_f) \tag{4.6}$$

Using the above results, we can rewrite W_0

$$\begin{pmatrix} E'_s \\ E'_f \end{pmatrix} = e^{-i\phi} \overbrace{\begin{pmatrix} e^{-i\Gamma/2} & 0 \\ 0 & e^{+i\Gamma/2} \end{pmatrix}}^{W_0} \begin{pmatrix} E_s \\ E_f \end{pmatrix} \tag{4.7}$$

Note that the absolute phase can be and is often dropped as it is the phase difference that determines the output polarization.

The final step is to transform output light back into laboratory axes

$$\mathbf{E}_{out} = \begin{pmatrix} E'_x \\ E'_y \end{pmatrix} = R(-\psi) \begin{pmatrix} E'_s \\ E'_f \end{pmatrix} \tag{4.8}$$

The complete operation to find the output amplitude vector is thus

$$\mathbf{E}_{out} = \overbrace{R(-\psi)W_0 R(\psi)}^{W} \mathbf{E}_{in} \tag{4.9}$$

Modeling Polarization Dependent Loss A material that shows unequal attenuation along different material axes is considered dichroic. This dichroism can

also be expressed in a Jones matrix through complex index of refraction $\tilde{n} = n - i\kappa$. Again, the indices differ along the fast and slow axes.

$$\begin{pmatrix} E'_s \\ E'_f \end{pmatrix} = \begin{pmatrix} e^{-i(n_s - i\kappa_s)\frac{2\pi d}{\lambda}} & 0 \\ 0 & e^{-i(n_f - i\kappa_f)\frac{2\pi d}{\lambda}} \end{pmatrix} \begin{pmatrix} E_s \\ E_f \end{pmatrix} \qquad (4.10)$$

The imaginary part of the complex index leads to the absorption term which attenuates the signal as it moves through the material

$$e^{-i(n - i\kappa)\frac{2\pi d}{\lambda}} = \overbrace{e^{-ikd}}^{phase} \overbrace{e^{-\alpha d}}^{attenuation} \qquad (4.11)$$

We can separate the phase retardation and the attenuation and express the entire Jones matrix as a product of the two matrices. Knowing that the transmission can be expressed as $T = e^{-\alpha d}$, we write the polarization dependent attenuation matrix as

$$T_{PD} = \begin{pmatrix} T_x & 0 \\ 0 & T_y \end{pmatrix} \qquad (4.12)$$

It is likely that we will know the transmission rather than the complex index or the absorption. Furthermore, we will be more interested in the phase difference rather than the absolute phase. Ignoring absolute phase, we rewrite Equation 4.10 as follows

$$\begin{pmatrix} E'_s \\ E'_f \end{pmatrix} = \begin{pmatrix} T_x e^{-i\Gamma/2} & 0 \\ 0 & T_y e^{+i\Gamma/2} \end{pmatrix} \begin{pmatrix} E_s \\ E_f \end{pmatrix} \qquad (4.13)$$

A simple example of a dichroic element is an ideal linear polarizer which is completely transmissive along one axis while absorbing along the other. Written here is a linear polarizer aligned along the x-axis

$$P_x = \begin{pmatrix} 1 & 0 \\ 0 & 0 \end{pmatrix} \qquad (4.14)$$

We have developed a means of describing components according to their bire-

89

fringent and dichroic effects. Note that Jones Calculus works only for polarized and coherent light which is the case for laser light. Otherwise, one would have to use Mueller Calculus.

4.1.2 Wavelength Dependent Polarization Losses

As shown in Equation 4.5, Γ shows the source of wavelength dependence. In this section, we discuss how birefringent and dichroic elements may be cascaded to create filters with wavelength dependent transmission.

Simple Example of Wavelength Dependent Polarization Effects We start with a simple example demonstrating wavelength dependent polarization effects using two linear polarizers sandwiching an anisotropic medium. Using Equations 4.9
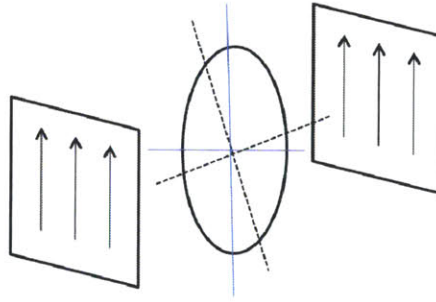

Figure 4-2: Illustration of a basic polarization dependent filter consisting of a uniaxial material sandwiched by two linear polarizers.

and 4.14, the complete operation on the incident light is written as a product of input polarizer, anisotropic medium, and output polarization Jones matrices

$$\mathbf{E}_{out} = P_x R(-\psi) W_0 R(\psi) P_x \mathbf{E}_{in} \tag{4.15}$$

The transmission curve was simulated in MATLAB for an incident vector polarized 45° with magnitude 1. As expected, the maximum possible transmission for this vector incident on a y-axis linear polarizer is 0.5. The plotted transmission is shown in Figure 4-3 as a function fo Γ.
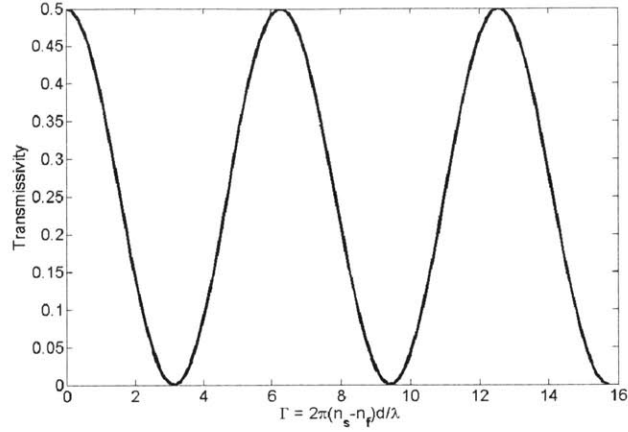
90

Figure 4-3: Transmission curve of uniaxial material sandwiched by perfect linear polarizers as a function of Γ.

Modeling Twisted Fiber In the fiber ring laser, the SM fiber is twisted either by nature or intentionally by the polarization controllers. Though the fiber twist is not determined, we will start with a model where the twist grows linearly. A fan Šŏlc filter is one such model where phase retarders offset an angle ρ from the previous plate are cascaded and sandwiched by linear polarizers. To justify this, we state that the inherent fiber birefringence experiences twist until it meets polarization dependent elements such as the gain cavity or the integrated photonic filter which will create the wavelength dependent effect.

We start by defining the linear function of the twist ψ

$$\psi(z) = \alpha z \tag{4.16}$$

We consider the total phase retardation of the fiber of length l when untwisted given as Γ

$$\Gamma = \frac{2\pi}{\lambda}(n_e - n_o)l \tag{4.17}$$

Note that we have switched "fast" and "slow" with "ordinary" and "extraordinary" and appropriate subscripts. Having defined the fiber length, we can express the total twist ϕ as

$$\phi \equiv \psi(l) = \alpha l \tag{4.18}$$

91

To express the Jones matrix of the fiber, we imagine that the fiber is actually N distinct plates in sequence with angular offset which is multiple of ρ. We write the Jones matrix as a product of N phase retarders with increasing rotation

$$M = \prod_{m=1}^{N} R(-m\rho)W_0 R(m\rho) \tag{4.19}$$

Having divided the fiber into N sections, the total phase difference per plate is simply $\frac{\Gamma}{N}$ which leads us to rewrite Equation 4.4 as follows

$$W_0 = \begin{pmatrix} e^{-i\Gamma/2N} & 0 \\ 0 & e^{+i\Gamma/2N} \end{pmatrix} \tag{4.20}$$

Using the following property of the transformation matrix

$$R(\rho_1)R(\rho_2) = R(\rho_1 + \rho_2) \tag{4.21}$$

and replacing the angle offsets with $\rho = -\frac{\phi}{N}$, we can simplify and rewrite Equation 4.19 as follows

$$M = R(\phi)\left[W_0 R\left(-\frac{\phi}{N}\right)\right]^N \tag{4.22}$$

In simulation, the Šolc filter shows very fine bandwidth. Figure 4-4 shows the filter transmission for increasing layers, or more accurately, subdivisions of the fiber. We see that as N increases, the free spectral range of the line peaks grows. We use the idea of "gradualness" of light rotation as an intuitive tool: smaller N means faster rotation per plate leading to closer peaks while a finer grade leads to widely spaced filter peaks. This applies not only to the number of layers but also to the index difference along the material axes, length of fiber, and total twist. As a general note, small index differences, long fiber length, and smaller twist lead to smaller FSR. In addition, the transmission for different amounts of twist within the range of π are shown in Figure 4-5. While the FSR and location of the transmission peak remains the same, the transmission of the filter inverts as ϕ moves from $\frac{\pi}{2}$ to π.

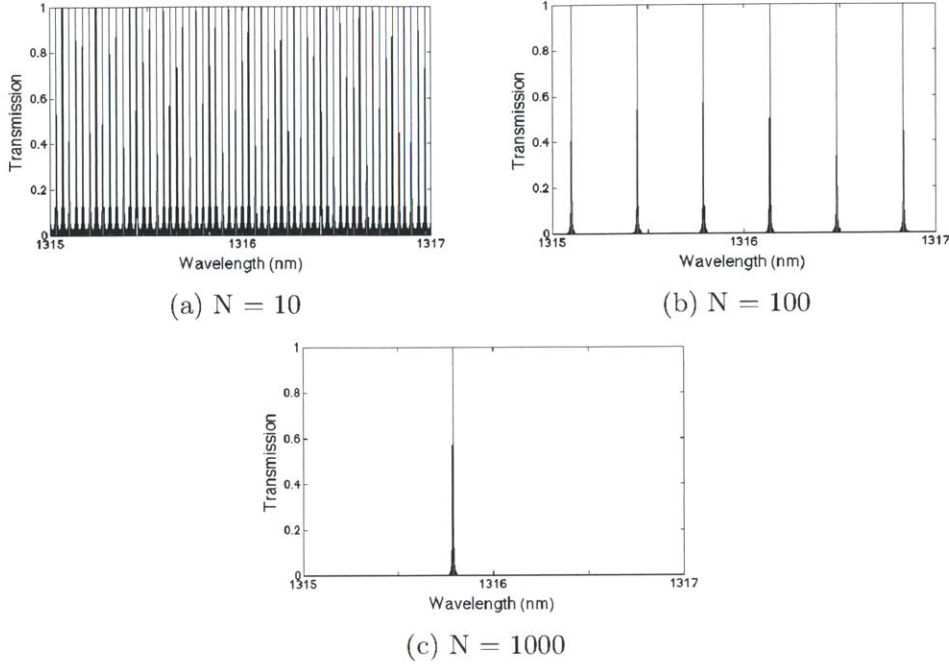Considering that for the fiber, we must take the number of plates N to ∞, we

(a) N = 10

(b) N = 100

(c) N = 1000

Figure 4-4: Simulation of transmission of the Šolc filter for different number of plates. The incident light was linearly polarized along the input polarizer axis.

consider the possibility that the peaks of the filter themselves are not responsible for distinguishing the lasing wavelength. Instead, we see a much flatter profile at work.

To investigate the effects of a polarization dependent loss component, the simulation was repeated with transmission of 0.8 along the x-axis and 0.3 along the y-axis and the incident light linearly polarized 45°. The intent of the simulation was to model the effects of PDL components such as the SOA and integrated filter. The results are shown in Figure 4-6. Unlike previous simulations where the incident light was aligned to a perfect x-axis polarizer with flat profiles, the transmission now shows a band when zoomed in shows the curve oscillating between 0.2 and 0.07 transmission.

The simulation was repeated with the PDL plates rotated 90°. Figure 4-7 shows the transmission for both simulations in a much smaller wavelength range. We find that rotation of the PDL plates offsets the filter transmission supporting the idea that twisting the fiber or changing the orientation of components in the fiber ring laser can act as a wavelength selection mechanism in addition to the comb filter. The period of the filter is on the order of 0.01 nm or 1.75 GHz. The polarization effects

93

(a) $\phi = \frac{\pi}{2}$

(b) $\phi = \pi$

(c) $\phi = \frac{\pi}{4}$
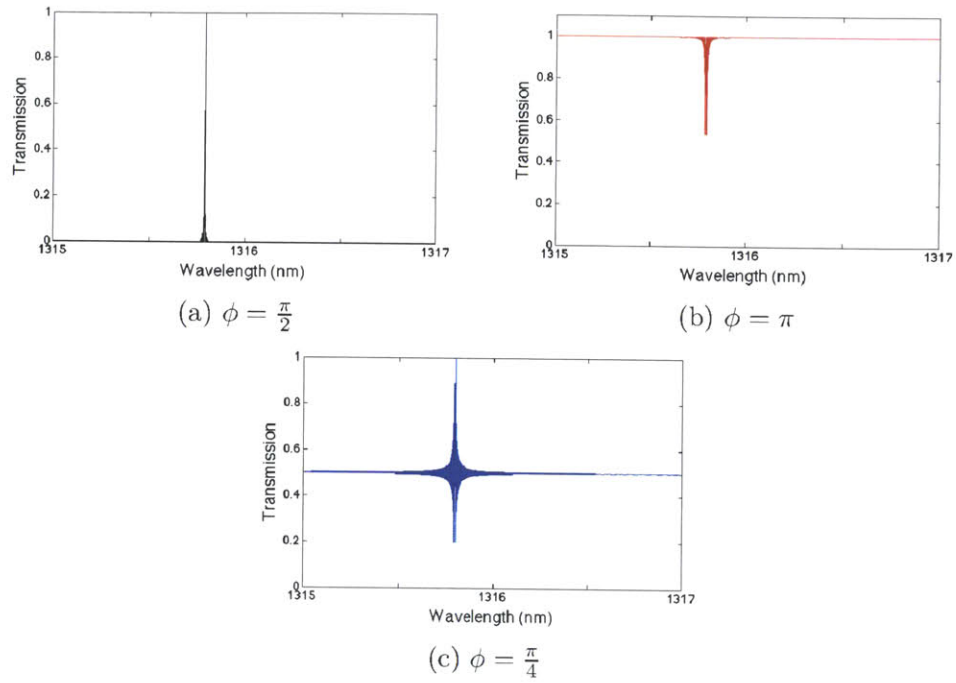
Figure 4-5: Simulation of transmission of the Šolc filter for varying degrees of twist. Again, the incident light was linearly polarized along the input polarizer axis.
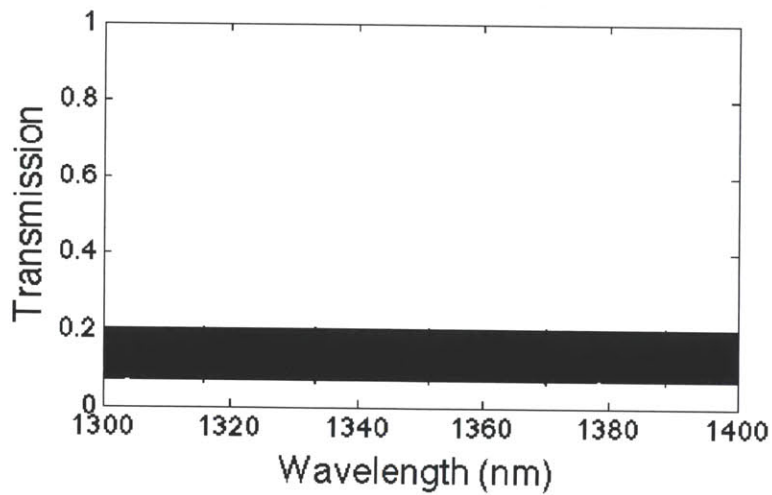

Figure 4-6: Transmission curve of modified Šolc filter with polarizers replaced with PDL component modeling the SOA. The transmission of the x and y-axes were 0.8 and 0.3 respectively with incident light 45° linearly polarized.

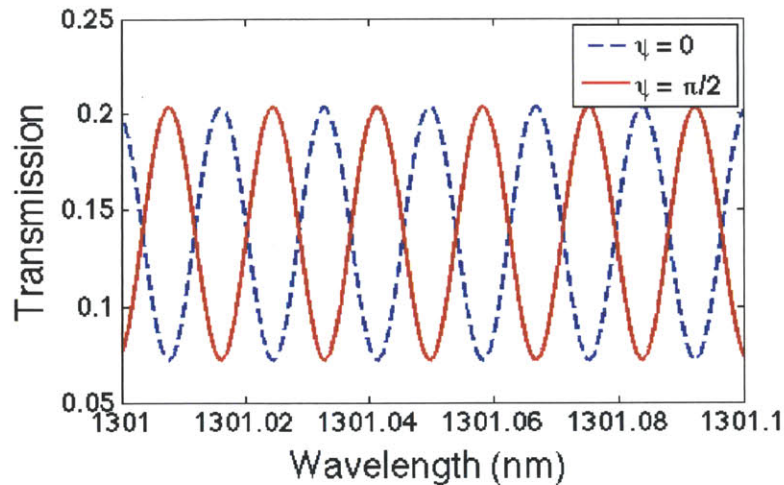are thus a finer selection tool than the comb filter.

Figure 4-7: Transmission curve of PDL Sŏlc filter close up for rotations of 0 and 90 degrees.
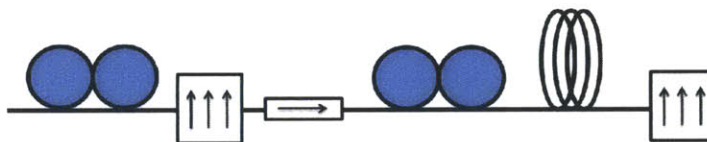

Figure 4-8: Illustration of polarization filter measurement setup. An input polarization controller acted to align the incident light before the input polarizer. A second polarization controller varied the amount of twist in the fiber. Finally, an output polarizer became the selective component of the rotated light. The input and output light was measured to create transmission curves.

Experiments with Polarization Filters To results of the simulations were supported experimentally. Figure 4-8 shows the component arrangement to create a polarization filter. Two in-line polarizers were used as PDL elements. Fiber with added polarization control is contained in the middle to simulate our fiber birefringence.

The transmission of the polarizers is first determined. The PDL elements differ in performance. Figure 4-10a shows the transmission curves of a much better polarizer than Figure 4-10b. The experiment places the weaker polarizer at the input to allow a larger amount of incident light to reach the birefringence. We can imagine that the weak polarizer is the SOA PDL while the strong polarizer is the filter PDL.

The initial results of the experiment had a total fiber length of 2.2 meters and

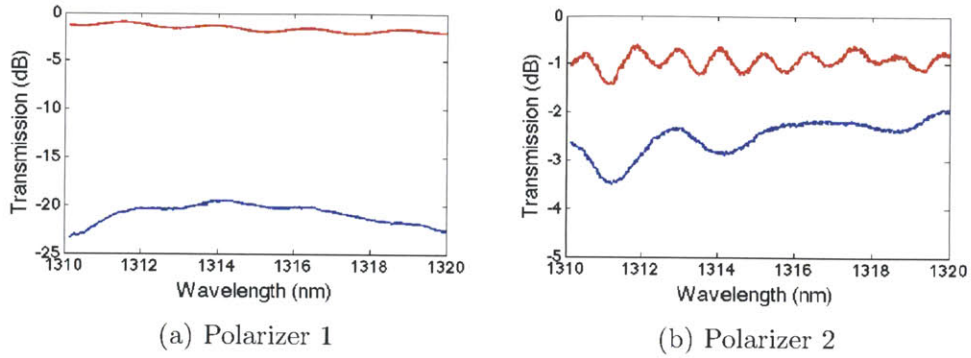(a) Polarizer 1   (b) Polarizer 2

Figure 4-9: Transmission curves for two in-line polarizers with red curves showing high transmission alignment and blue curves showing low transmission alignment. Polarizer 1 has better performance as a linear polarizer. Polarizer 2 simulates more accurately a component with moderate PDL.

(a)   (b)
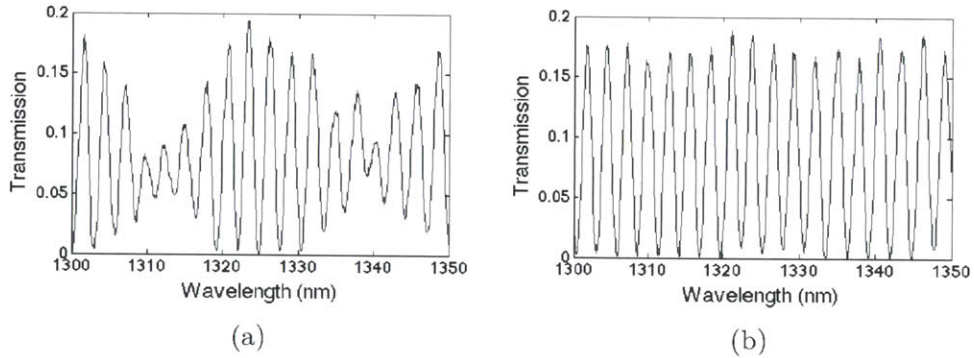
Figure 4-10: Transmission curves of polarization filter with different fiber twist.

compared the filter transmission with varying degress of twist of the birefringent fiber using the second set of polarization paddles. Figure 4-10 shows the results of the experiment. There is no means of quantifying how much the fiber as actually twisted. We can only qualitatively say that the paddles were arranged differently in the two measurements. We clearly see highs and lows in the transmission peak. Furthermore, different polarization settings created distinct transmission shapes.

We repeat the experiment by rotating the polarization of the incident light to maximum and minimum transmission at the output at a wavelength of 1310 nm in attempts to achieve a full 90° rotation of the light. We again keep the fiber twist constant. Figure 4-11 shows the results of the transmission measurement. As shown above in Figure 4-7, we anticipated wavelength offset of a half a period and found
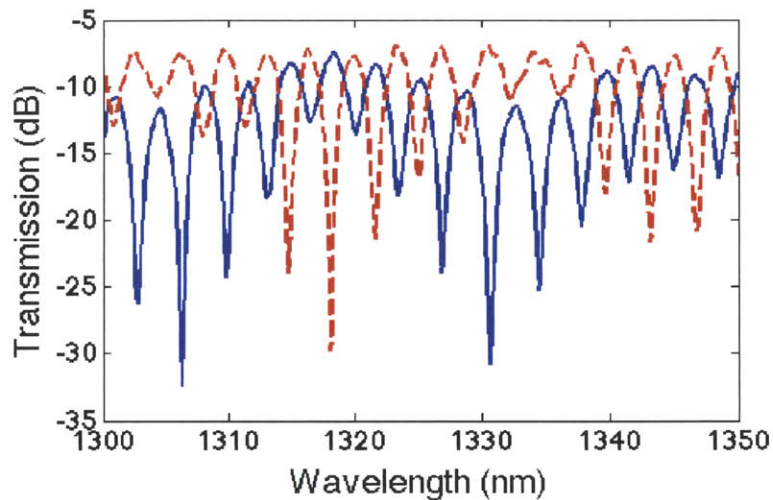
Figure 4-11: Transmission curves of polarization filter at maximized and minimized transmission of 1310 nm wavelength light shown in blue and red respectively.

that the experimental results matched our prediction. Compared to simulated results,

Figure 4-12: Simulated transmission of a 2 meter length filter with index difference of 0.00025 from wavelength range 1300 nm to 1350 nm.

the transmission peak spacing and bandwidth was much larger in experiments. By reducing the index difference from 0.01 to 0.00025, we were able to get similarly spaced peaks in simulation as shown in Figure 4-12.

Finally, we increased the length of the fiber from 2.2 meters to 15 meters while
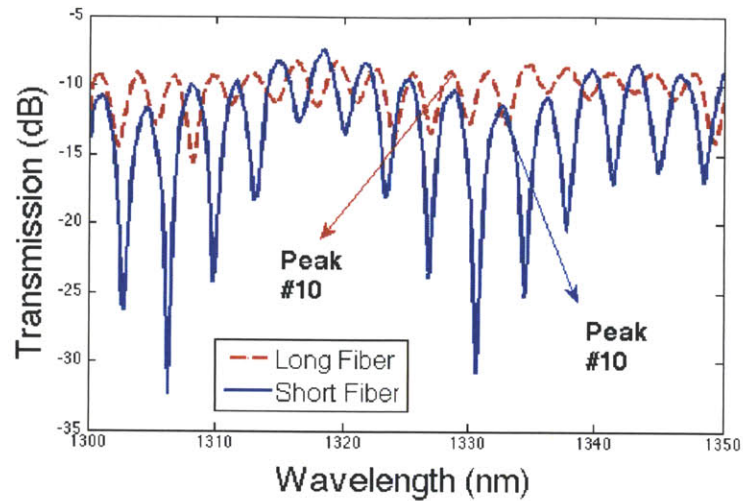
Figure 4-13: Transmission curves of polarization filter of short and long fiber length shown in blue and red respectively.

keeping the fiber twist constant. We see that the longer fiber length compresses the transmission spectra as indicated in the position of the 10th peak in Figure 4-13. Furthermore, the range of transmission is greatly reduced in the long fiber case.
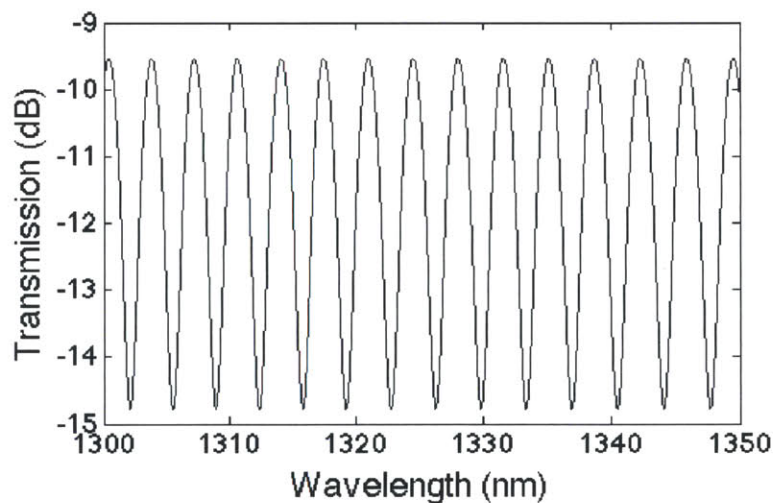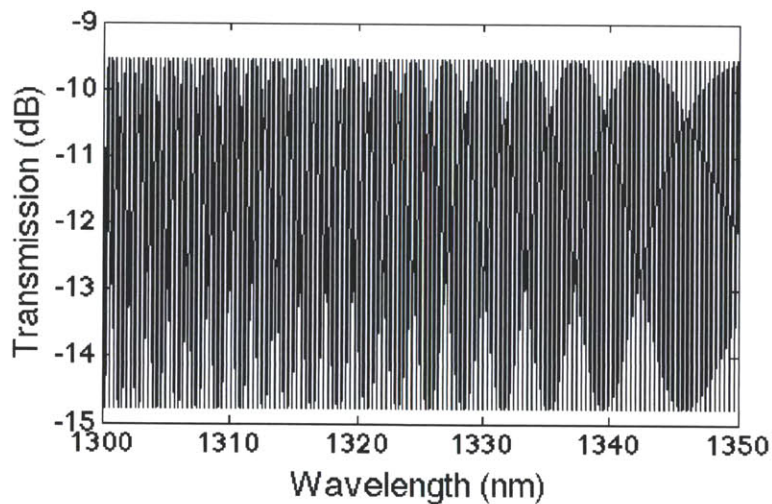

Figure 4-14: Simulated transmission of a 20 meter length filter with index difference of 0.00025 from wavelength range 1300 nm to 1350 nm.

This result is not matched with our simulations of a longer cavity filter 20 meters in length shown in Figure 4-14. As the longer length should increase the range of

98

Γ in our Solc filter model, we expect a denser distribution of filter peaks over the same wavelength range, yet the experiments show that the short and long cavity polarization filter is comparable in peak density. However, we consider this result is due to the fact that the additional "long" fiber is coiled, but there is no polarization controller acting to twist the fiber. Therefore, the model of a linearly twisted fiber applied to the whole length of 15 meter fiber cannot apply.

4.2 RF Spectrum Analysis

Due to some of the unexpected results from the microwave spectra, this section views the problem in reverse by assuming an optical profile at the resolution of the cavity resonance. MATLAB simulations of the microwave spectra are performed and compared to experimental results.

4.2.1 Beat Notes

$$E_2(t) = E_2 e^{-j\omega_2 t}$$

$$E_1(t) = E_1 e^{-j\omega_1 t}$$

$$\omega$$

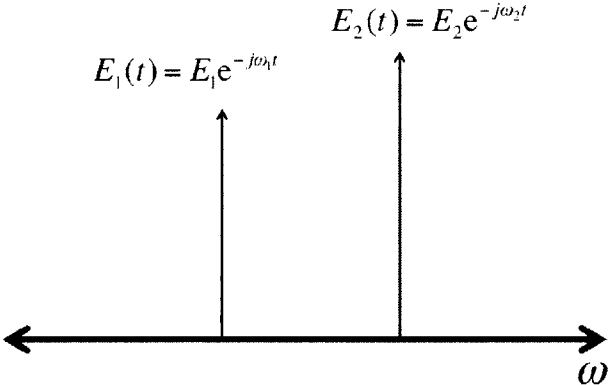Figure 4-15: Illustration of two plane wave signals with time-varying electric fields.

The operation of the microwave spectrum analyzer rests on the concept of a beat note which arises from a function that evaluates the squared magnitude of two interfering waves. Figure 4-15 shows a simple drawing of two plane waves assumed identically polarized with amplitudes E_1 and E_2 and frequencies ω_1 and ω_2. Note

that the absolute phase is ignored. However, it will be considered later in this section.

When the light source is input to the MSA, a photodetector receives the light, and the photocurrent is measured and displayed. The intensity is proportional to the squared magnitude of the total electric field.

$$I = \frac{|E|^2}{\eta} \tag{4.23}$$

We perform the operation on two interfering waves as follows

$$
\begin{aligned}
|E_1(t) + E_2(t)|^2 &= (E_1(t) + E_2(t)) \cdot (E_1(t) + E_2(t))^* \\
&= (E_1 e^{-j\omega_1 t} + E_2 e^{-j\omega_2 t}) \cdot (E_1 e^{+j\omega_1 t} + E_2 e^{+j\omega_2 t}) \\
&= |E_1|^2 + |E_2|^2 + E_1 E_2 (e^{+j(\omega_2 - \omega_1)t} + e^{-j(\omega_2 - \omega_1)t}) \\
&= |E_1|^2 + |E_2|^2 + 2 E_1 E_2 \cos(\omega_2 - \omega_1)t
\end{aligned}
\tag{4.24}
$$

The first two terms of the results of Equation 4.24 are the DC components. However, a third term arises and furthermore is sinusoidal. We isolate and rewrite it as the intensity of the beat note, I_{beat}

$$I_{beat} = 2 E_1 E_2 \cos(\omega_2 - \omega_1)t \tag{4.25}$$

The beat note oscillates at a frequency ω_{beat} that is the difference of the first two field frequencies

$$\omega_{beat} = \omega_2 - \omega_1 = \Delta\omega \tag{4.26}$$

4.2.2 Linear Multimodal Analysis without Phase

For more than two modes which is the case with the multiwavelength ring laser, we express the intensity as being proportional to the following

$$I_{mm} \propto \left| \sum_{i=1}^{N} E_i \right|^2 = \sum_{j=1}^{N} \sum_{k=1}^{N} E_j E_k \tag{4.27}$$

We can relate the intensity to the autocorrelation function $R_{xx}(j)$ where j describes the frequency of the beat note and distance between field components that contribute to the beat note power

$$R_{xx}(j) = \sum_{i=N/2}^{N/2} x_i x_{i-j} \tag{4.28}$$

Indeed, the autocorrelation at $j = 0$ returns the DC component which is simply the sum of the field amplitudes squared

$$R_{xx}(0) = \sum_{i=N/2}^{N/2} x_i^2 \tag{4.29}$$

Using Equation 4.27, we make a prediction of the microwave spectra under the circumstances that the field amplitudes are perfectly matched to the shape of the envelope of the laser and filter. We approximate the shape of the envelope as a Lorentzian centered at x_0 and bandwidth γ

$$f(x_0, \gamma) = \frac{1}{\pi} \left[\frac{\gamma}{(x - x_0)^2 + \gamma^2} \right] \tag{4.30}$$

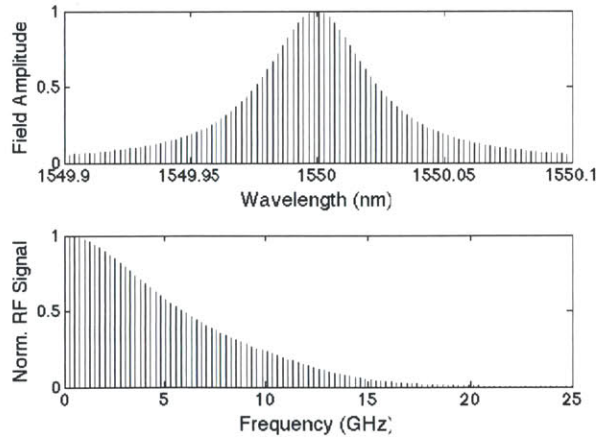The top of Figure 4-16 shows the simulated mode distribution of the field amplitudes

Figure 4-16: Illustration of two plane wave signals with time-varying electric fields.

for a laser with 6.25 GHz bandwidth. The cavity mode spacing is 250 MHz, or 100

modes within a 0.2 nm span. The bottom of the figure shows the predicted microwave spectrum normalized to the DC power. The spectrum has a bandwidth of 2γ.

4.2.3 Effect of Random Phase

The simulation shown in Figure 4-16 is what was expected, but not observed in experiments. However, the above model neglects the absolute phase. We now include the phases φ_1 and φ_2 and rewrite the expressions for the sum of the two plane waves from Section 4.2.1 as

$$E_1(t) + E_2(t) = E_1 e^{i\varphi_1} e^{-i\omega_1 t} + E_2 e^{i\varphi_2} e^{-i\omega_2 t} \qquad (4.31)$$

(a) Mode spacing = 250 MHz   (b) Mode spacing = 25 MHz

Figure 4-17: Simulation predicting microwave spectrum of a laser with amplitude profile of 6.25 GHz bandwidth scaled with absolute phases for the 250 MHz and 25 MHz cavity mode cases. The dotted red line shows the prediction without accounting phase.

To model the presence of absolute phase, we made the assumption that the modes were uncoupled and uncorrelated. For each mode, we scaled the mode amplitudes by $e^{i\varphi}$ where φ is a phase which was randomly generated from a uniform distribution. We then repeated the calculation of Equation 4.27 with new mode amplitudes. Figure 4-17 shows the results of the MATLAB simulation for 6.25 GHz bandwidth profile for cavity mode spacing of 250 MHz and 25 MHz.

The addition of phase greatly reduced the beat note amplitudes of the microwave

spectra. Furthermore, we find that a greater number of modes leads to improvements in the relative noise intensity as the noise grows slower than the the DC component. Suppression of the beat notes also makes it difficult to identify the Lorentzian fall-off of the original prediction.
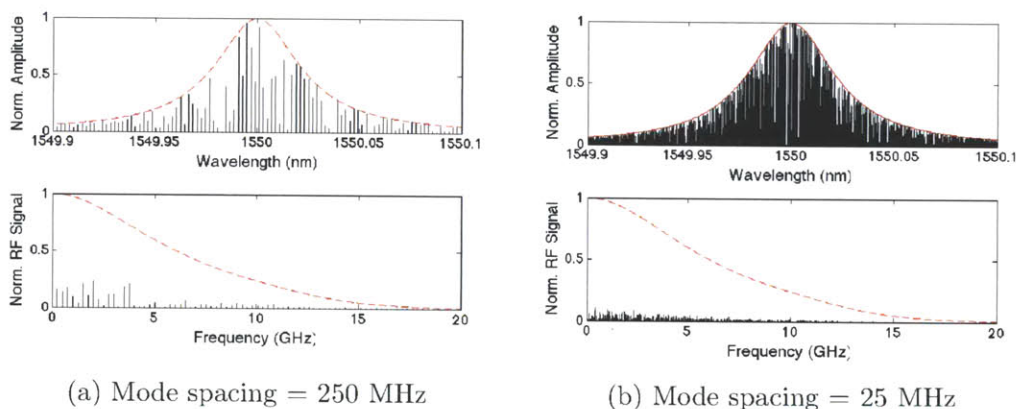

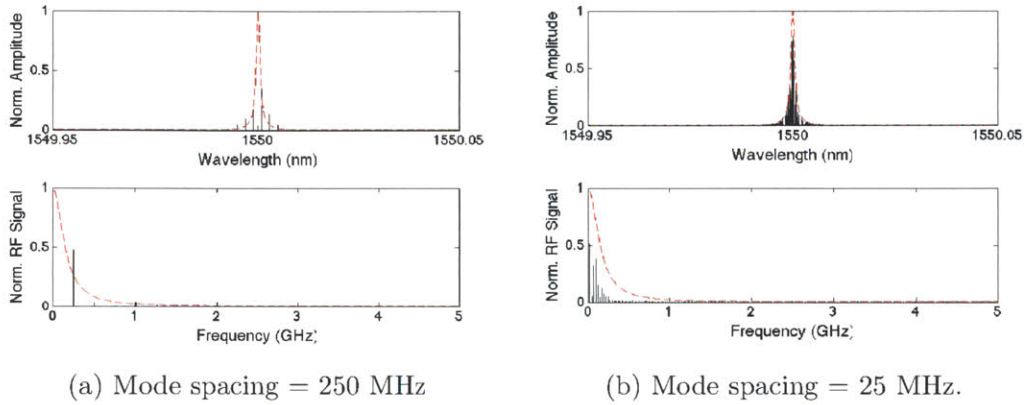(a) Mode spacing = 250 MHz   (b) Mode spacing = 25 MHz.

Figure 4-18: Simulation predicting microwave spectrum of a laser with amplitude profile of 150 MHz bandwidth scaled with absolute phases for the 250 MHz and 25 MHz cavity mode cases. The dotted red line shows the prediction without accounting phase.

The simulation was repeated for a filter of a much narrower bandwidth of 150 MHz. Again, the mode spacings were maintained at 250 MHz and 25 MHz. Figure 4-18 shows the results of the simulation. The dotted red line show the predicted results without accounting for phase, and indeed, we see that the 150 MHz filter would have fallen much faster than the 6.25 GHz filter.

We take the results of the 25 MHz spectra for the 6.25 GHz and 150 MHz bandwidths and compare. The spectra are shown in Figure 4-19. The conclusions we can make are that the presence of more modes seems to help suppress the beat notes because of phase noise averaging. The spiking behavior of the narrow bandwidth laser near the origin are familiar and observed in Figure 2-25. These results also feel consistent with the lower noise observed when modulating all wavelengths at once rather than a single filtered wavelength as shown in Figure 2-19.

However, these results also predict that the narrow bandwidth beat notes should fall away within the filter bandwidth while Figure 2-25 show that the modes persist
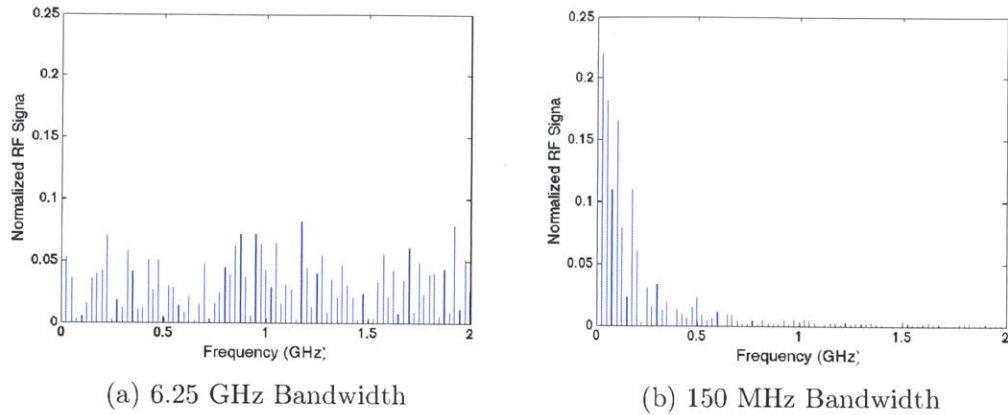
(a) 6.25 GHz Bandwidth   (b) 150 MHz Bandwidth

Figure 4-19: Simulated microwave specta for filter bandwidths of 150 MHz and 6.25 GHz at frequencies up to 2 GHz for beat note spacing of 25 MHz.

well outside of it. Furthermore, the noise observed for the large bandwidth laser is still more than predicted simulations tell. As a result, the conclusion is that though phase may be responsible for some suppression of sideband noise, it is an incomplete explanation of the presence of frequency noise on the microwave spectra.

4.3 Conclusion

We have developed a theory for the wavelength dependence of polarization in birefringent fiber cascaded with polarization dependent loss components and demonstrated the results of simulating this dependence. We find that degree of twist, length of fiber, polarization dependent loss, and angle of incident light all play a role in creating the transmission curve. We have also shown experimentally that the fiber birefringence in conjunction with polarization dependent elements can indeed have transmission that is not only wavelength dependent but can also be manipulated through adjustments to the polarization inside and outisde of the PDL components. Therefore, we have demonstrated a third level of wavelength selection in addition to the cavity resonances and the comb filter peaks and shown how polarization dependent loss and single wavelength operation can occur.

Furthermore, we have performed an analysis of the microwave spectrum by cal-

104

culating and simulating the power spectral density. We first neglected the effects of phase to see that our original predictions more closely matched a situation where the wavelengths were phase correlated. By introducing phase and therefore assuming uncorrelated wavelengths, we have been able to simulate the effects and found that uncorrelated modes result in reduced relative intensity of noise. Furthermore, we find that the more modes we have, the more the noise decreases. This supports the experimental results. Simulations were performed for filter bandwidths matching the commercial Micron Filters. While we had found that there are some aspects of the microwave spectra that appeared consistent, our model could not explain the persistence of noise well beyond the filter bandwidth of the 150 MHz filter that appeared nearly identical to the noise in the 6.25 GHz bandwidth case. As a result, the analysis remains incomplete.

Chapter 5

Conclusion and Future Work

5.1 Conclusion

In this thesis, we have presented the argument for the necessity of a photonic laser source. This topic continues to be a major area of research with many unique solutions. Our approach chose to externalize the gain while using integrated components. The external gain provides the advantages of reducing the electrical and thermal load on the chip socket, avoiding the challenges of integrating gain mediums into CMOS processes, allowing for lasing at virtually arbitrary wavelength, and though still elusive, the possibility of multiwavelength operation with a shared gain medium. The advantages of using integrated resonators were the elimination of closed-loop control of wavelength tuning, ability to control laser output and wavelength on-chip, and the potential of wavelength modulation using novel resonator designs.

The experiments presented in this thesis began with commercial components. We were able to apply known characterization techniques for a laser that began as an unfamiliar system. Threshold current, slope efficiency, and wall-plug efficiency could be defined for the laser even under multiwavelength operation. We found that our model was accurate up to the limit of our knowledge of the polarization. Furthermore, we presented microwave spectra data that at the time of this writing has note been presented in research for lasers of similar structure and design. The results have opened the door to understanding the operation of a laser on a more fundamental

level.

As we progressed to using micro-ring resonators, we were able to successfully reapply the analysis performed in the experiments using the commercial filters demonstrating consistency in the theory as we moved to the integrated components. Furthermore, the advantages of an integrated ring resonator are demonstrated through successful tuning of the laser while in operation. The nature of the resonator structure has allowed for wavelength modulation experiments to begin. Furthermore, we have also been able to demonstrate an open eye in a communications link experiment as a testament to the laser's future usability as a data carrier.

We have also developed a theory for the role of birefringence in selecting the wavelength. One of the particular aspects of this laser is the ability to function as either a single or multiwavlength laser by simply adjusting polarization paddles. We have shown that the combination of fiber and possible integrated material birefringence together with the polarization dependent losses of components can create wavelength dependent transmission through the cavity thus having different wavelengths see different losses in the cavity. Also, the role of phase correlation in multimodal operation was simulated, and it was found that the laser in multimode operation shows random phase. This will be interesting in future work that will study the modes of the laser as set of coupled and uncoupled oscillators and the implications of such.

5.2   Future work

Future work in this topic sits along the spectrum of theory and application. As the POEM program continues, the pursuit of a multiwavelength laser source at wavelengths 1180 nm, 1280 nm, and 1550 nm is still ongoing. Meanwhile, a full understanding of the physics of the laser, let alone a means of engineering an optimal version, has yet to be reached. The following section addresses some of the necessary future work in the ongoing research of the multiwavelength ring laser.

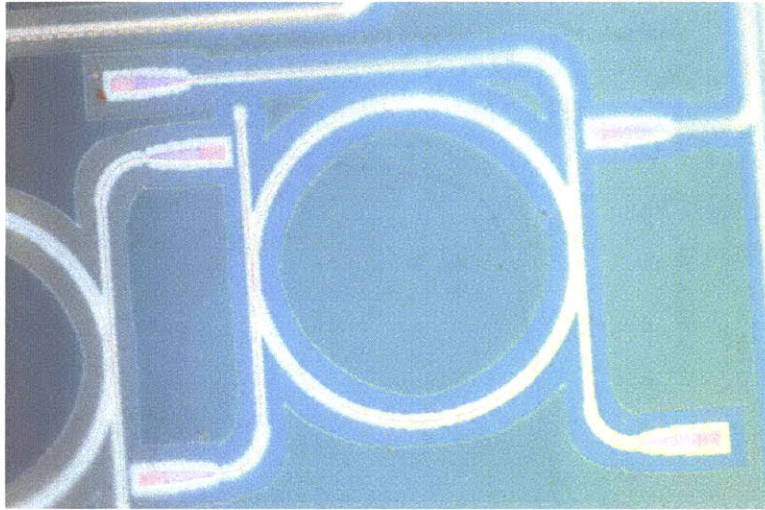### 5.2.1   Integrated 1180 nm Ring Laser

Figure 5-1: Large rings on EOS18 systems chips were designed for a small FSR in the 1180 nm range to encourage multiwavelength lasing. The losses through the drop ports exceeded 30 dB while the through port coupling showed losses of 14 dB.

Micro-Ring Resonators with Small FSR   Attempts to create an integrated multiwavelength 1180 nm laser source were started, but the experiment is incomplete. On EOS16 system chips, silicon micro-ring resonators with 1180 nm grating couplers and large radius were laid out to support multiwavelength experiments. Figure 5-1 shows a photograph of the ring resonator. However, coupling through the drop port of the ring proved unsuccessful as the fiber-to-fiber loss typically exceeded 30 dB. A 14 dB fiber-to-fiber coupling loss was achieved at the through port. Regardless, the experiment went forward with the through port as the output of the ring filter.

Innolume 1180 nm SOA   A quantum dot SOA from Innolume was obtained for experiments at lower wavelengths. The SOA has a typical gain of 18 dB at its recommended operating current of 500 mA defining a low limit on total loss in the system in order to see threshold. However, the gain curve shows that the peak wavelength occurs near 1200 nm. We anticipated that lasing would occur at wavelengths higher than the desired 1180 nm if it occurred at all.

1180 nm Laser Setup   The initial setup for the 1180 nm ring laser placed the isolator at the output of ring resonator. The fibers of the resonator were also
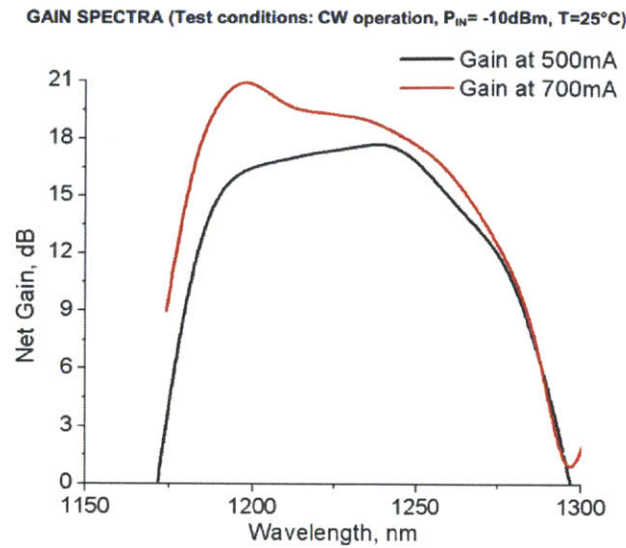
Figure 5-2: Gain curve of Innolume SOA from data sheet. The Innolume SOA has a maximum gain of 21 dB at a bias current of 700 mA near 1200 nm and typical gain of 18 dB at a bias current of 500 mA.
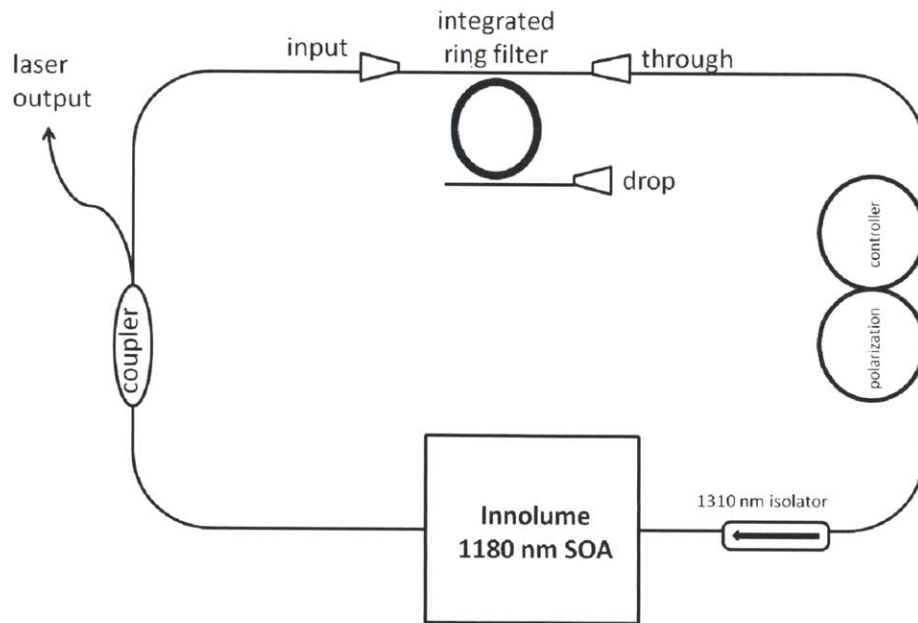
Figure 5-3: Illustration of first iteration of Innolume ring laser. The through port acts as the output port of the ring filter. The fiber length of the external components is 6.6 meters. The coupling fibers add approximately 2 meters.

threaded through a polarization controller which acted to twist the fibers and allow limited adjustment of polarization before launching into the polarization dependent

Innolume SOA. The coupler allowed for 50% output. We note that the isolator and coupler are the same devices from Micron Filter experiments from Section 2.6.1 and are designed for operation in the 1310 nm range.
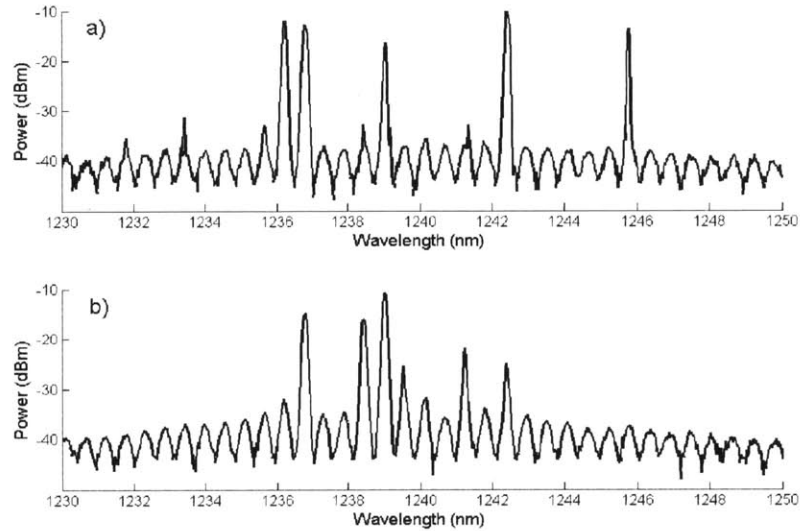

Figure 5-4: Optical spectra of laser output with ring cavity connected or disconnected. a) The output of the ring laser showed resonances that did not seem to come from the cavity or ring resonator modes. b) Disconnecting the output of the ring resonator from the input of the isolator showed identical behavior.

The resulting laser output was not stable, but it also showed unexpected behavior. The optical spectrum of the showed resonances that did not match cavity or ring resonator peaks. In addition, disconnecting the cavity at the ring resonator output and viewing the laser output spectrum showed the same results leading to the conclusion that a bidirectional cavity was formed between the SOA and ring resonator input as seen in Figure 5-4.

To prevent this bidirectional cavity, a second isolator was placed at the SOA output increasing the cavity length by 2.2 meters. The results after adding the second isolator to prevent back reflections between the ring resonator input and SOA output eliminated the oscillations from Figure 5-4. The laser spectrum in Figure 5-6 shows the lasing wavelength near 1228 nm. However, the laser output was far from stable, and changing the polarization seemed to affect the laser behavior very little. Further-
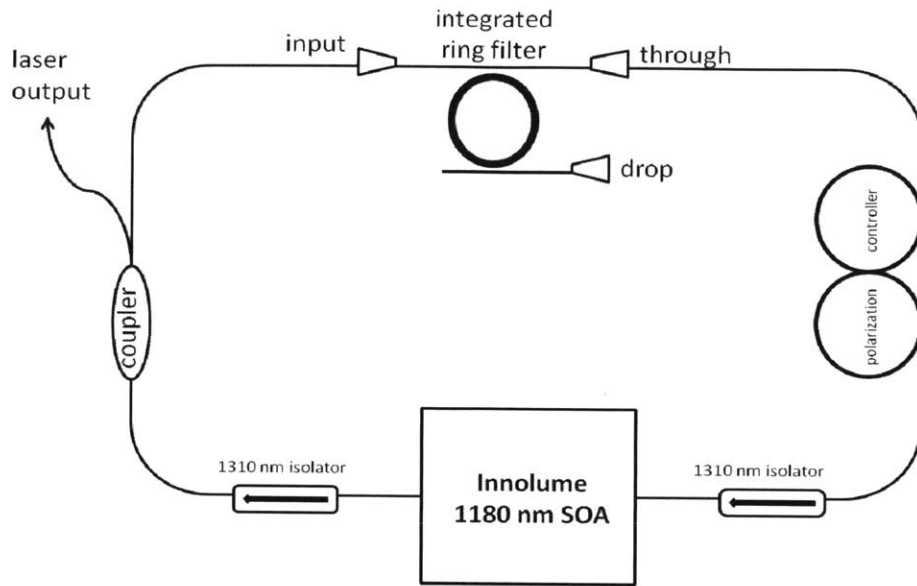
Figure 5-5: Illustration of second iteration of Innolume ring laser. The additional isolator at the output of the SOA brings the total external component fiber length to 8.8 meters. The coupling fiber length is still 2 meters.
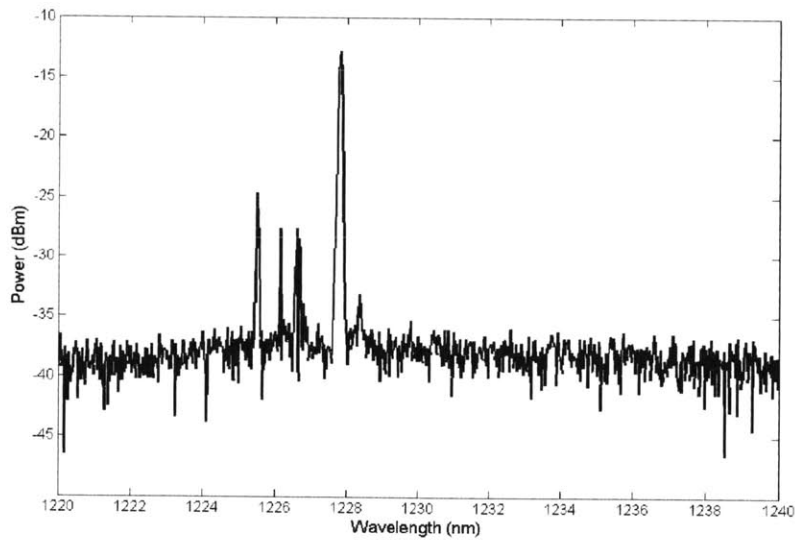
Figure 5-6: Optical spectrum showing output of laser with modified layout at a current bias of 500 mA. The output was unstable and did not maintain a lasing wavelength. Spikes were visible near the 1230 nm wavelength.

more, the laser at this point was operating with the SOA pushed to its recommended current of 500 mA. As a result, collecting LI data proved too difficult for this laser,

and further experiments with this setup were abandoned.

Innolume SOA with Micron Filter The experiments were continued using the commercial 1310 nm Micron Filter. Figure 5-7 shows the optical spectra taken
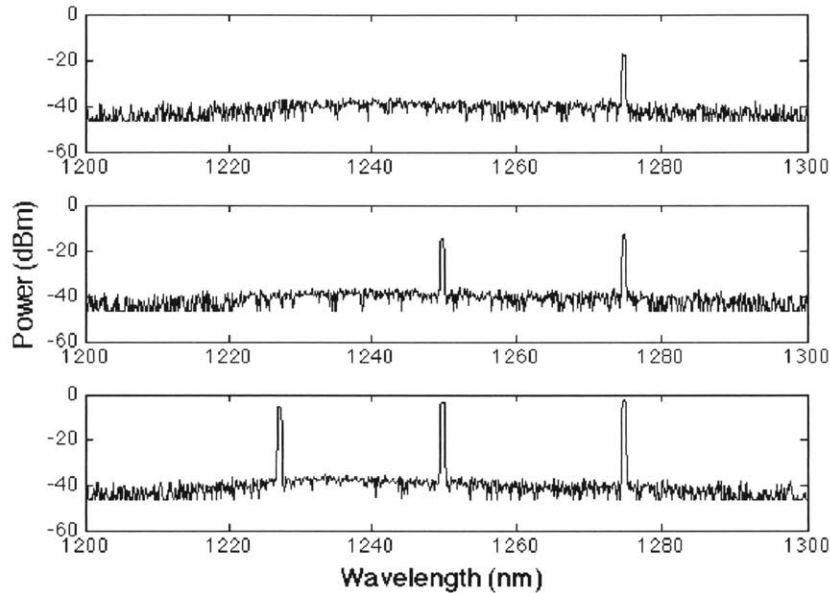
Figure 5-7: Optical spectra of the ring laser using the Innolume Quantum Dot SOA. The spectra are taken from top to bottom at bias currents of 13 mA, 14 mA, and 46 mA.

at different bias currents. Recalling that the Micron Filter has a mode spacing of 0.4 nm, the results of the spectra show mode spacing closer to 25 nm. Furthermore, the polarization was adjusted for stable single mode lasing before increasing the bias current. Without adjustments to the polarization, the spectrum centered around 1250 nm was unstable.

We hypothesize that polarization adjustments were successful at suppressing side modes at lower bias currents, and that the rise of the new far apart side modes are credited to other sub-band transitions. The quantum dot density of states is delta functions at the sub-band energies, and we expect rather sudden rather than gradual contributions of carriers with increasing bias current. The gain contribution from these sub-bands are also capable of creating multiwavelength combs centered around

1275 nm and 1225 nm respectively, but the polarization condition was particular enough to create "single-modes" at these wavelengths.

5.2.2 Physics of Multimode Operation

The ring laser with external gain and comb filter is a dynamic and unstable system with observed exchanges of power between wavelength peaks of the filter and even within a single filter peak. It is also interesting that we are able to coax the laser into single-mode lasing through adjustments to the polarization, but with increasing bias current, the laser inevitably becomes multiwavelength. Many questions are left unanswered with regards to the multiwavelength laser dynamics.

However, we have learned that multiwavelength behavior is not always guaranteed, and one can guess some of the circumstances in which it happens. The gain profile and wavelength dependent loss must be such that the modes of interest all experience equal gain. In addition, the gain medium must saturate inhomogeneously to some degree so that mode competition will not completely suppress struggling side modes. In this section, we discuss some points that might help begin exploration of the physics of semiconductor gain and how it could lead to multimode operation.

Gain Compression   We have observed at high bias currents that even when the laser is operating in "single-mode", there is a point at which the single-mode behavior cannot be maintained and the laser transitions into multiwavelength operation. It is possible that the gain is compressing at that photon energy, and that wavelength is no longer monopolizing the energy of the inverted carriers.

In a multimode system, we are interested in the gain compression at different photon energies. The rate expressions in the multimode case express the photon densities as $N_{p,i}$ for the ith mode, but the carrier density is shared. To be able to describe in detail the point at which the gain medium is unable to support a particular ith mode due to gain compression but is able to begin to supply its carriers to other modes will be an important step towards understanding the multimode laser.

Homogeneous and Inhomogenenous Saturation Furthermore, homoege-nenous and inhomogeneous broadening and saturation effects are important to understand since it will convey to us if the laser we envision, the ring laser with single frequency lasing under each comb filter peak, is even possible. For this to happen, we required homogeneous saturation on the order of the comb filter bandwidth but inhomogeneous saturation on the order of the comb filter free spectral range.

We have already mentioned the inhomogeneous gain of a quantum dot SOA due to its discrete density of states, but we also need to examine the homogeneous broadening effects of bulk and quantum well SOAs. In particular, energy broadening of the electron allows for many state transitions rather than just one state transition to contribute to a specific photon energy. Exploration of this subject will help us to understand the scale at which this phenomena occurs and how it affects the laser.

Nonlinear Effects The nonlinearities of the semiconductor medium have not been well-researched over the course of this work, but certainly, the effects should be examined more closely. In particular, the Kerr effect and intensity dependent changes in the index of refraction are certainly at work, and furthermore, four-wave mixing phenomenon is often observed in SOA mediums that one should consider looking at how it may play a role in this system. Finally, with our arguments from Chapter 3 about uncorrelated phase, we should consider examining the effects of correlated such as with a mode-locking system.

5.2.3 Next Steps in Integration

Much of the integrated experiments performed utilized devices that were already available. As more was learned about the capabilities of the laser, it became interesting and necessary to plan devices on future tape-outs specifically for this work. From Section 5.2.1, we have already shown the need for a new iteration of a large 1180 nm MRR in order to continue the experiments. This section will address some of the logical next steps in the integration of the ring laser.

Thermal Tuning and Wavelength Modulation Section 3.3 discussed the frequency limits of the measurements due to the use of DC probes. GSG Probes designed for high frequency signals must be used to accurately determine frequency rolloff. The placement of the probe pads shown in Figure 3-5 is the primary issue as the pads required access from the front and back of the probe station setup. As a result, a future layout of this device should consider pad placement for ease of access from the front by a GSG probe. In addition, because the resistive heating mechanism is a novel method, it would be interesting to continue incorporating doped rings in a variety of ring resonator designs in future tape-outs.

Integrated Micro-Ring Resonator Banks As mentioned above, investigation of more interesting filter structures could lead to novel operation of the laser. Early experiments aimed to use an 11-channel filterbank from EOS14. Figure 5-8

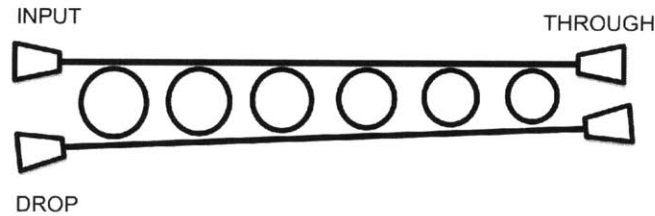INPUT   THROUGH

DROP

Figure 5-8: Cartoon illustrating a 6 channel filter bank structure. Proper realization of the structure would lead to individually tunable wavelengths with multiplexed input and drop ports.

shows an illustration of the aforementioned filter structure except with 6 rather than 11 resonators. The notable features are not only the shared input to through waveguide but also the shared drop port allowing for a multiplexed output. The separate resonators are all slightly different in size and thus designed for different peak wavelengths. Furthermore, the rings would have their own tuning structures allowing for individual wavelength control. The benefits of such a structure are that it allows for a multiwavelength laser that gives independent control of each wavelength without disrupting the external gain medium.

Early transmission measurements of the filterbanks showed nondistinguishable resonance peaks, however, and though it may have been beneficial to attempt the
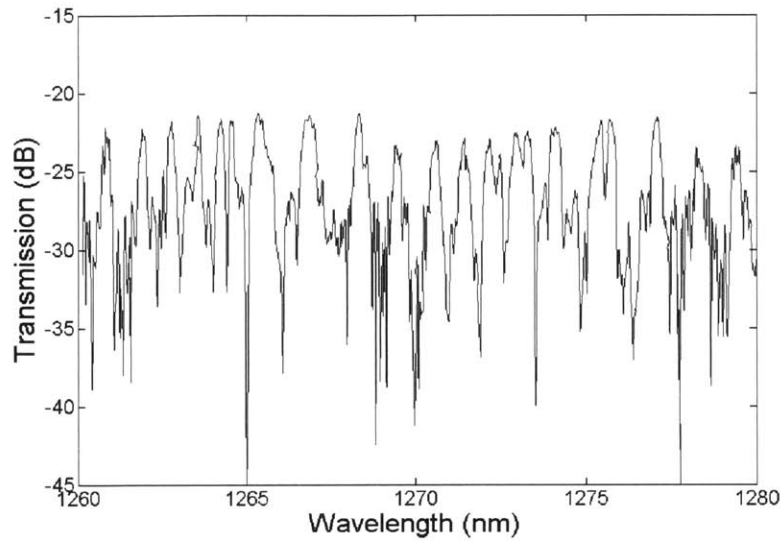
(a) from EOS14 Test Chip 1
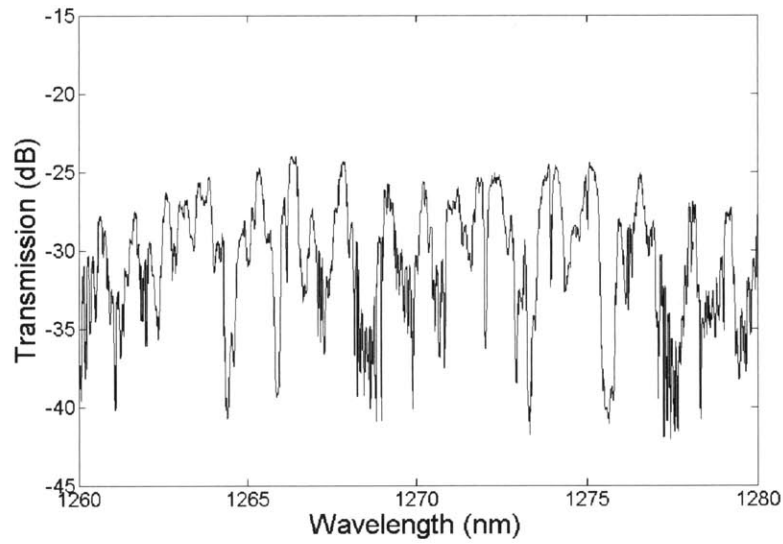
(b) from EOS14 Test Chip 2

Figure 5-9: Transmission function of 11-channel filterbanks from two different EOS14 test chips.

multiwavelength laser anyway, the effort was put on hold. It is suspected that the inter-ring paths were also contributing to the transmission function, and future designs for the filterbank planned higher order filter designs to eliminates these unwanted resonantces.

Integrated Cavity and Direct Modulation   Fabricating the entire laser cavity on chip leaving only the SOA directly coupled into the chip is the eventual and final packaging goal of the laser. This means the output coupler and micro-ring resonator will be completely contained on chip, and the coupler output could pass directly into other devices such as a modulator or other MRRs for wavelength selection.

This presents several advantages and scenarios for study. First, the polarization dependent effects observed in the previous experiments are largely eliminated as the fabricated devices are polarization maintaining. Experiments utilizing polarization maintaining fiber were planned but difficult to accomplish as all components needed to have PM fiber pigtails.

Second, a fabricated cavity greatly minimizes the total cavity length. On this note, the fiber ring structure of the laser should be taken into reconsideration as this would require a fiber exiting the chip and returning to the SOA input. There are a great deal of advantages of eliminating fiber entirely not only from the packaging perspective but also from the number of simplifications that can be made to better control the laser behavior. Utilizing an etalon cavity such as the one shown by Jeong et. al may be the most practical choice in terms of packaging ease and minimizing cavity length, and using integrated filters such as the filterbanks discussed in Section 5.2.3 would further simplify the input and output coupling.

Finally, the self-tuning can be observed and eliminate the need for wavelength alignment in the future. The system is simplified down to just an input SOA, and with laser outputs passing directly into active and passive devices, the performance of the devices can be evaluated more easily. This assumes that the noise and communications of the laser has been improved, but we expect that integration of the cavity would bring us closer to a high performing laser that meets the needs of a variety photonic applications.

Appendix A

MATLAB Simulations

A.1   LI Curve Generator

```
powerdB = zeros(1,100);

wlindex = zeros(1,100);

wlvariation = zeros(1,100);

current = linspace(3,300,100);


A =length(powerdB);

for i = 1:A;

    [powerdB(i), wlindex(i)] = max(spectra(i,:));

    %powerdB(i) = sum(10.^((spectra(i,:))./10));

    index = wlindex(i);

    wlvariation(i) = wavelength(index);

end


powermW = 10.^(powerdB./10);

%powermW = powerdB;

powermW2 = powermW./0.79;

figure; plot(current, powermW2, '-');
```

```
%sm = [50,46,44,43,41,40,38,37,35,33,31,29,28,26,21,20];
%for i=sm;
%    i
%    powermW2(i)=[];
%    current(i) = [];
%end


%A = length(powermW2);
%current = current(sm);
%powerdB = powerdB(sm);



figure; plot(wlvariation, powerdB, 'o');
figure; plot(current, wlvariation);

 %figure; plot(powermW2,'o');
 %hold
 %plot(powermW2, 'o');

figure; plot(current, powermW2, 'o');

%figure; plot(current, powermW,'o');
%grid on
%hold
%plot(current,powermW2, 'o');

% figure; plot(current(sm), powermW,'o');
% hold
% % plot(current(sm),powermW2, 'o');
```

```
dB_offset = 10*log10(1/0.79);

powerdB2 = powerdB + dB_offset;

% powerdB2 = powerdB + dB_offset + 1.8;


powermW3 = 10.^(powerdB2./10);

% plot(current,powermW3,'o');



current = current(1:A);

powermW = powermW(1:A);

powermW2 = powermW2(1:A);


p1_coeff = polyfit(current, powermW, 1)

p2_coeff = polyfit(current, powermW2, 1)


p1_fit = p1_coeff(1).*current + p1_coeff(2);

p2_fit = p2_coeff(1).*current + p2_coeff(2);


slope_efficiency = p2_coeff(1)/1


%plot(current, p1_fit, 'k')

hold; plot(current, p2_fit, 'k')
```

A.2 Wall-Plug Efficiency Curve Generator

```
% typical laser values


Io = 30;

Go = 16.2840;
```

```
P_opt = 10;
hv_q = 0.925;


loss_internal = -7.5;
loss_ratio = 10^(loss_internal/10);


R = linspace(0.01,1,100);
alpha_mirror = log(1./R);
alpha_internal = log(1/loss_ratio);


loss_total = exp(-(alpha_mirror + alpha_internal));


Gth = 10*log10(1./loss_total);
Ith = Io.*exp(Gth./Go);


eta_d = alpha_mirror./(alpha_mirror + alpha_internal);



P_elec = (P_opt./eta_d) + (hv_q.*Ith);


eta_wall = P_opt./P_elec;

figure;
%plot(R, Gth);
%figure; plot(Ith, Gth);
%subplot(3,1,1);
%plot(R, Ith)
%subplot(3,1,2);
%figure;
```

```
%plot(R, eta_d)
%subplot(3,1,3);
%figure;
plot((1-R), eta_wall)


% %I = linspace(0,100,100);
%
% %eta_d = eta_i*log(1./R)./(log(1./R) + alpha_internal);
% %Ith = X.*exp(2.*(alpha_internal + alpha_mirror)/Y);
%
% %x = P_opt./eta_d;
% y = hv_q.*Ith;
%


% for i=1:100;
%     eta_d = eta_i*log(1./R)./(log(1./R) + 0.6);
%     Ith =((q*V*B*Ntr^2)/eta_i).*exp(2.*(alpha_internal + alpha_mirror)/(gamma*go*L))
%     Ith_mA = Ith*1000;
%     eta_wall(i,:) = (eta_d.*(I(i) - Ith_mA)./I(i));
% end


%plot(R, eta_wall, 'r');


%figure; surf(I, R, eta_wall)
```

A.3 Multi-Mode Simulation

```
dv = 6e9;    %Hz
lambda = 1550e-9;   %
c = 2.998e8;
```

```
v = (c/lambda);
dlambda = lambda*dv/v;


fsr_v = 16.9e6;
fsr_lambda = fsr_v * (lambda^2) / c;



gamma = (dlambda*1e9)/2;
x0 = 1550;
span = 0.2;
%spacing = span/fsr_lambda;
spacing = 100;
x = linspace(x0 - span/2,x0 + span/2, spacing);
lineshape_unnorm = (1/pi).*(gamma ./ ((x - x0).^2 + gamma^2));
lineshape = lineshape_unnorm / max(lineshape_unnorm);


%phase = exp(-2*pi*1i.*rand(1,length(lineshape)));
%linephase = lineshape.*phase;
%lineshape = linephase;


figure;
subplot(2,1,1);
plot(x, abs(real(lineshape)));


%planewaves = zeros(1,length(x));
%for j=1:length(x);
%    planewaves(j) = lineshape(j)*exp(-1i*x(j));
%end


autoc = zeros(1,length(x));
```

```
for j=1:length(x);

    for k=1:length(x);

        index = abs(k - j) + 1;

        if index==1;

            freqcomp = lineshape(j)* conj(lineshape(k));

        else

            freqcomp = (lineshape(j) * conj(lineshape(k)))/2;

        end

        autoc(index) = autoc(index) + freqcomp;

    end

end


power = max(abs(real(autoc)));


subplot(2,1,2);


y = linspace(0,span, length(x));
V = ((y / 1550^2)*c);


plot(V, abs(real(autoc))/power);
```

A.4 Polarization Šolc Filter Simulation

```
z = 10;                                     % meters
alpha = 2*pi*0.0120;                                % twist rate rad/m
lambda = linspace(1301, 1301.5, 100000)*1e-9;
ne = 1.5;                                   % extraordinary index
no = 1.49;                                  % ordinary index
Gamma = (2*pi*(ne - no)*z)./lambda;
%Gamma = linspace(0,2800,10000);
```

```matlab
%rho = 2*pi*0.1;

phi = z*alpha;

N = 1000;

R1 = [cos(phi) sin(phi); -sin(phi) cos(phi)];

R2 = [cos(-phi/N) sin(-phi/N); -sin(-phi/N) cos(-phi/N)];

Py = [0.3 0; 0 0.8];

Px = [0.8 0; 0 0.3];

%E_in = (1/sqrt(2))*[1;1];

E_in = [1;1];

I_out = zeros(length(Gamma), 1);

T_out = zeros(length(Gamma), 1);


for j=1:length(Gamma);
    w0 = [exp(-1i*Gamma(j)/(2*N)) 0; 0  exp(1i*Gamma(j)/(2*N))];
    M = R1*(w0*R2)^N;
    E_out = Px*M*Py*E_in;
    I_out(j) = (abs(E_out(1))^2 + abs(E_out(2))^2);
    T_out(j) = (abs(E_out(1))^2 + abs(E_out(2))^2)/(abs(E_in(1))^2 + abs(E_in(2))^2);
end


figure;
%subplot(2,1,1)
%plot(lambda, 10*log10(T_out));
%subplot(2,1,2)
plot(lambda, T_out);
```

Appendix B

GPIB Python Code

B.1 Single OSA Spectrum Scan

```
#!/usr/local/bin python

import time
from visa import *
from numpy import *
from scipy import io
print "got here0"

filename = "ring_laser_osa_chip4_21Jan2013_wavelengthmod_20Vpp_4.mat"
centerwl = 1307
span = 15
resbw = 0.2
startwl = centerwl - (span/2)
stopwl = centerwl + (span/2)
numpts = 800
current = 300
voltage = 0
wavelength = []
```

```python
spectra = []


#Initialize GPIB comm channels and id query for both OSA and LDC
osa = instrument("GPIB::23", timeout = 30)


print osa.ask("ID?")


xdata = osa.ask_for_values("TRA?")
ydata = linspace(startwl, stopwl, numpts)


spectra.append(xdata)
wavelength.append(ydata)


print filename
io.savemat(filename, {"spectra": spectra, "wavelength": wavelength, \
"current": current, "voltage":voltage})
```

B.2   Single MSA Spectrum Scan

```python
import time
from visa import *
from numpy import *
from scipy import io
print "got here0"



filename = "RIN_calibration_30Jan2013_log_2-22GHz_RIN.mat"
start_freq = 2
stop_freq = 22      #Mhz
opt_power = -2.8     # dBm
```

```
wavelength = 1550

reflevel = 0                 #dBm

resbw = 511 #KHz

freq = linspace(start_freq,stop_freq,1001)



#Initialize GPIB comm channels and id query for both OSA and LDC

#osa = instrument("GPIB::23", timeout = 30)

#ldc = instrument("GPIB::25", timeout = 30)

msa = instrument("GPIB::18", timeout = 30)



#print osa.ask("ID?")

#print ldc.ask("*IDN?")

print msa.ask("ID?")



fdata = msa.ask_for_values("TRA?")

print filename

io.savemat(filename, {"msa_spectra": array(fdata), "freq": array(freq), \

"opt_poweruW": opt_power, "resbw": resbw})
```

B.3   Multiple OSA Spectra Scan with Laser Diode Controller Step

```
#!/usr/local/bin python

import time
from visa import *
from numpy import *
```

```python
from scipy import io
print "got here0"


filename = "ring_laser_osa_17Jan13_time_stability_1300nm_v3_log.mat"



#Initialize GPIB comm channels and id query for both OSA and LDC
osa = instrument("GPIB::23", timeout = 30)
ldc = instrument("GPIB::25", timeout = 30)
print osa.ask("ID?")
print ldc.ask("*IDN?")


centerwl = 1301.8
span = 3
resbw = 0.1
startwl = centerwl - (span/2)
stopwl = centerwl + (span/2)
numpts = 800
ydata = linspace(startwl, stopwl, numpts)



#Set LDC current and temperature
#ldc.write("LAS:CHAN 1;LAS:MODE:LDI;LAS:LDI 20;LAS:OUT on")
ldc.write("LAS:CHAN 1;LAS:MODE:LDI;LAS:LDI 300;LAS:STEP 500;LAS:OUT on")
#ldc.write("LASer:STEP 10000")
#ldc.write("DELAY 5000")
#ldc.write("LAS:CHAN 2;LAS:MODE:LDI;LAS:LDI 20;LAS:OUT on")
#ldc.write("DELAY 5000")
time.sleep(5)
```

```python
xdata = []
idata = []
#Begin loop
for i in range(100):
    #n = 5*i + 120
    print i
    #ldc.write("LAS:INC 1")
    time.sleep(5)
    data = osa.ask_for_values("TRA?")
    #time.sleep(3)
    xdata.append(data)


    #for j in range(10):
    #    data = osa.ask_for_values("TRA?")
    #    ydata.append(data)
    #    time.sleep(3)


    #i = ldc.ask("LAS:LDI?")
    idata.append(float(i))


print filename
io.savemat(filename, {"spectra": array(xdata), "current": array(idata), \
"wavelength":array(ydata)})
```

Appendix C

Commercial SOA and Comb Filter Data Sheets

COVEGA | THORLABS Quantum Electronics Inc.

Thorlabs Quantum Electronics
Booster Optical Amplifier (BOA)
Part Description: 14 Pin Butterfly Packaged BOA
Package Description:1130-0-0-T-S-S-A-A

Serial Number: BOA-13559-12195.13.D04
Test Date: 09-Apr-13

Summary of Test Data

CW; T (Chip) = 25.0°C, T (Case) = 25.0°C, Seed λ=1312 nm

Parameter			
Operating Current	I_{OP}	700	mA
ASE Central Wavelength	λ_C	1287.8	nm
Optical 3 dB Bandwidth	BW	86.7	nm
Saturation Output Power @ -3 dB	P_{SAT}	18.3	dBm
Small Signal Gain @ Pin = -20 dBm	G	32.0	dB
Max Gain Ripple (RMS) @ I_{OP}	δG	0.10	dB
Noise Figure	NF	6.9	dB
Forward Voltage	V_F	1.8	V
TEC Operation @ T_{CASE} = 25°C			
- TEC Current	I_{TEC}	0.50	A
- TEC Voltage	V_{TEC}	0.63	V
- Thermistor Resistance	R_{TH}	10K	Ω

Steinhart Constants : a=1.129241E-3; b=2.341077E-4; c=8.775468E-8

Model: BOA1130   Rev: A
QA: Pass
Test Operator: Paya

COVEGA | THOR LABS Quantum Electronics Inc.

Serial Number: BOA-13559-12195.13.D04
Test Date: 09-Apr-13

Figure 1: BOA LIV Plot

Figure 2: BOA Spectrum

COVEGA | THORLABS Quantum Electronics Inc.
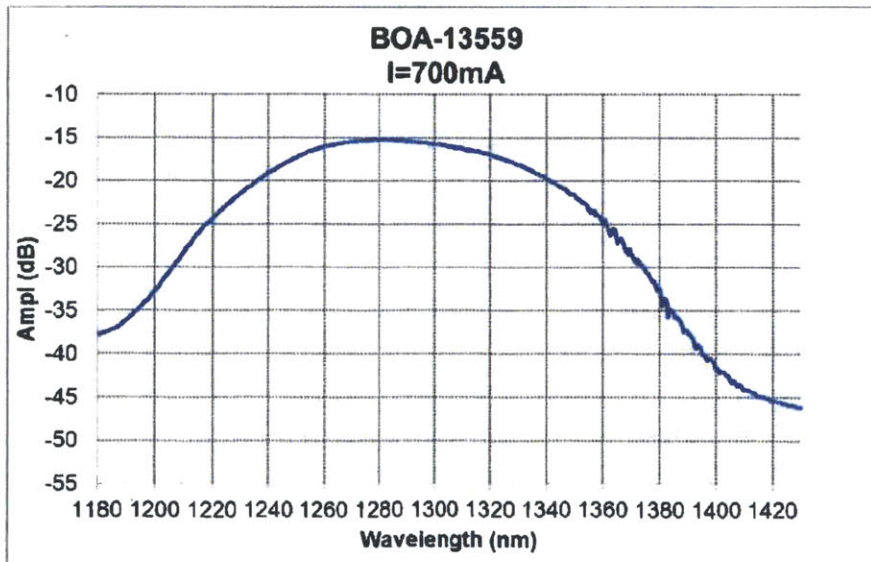
Serial Number: BOA-13559-12195.13.D04
Test Date: 09-Apr-13

Figure 3: BOA Fine Spectrum

Figure 4: Gain vs Current Plot

COVEGA | **THOR**LABS
Quantum Electronics Inc.

Thorlabs Quantum Electronics
Booster Optical Amplifier (BOA)
Part Description: 14 Pin Butterfly Packaged BOA
Package Description:1130-0-0-T-S-S-A-A

Serial Number: BOA-13559-12195.13.D04
Test Date: 09-Apr-13

Figure 5: Gain vs Output Plot

COVEGA | THOR
Quantum Electronics Inc.

Serial Number: BOA-7414-11812.5.E03
Test Date: 06-May-10

Summary of Test Data			
CW; T (Chip) = 25.0°C, T (Case) = 25.0°C, Seed λ=1312 nm			
Parameter			
Operating Current	I_{OP}	700	mA
ASE Peak Wavelength	$λ_C$	1298.0	nm
Optical 3 dB Bandwidth	BW	80.0	nm
Saturation Output Power @ -3 dB	P_{SAT}	18.9	dBm
Small Signal Gain @ Pin = -20 dBm	G	33.0	dB
Max Gain Ripple (p-p) @ I_{OP}	$δG$	0.62	dB
Noise Figure	NF	5.9	dB
Forward Voltage	V_F	1.60	V
TEC Operation @ T_{CASE} = 25°C			
- TEC Current	I_{TEC}	0.41	A
- TEC Voltage	V_{TEC}	0.53	V
- Thermistor Resistance	R_{TH}	10K	Ω
Steinhart Constants : a=1.129241E-3; b=2.341077E-4; c=8.775468E-8			

Model: BOA1132   Rev: A
QA: Pass
Test Operator: Lee

COVEGA | THOR Quantum Electronics Inc.

Thorlabs Quantum Electronics
Booster Optical Amplifier (BOA)
Part Description: 14 Pin Butterfly Packaged BOA
Package Description:1132-0-0-T-S-S-A-A

Serial Number: BOA-7414-11812.5.E03
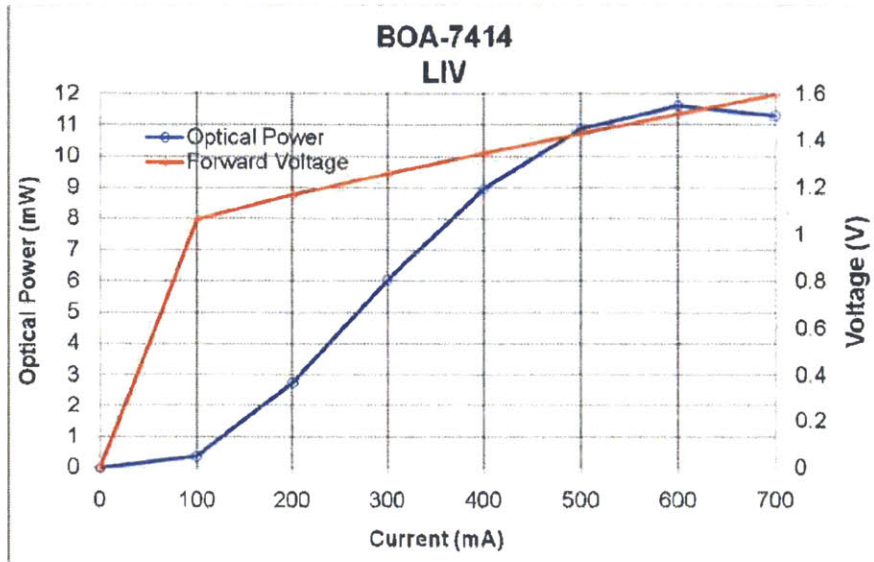Test Date: 06-May-10
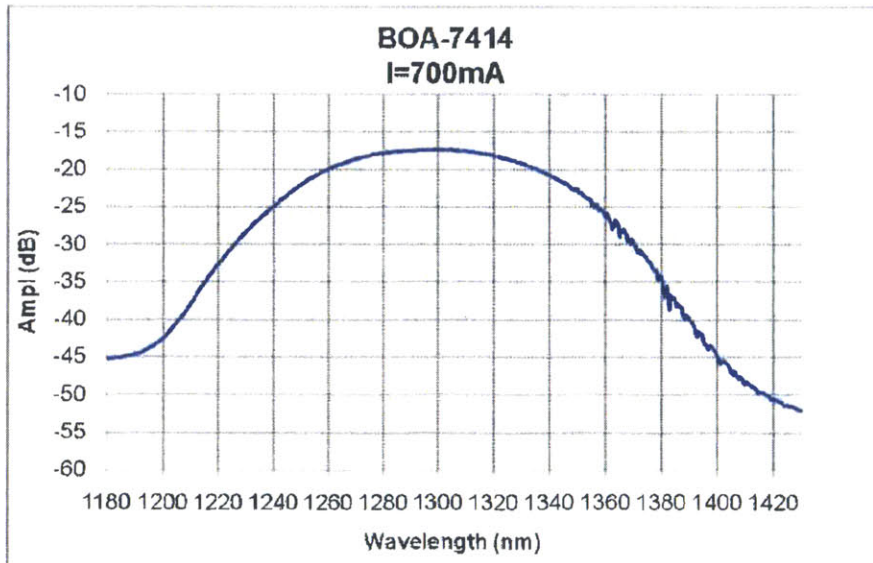

Figure 1: BOA LIV Plot

Figure 2: BOA Spectrum

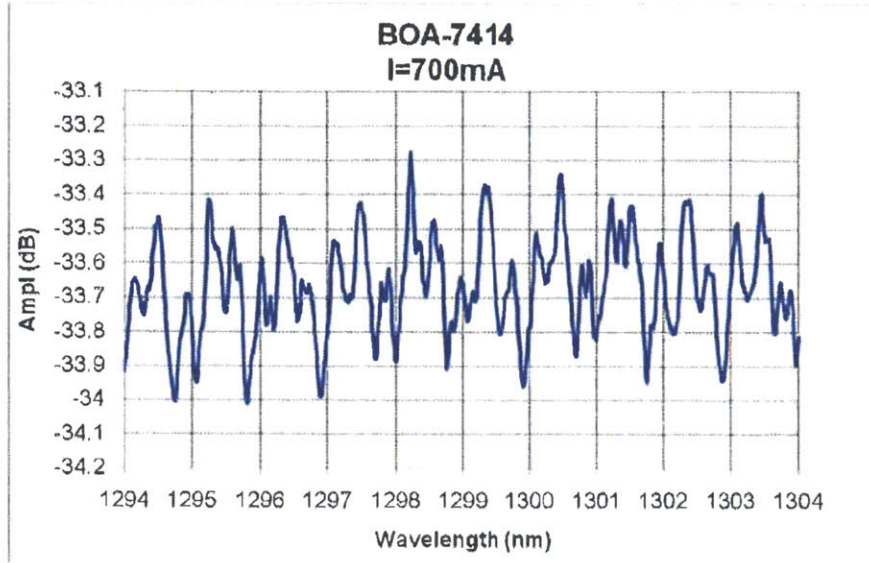Serial Number: BOA-7414-11812.5.E03
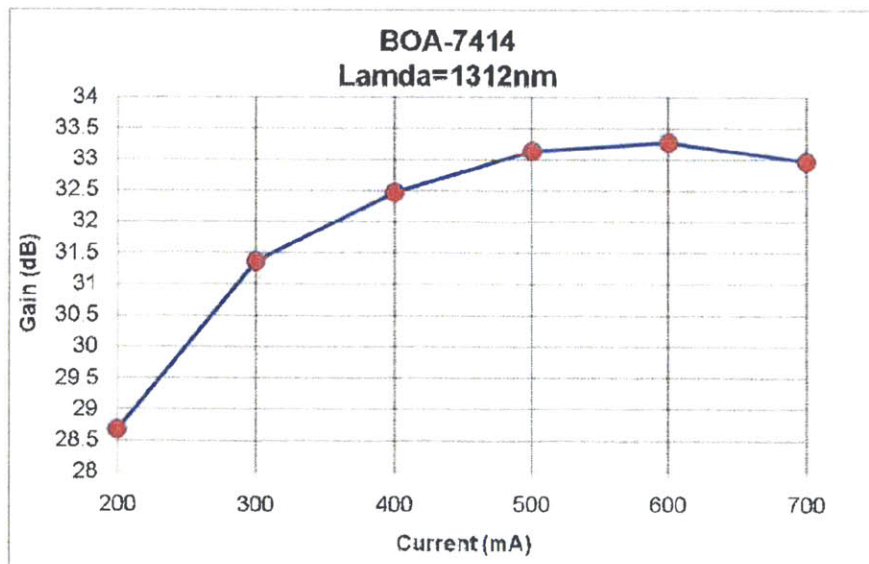Test Date: 06-May-10

Figure 3: BOA Fine Spectrum

Figure 4: Gain vs Current Plot

Serial Number: BOA-7414-11812.5.E03
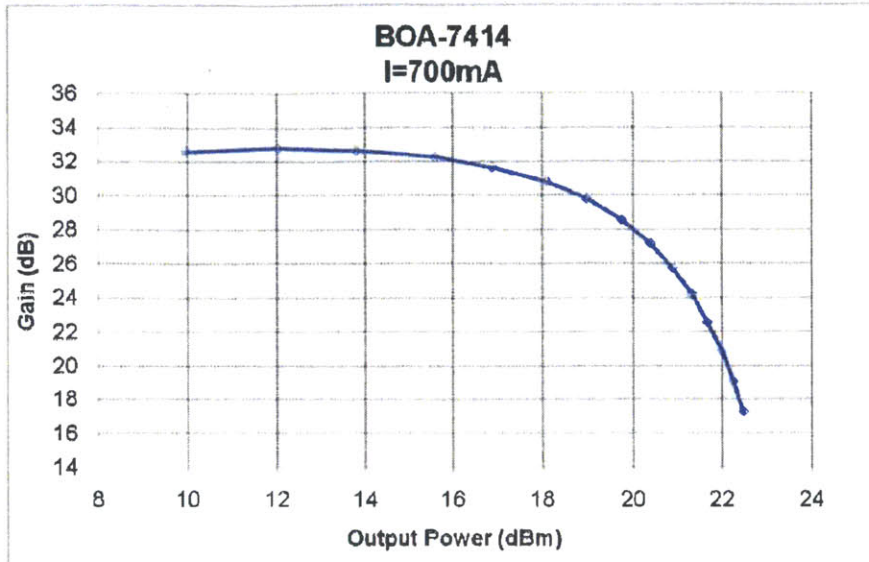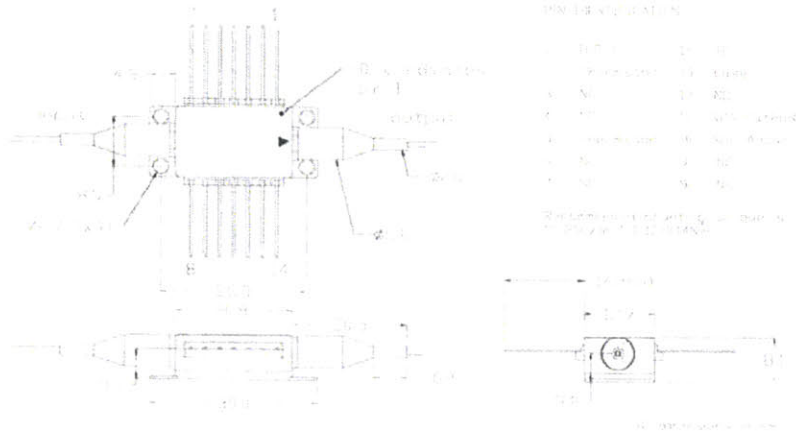Test Date: 06-May-10

Figure 5: Gain vs Output Plot

Serial Number: BOA-7414-11812.5.E03
Test Date: 06-May-10

Packaging

Attention:

Please observe the following precautions when mounting the butterfly package to a heatsink:
1. The heatsink should be as flat as possible.
2. Thermal grease or an alternative thin but compliant material is recommended to be used between package and heatsink.
3. Screws should be tightened in a suitable sequence so that package mates to the heatsink without screw heads being forced up and into package snout.
4. Maximum torque of 10~20oz·in (0.07~0.14N·m) is recommended for screw tightening.

Failure to comply to the above may cause damage to the internal thermo-electric cooler.

INNOLUME

TEST REPORT for 14-pin butterfly SOA module

Tested:	26.07.13	I. Bakshaev		Product type:	SOA-1220-60-PM-18dB
Approved:	26.07.13	I. Krestnikov		Module ID:	DO1868b-q4-Bo4-B3

PARAMETERS

Test conditions. CW operation: 25°C

Parameters	Value	Unit
Operating current	400	mA
Forward voltage	1.30	V
Maximum net gain	21.2	dB
Output saturation power (-3dB)	12.0	dBm
Wavelength of gain maximum	1220	nm
Spectral bandwidth (-3dB)	60	nm
Ripples average amplitude	0.15	dB
Polarization extinction ratio (Input)	22	dB
Polarization extinction ratio (Output)	24	dB

ABSOLUTE MAXIMUM RATINGS

Parameters	Min.	Max.	Unit
Wire soldering temperature		250 (5 sec.)	°C
TEC voltage		4	V
TEC current		3	A
Reverse voltage		2.0	V
Input optical power		1.0	dBm
Forward current		1.0	A
Storage temperature range	5	80	°C
Operating temperature range	10	50.0	°C

DIMENSIONS
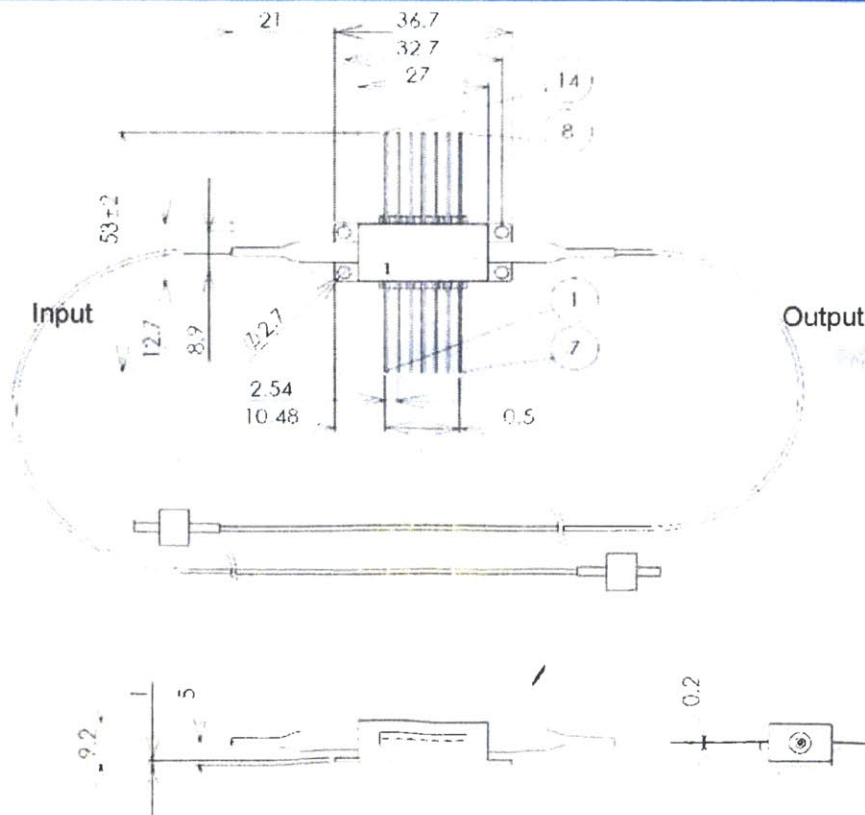
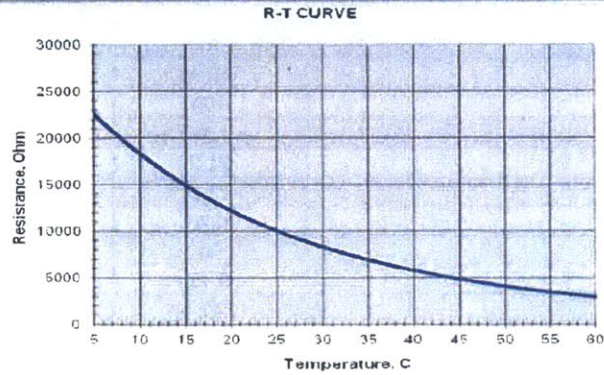**Pin idetntification:**

1. TEC " + "
2. Thermistor
3.
4.
5. Thermistor
6.
7.
8.
9.
10. SLD anode (+)
11. SLD cathode (-)
12.
13. Case ground
14. TEC " - "

INNOLUME
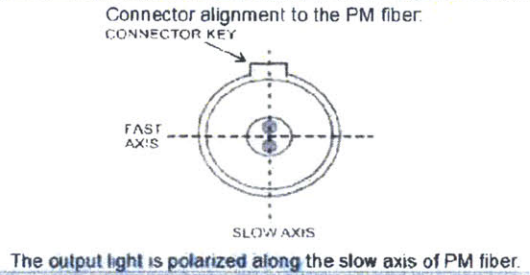
THERMISTOR SPECIFICATION

Parameters	Value	Unit
Resistance @25°C	10000	Ohm
Resistance Tol. ±	5	%
Beta +25°C/+75°C	3477	K
NTC @ + 25 °C	5	%/°C

R-T CURVE

FIBER SPECIFICATION

Parameters	Value	Unit
Type	PANDA PM980	
Connector type	FC/APC	
Length	1 - 1.2	m
Mode-field diameter	6.6	µm
Cladding diameter	125	µm
Coating diameter	245	µm
Jacket	NA	µm
NA	0.11	

Connector alignment to the PM fiber:

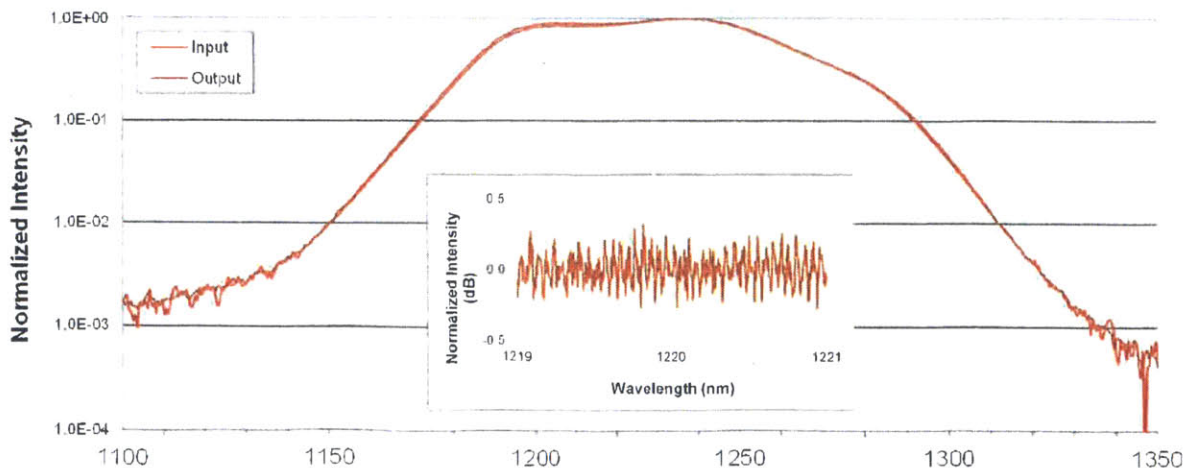The output light is polarized along the slow axis of PM fiber.
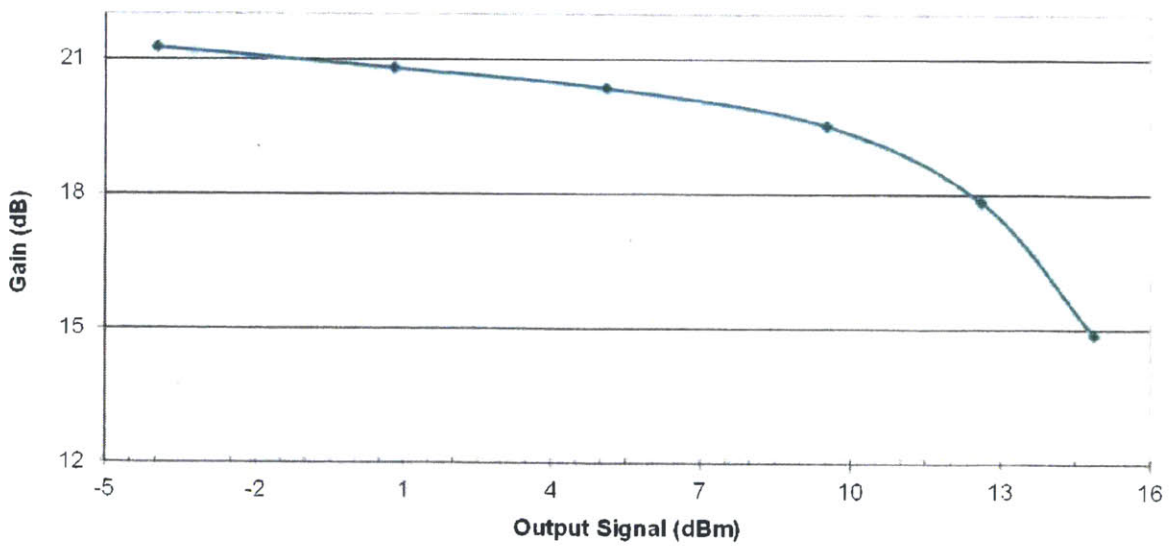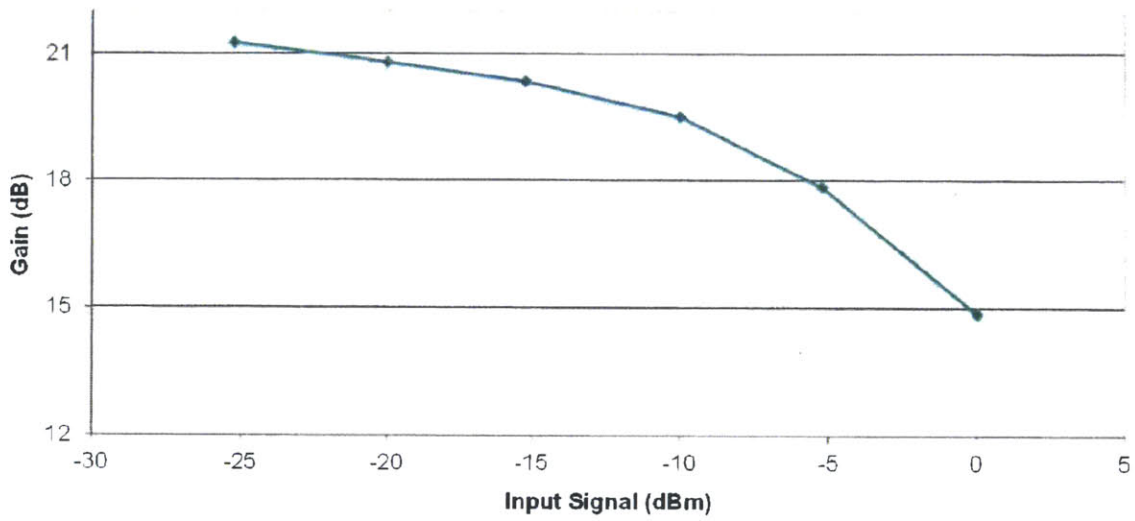
ASE L-I-V CURVE
Test conditions: CW operation, 25°C
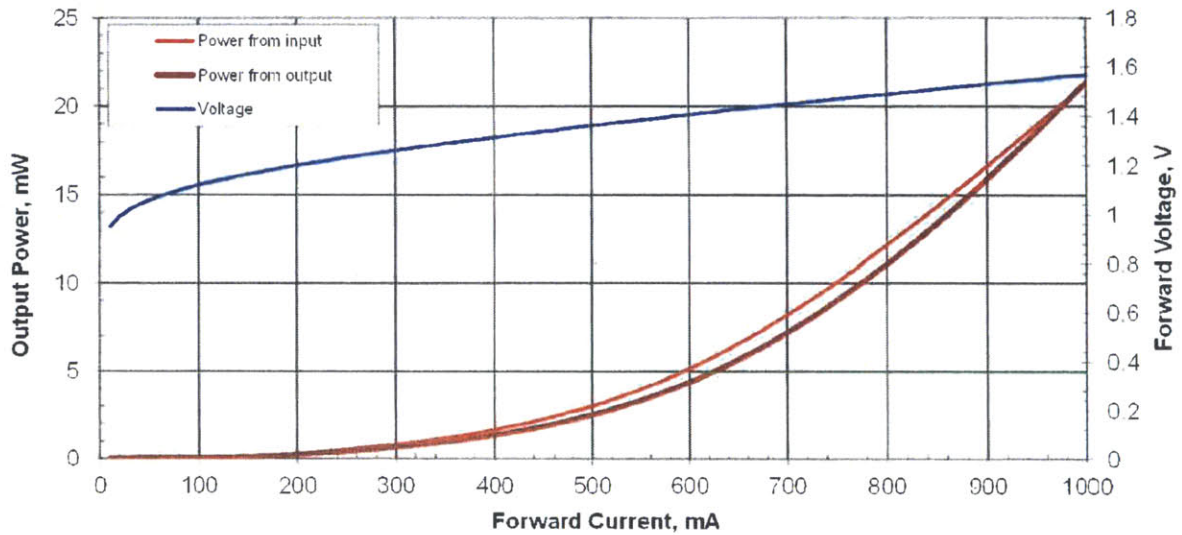
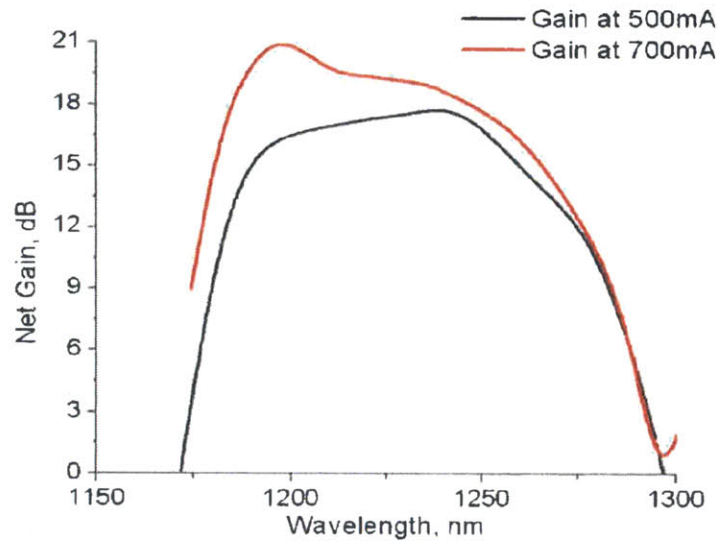## ASE SPECTRUM
Test conditions: CW operation, 400mA, 25°C

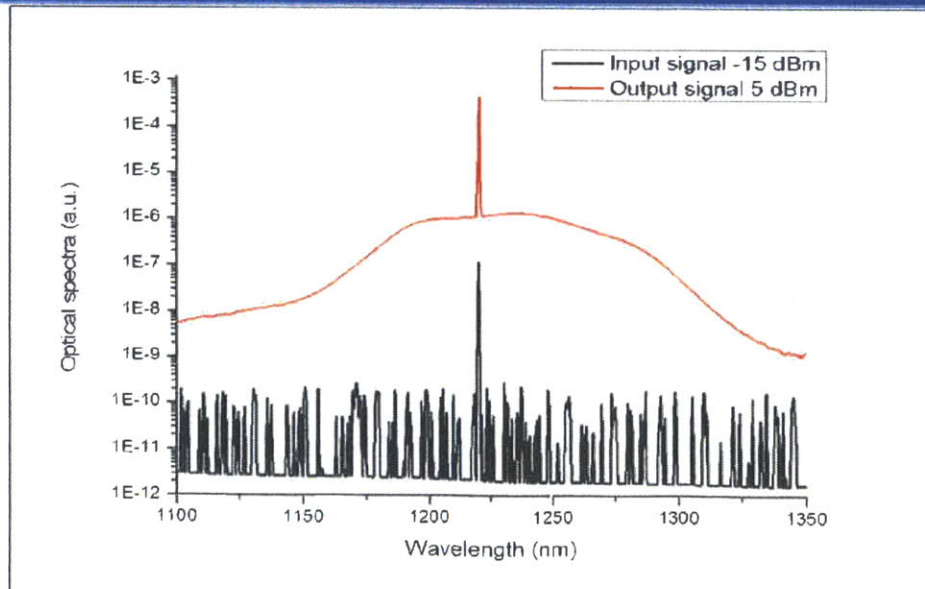## GAIN VALUE
Test conditions: CW operation, 1030nm, 400mA, 25°C

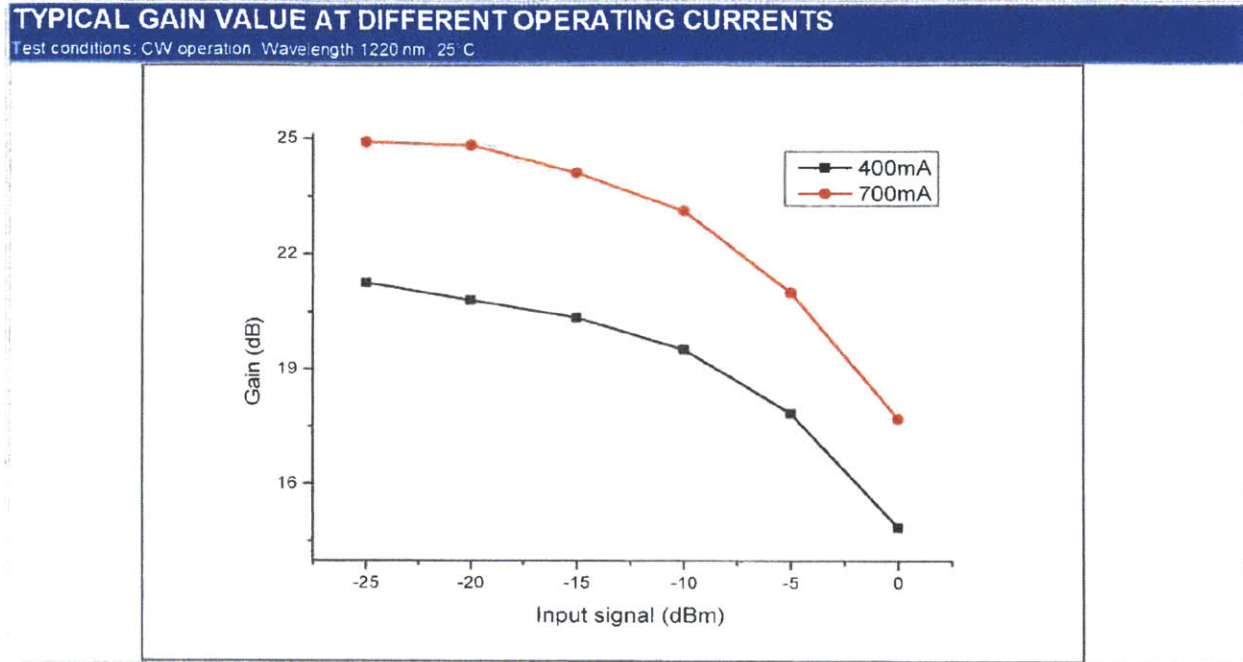## TYPICAL GAIN SPECTRA
Test conditions: CW operation, 25°C

TYPICAL SPECTRA
Test conditions: CW operation, 400mA, 25°C, Resolution 500pm

TYPICAL GAIN VALUE AT DIFFERENT OPERATING CURRENTS
Test conditions: CW operation. Wavelength 1220 nm, 25°C

SAFETY AND OPERATING INSTRUCTIONS

The light emitted from this device is invisible and will harmful to the human eye. Avoid looking directly into the fiber connector of the module or into the collimated beam along its optical axis when the device is in operation. Proper laser safety eyewear must be worn during operation.

Absolute Maximum Ratings may be applied to the SOA module for short period of time only. Exposure to maximum ratings for extended period of time or exposure more than one maximum ratings may cause damage or affect the reliability of the device.

Operating the SOA module outside of its maximum ratings may cause device failure or a safety hazard. Power supplies used with the component must be employed such that the maximum forward current cannot be exceeded. A proper heatsink for the laser diode module on thermal radiator is required. The module must be mounted on radiator with screws (bolt down in X-style fashion with initial torque set to 0.075Nm and final X-style bolt down at 0.15Nm) or clamps. The deviation from flatness of radiator surface must be less than 0.05mm. It's recommended using of In-foil or similar between bottom of the module and heatsink for thermal interface. It's undesirable to use thermal grease for this.

Do not pull the fiber. Do not bend a fiber with a radius smaller than 3 cm. Operate the laser module with clean fiber connector only. Periodically check and clean the connector if necessary. To clean the connector use a clean-room compatible tissue only, put some Isopropyl alcohol onto it and carefully clean the facet of the connector, or use special fiber cleaning tools. Perform cleaning only with the laser current switched off.

ESD PROTECTION – Electrostatic discharge is the primary cause of unexpected devicee failure. Take extreme precaution to prevent ESD. Use wrist straps, grounded work surfaces and rigorous antistatic techniques when handling the devices.

LASER RADIATION
AVOID EXPOSURE TO THE BEAM
CLASS 3B LASER PRODUCT

CAUTION
STATIC SENSITIVE DEVICE
OBSERVE PRECAUTIONS

DANGER

VISIBLE AND/OR INVISIBLE LASER RADIATION
AVOID EYE OR SKIN EXPOSURE TO
DIRECT OR SCATTERED RADIATION

DIODE LASER
MAX POWER 0,5W
WAVELENGTH 1000 - 1400 nm
CLASS IIIb LASER PRODUCT

Test Date	October 22, 2012
Center Wavelength	1550 nm
FSR	247.35 GHz
Bandwidth	6.033 GHz
Finesse	41
Loss	0.20 dB

Conformance Statement

Micron Optics confirms that the following Fiber Fabry-Perot Filter has been manufactured using fully qualified, consistent, procedures and materials.   The proof of the conformance is presented in the above serialized data sheet.

Handling

Any FFP product must be handled *carefully*. As with all high performance Fabry-Perot devices, mirrors are aligned to nanometer tolerance. If the FFP is subjected to excessive shock the mirrors will become misaligned and the filter performance will degrade.

Connectorization

Do not hold sheath and pull fiber; breakage could occur as a result. Pigtails contain loose buffered fiber pigtails so special connectorization procedures are required.

1. Chemically stripping the fiber is preferred.
2. To mechanically strip fiber, wrap 6 to 8 turns of buffered fiber around a 1 inch diameter mandrel to transfer tensile load from fiber to buffer. Gently strip fiber.
3. Minimize residual compressive load on fiber relative to sheath when inserting connector ferrule.
4. Follow remaining standard connectorization procedures.

MICRON OPTICS, INC.
1852 Century Place North East
Atlanta, Georgia 30345 USA
Tel. (404) 325-0005
Fax. (404) 325-4082

email: moi@micronoptics.com
internet: www.micronoptics.com

Test Date	May 31, 2013
Center Wavelength	1310 nm
FSR	152.16 GHz
Bandwidth	0.1485 GHz
Finesse	1024
Loss	3.5 dB
Connector	FC / APC

Conformance Statement

Micron Optics confirms that the following Fiber Fabry-Perot Filter has been manufactured using fully qualified, consistent, procedures and materials. The proof of the conformance is presented in the above serialized data sheet.

Handling

Any FFP product must be handled *carefully*. As with all high performance Fabry-Perot devices, mirrors are aligned to nanometer tolerance. If the FFP is subjected to excessive shock the mirrors will become misaligned and the filter performance will degrade.

Connectorization

Do not hold sheath and pull fiber; breakage could occur as a result. Pigtails contain loose buffered fiber pigtails so special connectorization procedures are required.

1. Chemically stripping the fiber is preferred.
2. To mechanically strip fiber, wrap 6 to 8 turns of buffered fiber around a 1 inch diameter mandrel to transfer tensile load from fiber to buffer. Gently strip fiber.
3. Minimize residual compressive load on fiber relative to sheath when inserting connector ferrule.
4. Follow remaining standard connectorization procedures.

MICRON OPTICS, INC.
1852 Century Place North East
Atlanta, Georgia 30345 USA
Tel. (404) 325-0005
Fax. (404) 325-4082

email: moi@micronoptics.com
internet: www.micronoptics.com

Test Date	July 22, 2013
Center Wavelength	1310 nm
FSR	162.90 GHz
Bandwidth	0.895 GHz
Finesse	182
Loss	1.76 dB
Connector	FC / APC

Conformance Statement

Micron Optics confirms that the following Fiber Fabry-Perot Filter has been manufactured using fully qualified, consistent, procedures and materials.   The proof of the conformance is presented in the above serialized data sheet.

Handling

Any FFP product must be handled *carefully*. As with all high performance Fabry-Perot devices, mirrors are aligned to nanometer tolerance. If the FFP is subjected to excessive shock the mirrors will become misaligned and the filter performance will degrade.

Connectorization

Do not hold sheath and pull fiber; breakage could occur as a result. Pigtails contain loose buffered fiber pigtails so special connectorization procedures are required.

1. Chemically stripping the fiber is preferred.
2. To mechanically strip fiber, wrap 6 to 8 turns of buffered fiber around a 1 inch diameter mandrel to transfer tensile load from fiber to buffer. Gently strip fiber.
3. Minimize residual compressive load on fiber relative to sheath when inserting connector ferrule.
4. Follow remaining standard connectorization procedures.

MICRON OPTICS, INC.
1852 Century Place North East
Atlanta, Georgia 30345 USA
Tel. (404) 325-0005
Fax. (404) 325-4082

email: moi@micronoptics.com
internet: www.micronoptics.com

Bibliography

[1] Jason S. Orcutt. *Monolithic Electronic-Photonic Integration in State-of-the-Art CMOS Processes*. PhD thesis, Massachusetts Institute Technology, Department of Electrical Engineering and Computer Science, February 2012.

[2] Christopher Batten, Ajay Joshi, Jason Orcutt, Anatoly Khilo, Benjamin Moss, Charles W Holzwarth, Miloš A Popovic, Hanqing Li, Henry I Smith, Judy L Hoyt, et al. Building many-core processor-to-dram networks with monolithic cmos silicon photonics. *Micro, IEEE*, 29(4):8–21, 2009.

[3] Jason S Orcutt, Anatol Khilo, Charles W Holzwarth, Milos A Popović, Hanqing Li, Jie Sun, Thomas Bonifield, Randy Hollingsworth, Franz X Kärtner, Henry I Smith, et al. Nanophotonic integration in state-of-the-art cmos foundries. *Optics Express*, 19(3):2335–2346, 2011.

[4] L.A. Coldren, S.W. Corzine, and M.L. Mashanovitch. *Diode Lasers and Photonic Integrated Circuits*. Wiley Series in Microwave and Optical Engineering. Wiley, 2011.

[5] QDLaser. QLD1161-8030 Datasheet. *1180 nm 30mw DFB Laser Butterfly Package*, January 2012.

[6] Alexander W Fang, Hyundai Park, Oded Cohen, Richard Jones, Mario J Paniccia, and John E Bowers. Electrically pumped hybrid algainas-silicon evanescent laser. *Opt. Express*, 14(20):9203–9210, 2006.

[7] Jifeng Liu, Xiaochen Sun, Lionel C Kimerling, and Jurgen Michel. Direct-gap optical gain of ge on si at room temperature. *Optics letters*, 34(11):1738–1740, 2009.

[8] Jifeng Liu, Xiaochen Sun, Rodolfo Camacho-Aguilera, Lionel C Kimerling, Jurgen Michel, et al. Ge-on-si laser operating at room temperature. *Opt. Lett*, 35(5):679–681, 2010.

[9] Rodolfo E Camacho-Aguilera, Yan Cai, Neil Patel, Jonathan T Bessette, Marco Romagnoli, Lionel C Kimerling, and Jurgen Michel. An electrically pumped germanium laser. *Optics express*, 20(10):11316–11320, 2012.

[10] Purnawirman, J. Sun, T. N. Adam, G. Leake, D. Coolbaugh, J. D. B. Bradley, E. Shah Hosseini, and M. R. Watts. C- and l-band erbium-doped waveguide lasers with wafer-scale silicon nitride cavities. *Opt. Lett.*, 38(11):1760–1762, Jun 2013.

[11] JDSU. 980 nm Pump Laser Datasheet. *Up to 460 mW Fiber Bragg Grating Stabilized 980 nm Pump Modules S27 Series*, May 2011.

[12] Y. C. Yan, A. J. Faber, H. De Waal, P.G. Kik, and A. Polman. Erbium-doped phosphate glass waveguide on silicon with 4.1 db/cm gain at 1.535 micrometers. *Applied Physics Letters*, 71(20):2922–2924, Nov 1997.

[13] D Livshits, D Yin, A Gubenko, I Krestnikov, S Mikhrin, A Kovsh, and G Wojcik. Cost-effective wdm optical interconnects enabled by quantum dot comb lasers. In *OPTO*, pages 76070W–76070W. International Society for Optics and Photonics, 2010.

[14] Innolume. LD-1310-COMB-12 Datasheet. *Fiber coupled Comb Laser Diode @ 1310 nm*, June 2013.

[15] A Gubenko, S Mikhrin, V Mikhrin, I Krestnikov, and D Livshits. Low-power monolithic comb laser for short-reach wdm optical interconnects. In *IEEE Photonics Conference*, 2012.

[16] A. Gubenko, A. Kovsh, G. Wojcik, D. Livshits, I. Krestnikov, and S. Mikhrin. Semiconductor laser with low relative intensity noise of individual longitudinal modes and optical transmission system incorporating the laser, April 2 2013. US Patent 8,411,711.

[17] Seok-Hwan Jeong, S. Tanaka, S. Sekiguchi, T. Kurahashi, N. Hatori, S. Akiyama, T. Usuki, Tsuyoshi Yamamoto, and K. Morito. Hybrid laser with si ring resonator and soa for temperature control free operation with ring resonator-based modulator. In *Group IV Photonics (GFP), 2011 8th IEEE International Conference on*, pages 172–174, 2011.

[18] K. Morito, S.H. Jeong, S. Tanaka, T. Akiyama, T. Kurahashi, S. Sekiguchi, and Y. Tanaka. Silicon photonics optical source for temperature control free operation with ring resonator based modulator. In *Photonics in Switching (PS), 2012 International Conference on*, pages 1–3, 2012.

[19] XP Dong, Shenping Li, KS Chiang, MN Ng, and BCB Chu. Multiwavelength erbium-doped fibre laser based on a high-birefringence fibre loop mirror. *Electronics Letters*, 36(19):1609–1610, 2000.

[20] Hongxin Chen. Multiwavelength fiber ring lasing by use of a semiconductor optical amplifier. *Optics letters*, 30(6):619–621, 2005.

152

[21] Tomoyuki Akiyama, Haruhiko Kuwatsuka, Takashi Simoyama, Yoshiaki Nakata, Kohki Mukai, Mitsuru Sugawara, Osamu Wada, and Hiroshi Ishikawa. Application of spectral-hole burning in the inhomogeneously broadened gain of self-assembled quantum dots to a multiwavelength-channel nonlinear optical device. *Photonics Technology Letters, IEEE*, 12(10):1301–1303, 2000.

[22] SW Harun, R Parvizi, S Shahi, and H Ahmad. Multi-wavelength erbium-doped fiber laser assisted by four-wave mixing effect. *Laser Physics Letters*, 6(11):813–815, 2009.

[23] Xinhuan Feng, Hwa-yaw Tam, and Ping-kong Alexander Wai. Stable and uniform multiwavelength erbium-doped fiber laser using nonlinear polarization rotation. *Optics express*, 14(18):8205–8210, 2006.

[24] Thorlabs. BOA1132S Datasheet. *O-Band Booster Optical Amplifier, CWL=1300 nm, Butterfly Pkg, SMF, FC/APC*, March 2011.

[25] M.T. Wade, J.M. Shainline, J.S. Orcutt, C. Sun, R. Kumar, B. Moss, M. Georgas, R.J. Ram, V. Stojanović, and M.A. Popović. Energy-efficient active photonics in zero-change, state-of-the-art cmos process. *OFC Conference Submission*, 2014.

[26] A. Yariv and P. Yeh. *Optical Waves in Crystals: Propagation and Control of Laser Radiation*. Wiley Series in Pure and Applied Optics. Wiley, 2002.